

UC San Diego

UC San Diego Electronic Theses and Dissertations

Title

Vortex dynamics : a window into the properties of type-II superconductors

Permalink

<https://escholarship.org/uc/item/8n68x115>

Author

Taylor, Benjamin Jeremy

Publication Date

2006

Peer reviewed|Thesis/dissertation

UNIVERSITY OF CALIFORNIA, SAN DIEGO

Vortex Dynamics:

A Window Into the Properties of Type-II Superconductors

A dissertation submitted in partial satisfaction of the
requirements for the degree Doctor of Philosophy

in

Physics

by

Benjamin Jeremy Taylor

Committee in charge:

Professor M. Brian Maple, Chair

Professor Daniel Arovas

Professor Dimitri N. Basov

Professor David R. Hendrickson

Professor Jan B. Talbot

2006

Copyright

Benjamin Jeremy Taylor, 2006

All rights reserved.

The dissertation of Benjamin Jeremy Taylor is approved,
and it is acceptable in quality

Chair

University of California, San Diego

2006

To my wife Michelle, for all her love and support... and to McKenna Christine
our daughter, who will be arriving in September.

TABLE OF CONTENTS

Signature Page	iii
Dedication	iv
Table of Contents	v
List of Figures	vii
List of Tables	ix
Acknowledgements	x
Vita, Publications, and Fields of Study	xii
Abstract	xiv
I Introduction	1
A. Superconductivity	2
1. BCS theory of superconductivity	3
B. Type I	4
1. The London equation	4
C. Type II	5
1. Ginzburg-Landau theory	6
D. Vortex dynamics	7
Bibliography	10
II Experimental Apparatus and Measurement Methods	12
A. The pulsed laser ablation deposition technique	12
1. Development of a unique laser ablation chamber for growth of volatile inter-metallic films	14
B. Measurements	18
1. X-rays	18
2. Magnetization	18
3. Electrical resistivity & Electric field-current density measurements	18
Bibliography	20
III Quantum Fluctuations, Vortex Flux Line Dynamics, and the Vortex- Solid to Vortex-Liquid Transition	21
A. Introduction	21
B. Experimental Details	27
C. The quantum- thermal-fluctuation model of Blatter and Ivlev	28
D. Modification of the Blatter and Ivlev model	31
E. Discussion	36

1.	$\text{Y}_{1-x}\text{Pr}_x\text{Ba}_2\text{Cu}_3\text{O}_{6.97}$ and $\text{YBa}_2\text{Cu}_3\text{O}_{6.5}$	36
2.	The vortex glass melting lines of $\text{Sm}_{1.85}\text{Ce}_{0.15}\text{CuO}_{4-y}$ and $\text{Bi}_2\text{Sr}_2\text{CaCu}_2\text{O}_8$	49
3.	The vortex glass melting lines of MgB_2 and $\alpha\text{-Mo}_x\text{Si}_{1-x}$	49
F.	Summary	53
	Bibliography	59
IV	Inhomogenous vortex matter in a high purity twinned $\text{YBa}_2\text{Cu}_3\text{O}_{7-\delta}$ single crystal	62
A.	Introduction	62
B.	Experimental Details	66
C.	Results and Discussion	68
D.	Summary	84
	Bibliography	87
V	Vortex glass and Bragg glass phases in MgB_2	89
A.	Introduction	89
B.	Experimental Details	91
C.	Results and Discussion	92
D.	Summary	107
	Bibliography	110
VI	Anomalous dynamic behavior of vortices amidst an emergent peak effect in CeRu_2 films	112
A.	Introduction	112
B.	Experimental Details	115
C.	Experimental Results	118
D.	Discussion	140
1.	Review	140
2.	Current results: relation to known peak effect anomalies	147
E.	Summary	150
	Bibliography	154
	Appendices	156
A	The modified vortex glass model of Rydh, Rapp, and Andersson	156
B	The Columb-gas model	157
C	Modified vortex glass scaling model: Magnetic field dependencies	160
D	Critical behavior: suppression of the superfluid density	163
	Bibliography	165

LIST OF FIGURES

II.1	Top view schematic of deposition chamber	16
II.2	Side view schematic of deposition chamber	17
III.1	Vortex glass melting line data: 1 st modified melting line equation	37
III.2	Vortex glass melting line data: 2 nd modified melting line equation	38
III.3	Comparison of various vortex glass melting line equations	39
III.4	The exponent s obtained from vortex glass scaling of $\rho(T)$	42
III.5	The quantum parameter, $q(t)$	44
III.6	Temperature dependence of the quantum tunneling length	46
III.7	Fraction of quantum- to thermal fluctuations	47
III.8	Vortex glass melting lines of $\text{Sm}_{1.85}\text{Ce}_{0.15}\text{CuO}_{4-y}$ & $\text{Bi}_2\text{Sr}_2\text{CaCu}_2\text{O}_8$	50
III.9	Vortex glass melting line of bulk MgB_2	51
III.10	Vortex glass melting line of amorphous $\alpha\text{-Mo}_x\text{Si}_{1-x}$	52
IV.1	Electrical resistivity $\rho(H, T)$ of a twinned YBCO single crystal . .	69
IV.2	Electric field E vs transport current density J isotherms	72
IV.3	Scaled $E - J$ data	73
IV.4	Scaled resistivity data, $(d\ln(\rho)/dT)^{-1}$ vs T	75
IV.5	$H(T)$ phase diagram of a high purity, twinned, $\text{YBa}_2\text{Cu}_3\text{O}_{7-\delta}$ single crystal	80
V.1	Electric field E vs transport current density J isotherms for HIPed MgB_2	93
V.2	Scaled $E - J$ data	95
V.3	Zero-field vortex-glass coherence length	98
V.4	Width of the critical region	100
V.5	Critical current density, J_c , in the $H - T$ phase diagram of MgB_2	102
V.6	Iso-current density lines in the $H - T$ plane	103
V.7	$H - T$ phase diagram of HIPed MgB_2	104
V.8	Scaling behavior of J_c at low magnetic fields	106
VI.1	SEM images of CeRu_2 films “A” and “B”	116
VI.2	X-ray data for films “A” and “B”	117
VI.3	$\chi \equiv 4\pi M/H$, data for target sample and films	120
VI.4	Zero field resistivity data, $\rho(T)$, for target sample and films “A” and “B”	121
VI.5	TAFF behavior of film “A”	124
VI.6	$\rho(T)$, data for film “B”	125
VI.7	$\rho(H)$, data for films “A” and “B”	127
VI.8	$\rho(H)$, data for films “B” and “C”	129
VI.9	Critical current density, $J_c(H)$, data of films “A” and “B”	130
VI.10	$F_p(H)$ and scaled $F_p(H)$ data for films “A” and “B”	132

VI.11	Enhanced pinning force density of the large grain CeRu ₂ film “B”	133
VI.12	Comparison of $M(H)$ and $J_c(H)$	135
VI.13	$E - J$ and scaled $E - J$ data	136
VI.14	Behavior of $\rho(H)$ in the emerging peak effect region	138
VI.15	Correlation of $M(H)$, c_B , and Δ_ℓ behavior with the peak effect .	139
VI.16	$H - T$ phase diagram of CeRu ₂ films	142
VI.17	The missing peak effect in CeRu ₂ single crystals	146
B.1	Modified vortex glass scaling	159
B.2	Coulomb-glass scaling	159

LIST OF TABLES

III.1	Parameters obtained from fit to 1 st modified melting line equation	56
III.2	Parameters obtained from fit to 2 nd modified melting line equation	57
IV.1	Critical exponents, temperatures, and coherence lengths of a high purity, twinned, YBa ₂ Cu ₃ O _{7-δ} single crystal	85
V.1	Values of scaling parameters for bulk MgB ₂	108
VI.1	Values of scaling parameters for a large grain CeRu ₂ film	152

ACKNOWLEDGEMENTS

First, I would like to thank my advisor, M. Brian Maple, for supporting me through the years, for his guidance, and for allowing me the freedom to pursue the directions which the research presented within has taken me.

I would like to recognize the help of my coworkers Dan Scanderbeg and Ryan Baumbauch who assisted with measurements at the National High Magnetic Field Laboratory in Tallahassee, and Todd Sayles whose valiant efforts resulted in the materials necessary for the body of work in Chapter VI. In particular, I wish to acknowledge the work of Cassandra Rayt, who, as an undergraduate, among having contributed in many ways to the work present here, has incredibly steady hands and a knack for placing leads on microscopically small samples. Finally, amongst my coworkers, I would like to express thanks to Jason Jeffries, Nick Butch, and Neil Frederick for useful discussions and for providing ears to bounce ideas off of.

I wish to express my love for my parents who have always supported me in many ways, and instilled within me the desire to always do my best, and for my wife, whose love, patience, and support are deeply appreciated.

And finally I would like to thank an old roommate of mine, Jeffrey Bakkus, who, when I was 18, asked me that burning question, ‘So, why aren’t you going to college?’

A portion of the text and data of Chapter III appears as it will be submitted for publication in the articles, “Evolution of Vortex Dynamics Along the Vortex-Lattice Melting Line,” B. J. Taylor and M. B. Maple; “Quantum Fluctuations, Critical Dynamic Vortex Motion, and the Vortex Solid-Liquid Transition,” B. J. Taylor, D. J. Scanderbeg, M. B. Maple, C. Kwon, and Q. X. Jia. The dissertation author was the primary investigator and author of these articles.

A portion of the text and data of Chapter IV is a reprint of the material as it appears in “Vortex-melting and vortex-glass transitions in a high purity twinned $\text{YBa}_2\text{Cu}_3\text{O}_{7-\delta}$ single crystal,” Phys. Rev. B **68**, 054523 (2003), B. J. Taylor, S.

Li, M. B. Maple, and M. P. Maley. The dissertation author was the primary investigator and author of this article.

A portion of the text and data of Chapter V is a reprint of the material as it appears in “Vortex- and Bragg-glass phases in bulk MgB_2 ,” *Physica C* **387**, 131 (2003), M. B. Maple, B. J. Taylor, S. Li, N. A. Frederick, V. F. Nesterenko, and S. S. Indrakanti; and “Mixed-state flux dynamics in bulk MgB_2 ,” *Physica C* **382**, 177 (2002), S. Li, B. J. Taylor, N. A. Frederick, M. B. Maple, V. F. Nesterenko, and S. S. Indrakanti. The dissertation author was the secondary investigator and author of these articles.

A portion of the text and data of Chapter VI appears as it will be published in the article, “Anomalous critical dynamic behavior of vortices amidst a nascent peak effect in granular CeRu_2 films,” B. J. Taylor, R. E. Baumbach, T. A. Sayles, and M. B. Maple. The dissertation author was the primary investigator and author of this article.

VITA

1992–1994	U.S. Navy
1999	Bachelor of Arts in Physics (with distinction), California State University, San Diego
1999	Bachelor of Arts in Mathematics (with distinction), California State University, San Diego
1999–2006	Research Assistant, University of California, San Diego Advisor: Brian Maple
2000	Teaching Assistant, Department of Physics University of California, San Diego
2006	Doctor of Philosophy University of California, San Diego

PUBLICATIONS

B. J. Taylor and M. B. Maple, “Evolution of Vortex Dynamics Along the Vortex-Lattice Melting Line,” *Phys. Rev. B* *submitted* (2006).

B. J. Taylor, R. E. Baumbach, T. A. Sayles, and M. B. Maple, “Critical Dynamic Fluctuation Amidst a Nascent Peak Effect in Granular CeRu₂ Films,” *Phys. Rev. B* *submitted* (2006).

B. J. Taylor, D. J. Scanderbeg, M. B. Maple, C. Kwon, and Q. X. Jia, “Quantum Fluctuations, Critical Dynamic Vortex Motion, and the Vortex Solid-Liquid Transition,” *Phys. Rev. B* *submitted* (2006).

T. Katuwal, V. Sandu, C. C. Almasan, B. J. Taylor, and M. B. Maple, “High temperature mixed state c-axis dissipation in low carrier density Y_{0.54}Pr_{0.46}Ba₂Cu₃O_{7 δ} ,” *Phys. Rev. B* **73**, 144510 (2006).

S. Liang, R. Islam, David J. Smith, P. A. Bennett, J. R. O’Brien, and B. Taylor “Magnetic iron silicide nanowires on Si $\langle 110 \rangle$,” *Appl. Phys. Lett.* **88**, 113111 (2006).

M. B. Maple, N. A. Frederick, P.-C. Ho, W. M. Yuhasz, T. A. Sayles, N. P. Butch, J. R. Jeffries, and B. J. Taylor, “Novel strongly correlated electron states in filled skutterudite lanthanide osmium antimonides,” *Physica B*, **359**, 830 (2005).

T. Katuwal, V. Sandu, C. C. Almasan, B. J. Taylor, and M. B. Maple, “Vortex dissipation in Y_{1-x}Pr_xBa₂Cu₃O_{6.97} superconductors above and below the zero-field critical temperature,” *Phys. Rev. B* **72**, 174501 (2005).

- W. M. Yuhasz, N. A. Frederick, P. -C. Ho, N. P. Butch, B. J. Taylor, T. A. Sayles, M. B. Maple, J. B. Betts, A. H. Lacerda, P. Rogl, and G. Giester, “Heavy-fermion behavior, crystalline electric field effects, and weak ferromagnetism in $\text{SmOs}_4\text{Sb}_{12}$,” *Phys. Rev. B* **71**, 104402 (2005).
- V. F. Nesterenko, M. B. Maple, B. J. Taylor, and Y. B. Gu, “Modification of Magnesium Diboride Properties Using Shock Loading and Hot Isostatic Pressing,” *AIP Conf. Proc.* **706**, 1114 (2004).
- B. J. Taylor, S. Li, M. B. Maple, and M. P. Maley, “Vortex-melting and vortex-glass transitions in a high purity twinned $\text{YBa}_2\text{Cu}_3\text{O}_{7-\delta}$ single crystal,” *Phys. Rev. B* **68**, 054523 (2003).
- M. B. Maple, B. J. Taylor, S. Li, N. A. Frederick, V. F. Nesterenko, and S. S. Indrakanti “Vortex- and Bragg-glass phases in bulk MgB_2 ,” *Physica C*, **387**, 131 (2003).
- M. B. Maple, B. J. Taylor, N. A. Frederick, S. Li, V. F. Nesterenko, S. S. Indrakanti and M. P. Maley, “Critical scaling and flux dynamics in bulk MgB_2 and high-purity $\text{YBa}_2\text{Cu}_3\text{O}_{7-\delta}$ single crystals,” *Physica C*, **382**, 132 (2002).
- S. Li, B. J. Taylor, N. A. Frederick, M. B. Maple, V. F. Nesterenko, and S. S. Indrakanti “Mixed-state flux dynamics in bulk MgB_2 ,” *Physica C* **382**, 177 (2002).
- E. D. Bauer, A. Slebarski, E. J. Freeman, N. A. Frederick, B. J. Taylor, C. Sirvent, and M. B. Maple, “Strongly correlated electron behavior in $\text{ROs}_4\text{Sb}_{12}$ ($\text{R}=\text{Ce}, \text{Pr}$) filled skutterudites,” *Physica B*, **312**, 230 (2002).

FIELDS OF STUDY

Major Field: Physics

Studies in Superconductivity and Magnetism

M. Brian Maple, Bernd T. Matthias Professor of Physics,
University of California, San Diego

ABSTRACT OF THE DISSERTATION

Vortex Dynamics:

A Window Into the Properties of Type-II Superconductors

by

Benjamin Jeremy Taylor

Doctor of Philosophy in Physics

University of California, San Diego, 2006

Professor M. Brian Maple, Chair

The vortex solid - vortex liquid transition, i. e., the vortex lattice (vortex glass) melting line, $H_m(T)$ ($H_g(T)$) is the most heavily studied phase boundary in the $H - T$ phase diagram of type-II superconductors. Debate has continued for many decades as to the nature of the transition and of the vortices themselves. The vortex glass melting transition has been investigated in the type-II superconducting compounds $\text{YBa}_2\text{Cu}_3\text{O}_{7-\delta}$, $\text{YBa}_2\text{Cu}_3\text{O}_{6.5}$, $\text{Y}_{1-x}\text{Pr}_x\text{Ba}_2\text{Cu}_3\text{O}_{6.97}$, MgB_2 , and CeRu_2 . By performing measurements of magnetoresistivity, $\rho(H, T)$, voltage-current $V - I$, and magnetization, $M(H, T)$, and by analyzing the behavior in the region of the melting transition, physical properties of the host materials and how these contribute to the nature of the melting transition have been revealed.

I

Introduction

After nearly two decades since the discovery of high temperature superconductivity [1], the phase diagram of vortex matter in type-II superconductors continues to be a source of debate. Certainly, the most experimentally and theoretically investigated feature of the phase diagram is the vortex lattice (or vortex glass) melting line, $H_m(T)$ ($H_g(T)$), the boundary at which the vortex matter undergoes a change from an immobile solid state to an electrically dissipative liquid state. Achieving an understanding of the nature of this transition over the entire range of magnetic field and temperature, within materials with disparate normal state and superconducting properties, and with various types of disorder is of the utmost importance if a truly universal picture of the vortex matter phase diagram is to be developed. As new and theoretically predicted behavior is experimentally observed and/ or confirmed, such as the Bragg-glass phase [2, 3, 4] and non-hexagonal vortex lattice structures in superconductors with anisotropic band structures or energy gaps [5, 6, 7], the fact that the superconductor is more than a mere host for the vortex matter, and that vortices are more than an engineering obstacle for applications, has become more widely appreciated. While it has long been recognized that the physical properties of the host have consequences for the dynamical behavior of vortex flux lines and the order/disorder of the vortex-lattice, it is becoming more apparent that the presence of the vortices is the source of some

of the physical changes of the superconductor [8]. A study of the behavior of the vortex-matter can provide insight into the electronic and structural properties of the host, beyond that of strictly disorder/impurity concerns.

The work presented in the following chapters consists of the study of vortex dynamics in type-II superconductors, with the goal of gaining insight into key properties of the material system. The intrinsic properties of the superconducting materials examined here are vastly different, yet by analyzing the dynamical properties of vortices at the vortex-solid to vortex-liquid transition valuable information has been gained in each case. The systems examined include the novel low-temperature superconductor CeRu₂ ($T_c \sim 6\text{K}$), the two gap mid-temperature superconductor MgB₂ ($T_c \sim 40\text{K}$), and the high- T_c cuprate superconductors YBa₂Cu₃O_{7- δ} , YBa₂Cu₃O_{6.5}, and Y_{1-x}Pr_xBa₂Cu₃O_{6.97} ($T_c \sim 20\text{ K} - 90\text{ K}$).

I.A Superconductivity

Materials in a metallic state are characterized by having a high electrical and thermal conductivity; they have a large number of electrons which are free to move about. In simple models, the electrons within a metallic material are treated as free, independent particles. The electrical and thermal properties are described fairly well by models which treat the electrons as independent particles. In many metallic elements and alloys, (and even in certain semiconductors under appropriate conditions [9]), an electronically ordered state, the superconducting state, is abruptly established at very low temperatures below a critical temperature, T_c . Superconductivity, however, is not limited to low temperatures, as demonstrated by the numerous cuprate based high-temperature superconductors, whose critical temperatures, T_c , are an order of magnitude greater than most conventional superconductors [10]. The defining characteristics of a superconductor are: (1) The material is able to transport an electrical current without any measurable dissipation, (2) It behaves as a perfect diamagnet. A sample in thermal equilibrium and

in the presence of an applied magnetic field with a strength below a characteristic value, H_c , carries surface currents which flow in a manner that results in the canceling of the applied field strength internal to the sample. (3) The formation of an energy gap, 2Δ , centered about the Fermi energy, ε_F , associated with the pairing energy of the superconducting electrons. The addition or subtraction of an electron from the superconducting state requires an energy ε such that $\varepsilon - \varepsilon_F > \Delta$. There are situations where the formation of an energy gap is not a necessary condition for superfluidity, but this is not usually the case [11].

I.A.1 BCS theory of superconductivity

The microscopic theory of superconductivity proposed by Bardeen, Cooper, and Schrieffer in 1957 (BCS theory) [12] explains the phenomenon as resulting from a net attraction between electrons, in spite of their repulsive electrostatic interaction. In the case of conventional low temperature superconductors, an attractive force is provided by a screening action produced by ionic motion, referred to as the electron-phonon interaction. In a simplified picture, an ion will move towards the region of a passing electron, and subsequently the displaced ion draws a second electron towards this new location and then will return back towards its equilibrium position, allowing the second electron to pass. The result is an effective attractive force, with an associated isotropic energy gap Δ , binding the electrons together in correlated, dissipation free, motion. The spatial extent of the paired electrons can be related to the energy gap by the equation,

$$\xi_0 = \frac{\hbar v_F}{\pi \Delta}, \quad (\text{I.1})$$

where ξ_0 is the Cooper pair coherence length, and v_F is the Fermi velocity. The electron-phonon mechanism has long since been verified in conventional superconductors through the observation of the isotope effect [13, 14], whereby a change of the ionic mass, M , by substitution with an isotope results in a shift of the characteristic frequency at which the ion oscillates and thus shifts the binding energy

associated with the paired electron, leading to the result, $T_c \propto M^{-\alpha}$. In conventional superconductors the energy gap is isotropic, so that pairing is of the spin singlet $S = 0$ type, with s -wave $L = 0$ symmetry. BCS theory however does not require that phonons provide the pairing mechanism, and as such, other mechanisms are possible which can lead to an anisotropic energy gap and non s -wave pairing. In the high- T_c cuprate superconductors (and other unconventional superconductors) the pairing mechanism is thought by many to be due to magnetic fluctuations, though this has been under investigation for many years and no consensus has yet been reached. Experimental evidence strongly indicates that the pairing mechanism in the cuprate superconductors is d -wave in nature [15].

I.B Type I

In superconductors which are referred to as type I, at temperatures below the critical superconducting temperature T_c and below a critical field, $H_c(T)$, that is increasing as the temperatures decreases, there is no penetration of the magnetic field into the body of the material. This condition is known as the Meissner state. When the sample geometry is ideal and the applied field exceeds the critical value, the field penetrates the sample fully and superconductivity is completely destroyed. However, in a sample with non ideal geometry, when the applied field is close to the bulk critical field, the field will penetrate fully into macroscopic regions of the superconductor, with adjacent regions remaining superconducting. This is referred to as the intermediate state.

I.B.1 The London equation

F. London and H. London were the first to quantitatively examine the fundamental fact that a metal in the superconducting state excludes a magnetic field from its interior [16]. From consideration of the situation where an electric field momentarily arises within a superconductor, resulting in the superconducting

electrons, of density n_s , being freely accelerated without dissipation with a current density $\mathbf{j} = -e\mathbf{v}_s n_s$, and by use of Faradays law of induction,

$$\nabla \times \mathbf{E} = -\frac{1}{c} \frac{\partial \mathbf{B}}{\partial t}$$

the relation between the current density and magnetic field in a superconductor in which no magnetic field is permitted in the interior is found to be,

$$\nabla \times \mathbf{j} = \frac{-n_s e^2}{mc} \mathbf{B}. \quad (\text{I.2})$$

Eq. (I.2) together with the Maxwell equation, $\nabla \times \mathbf{B} = (4\pi/c)\mathbf{j}$ gives the equations

$$\begin{aligned} \nabla^2 \mathbf{B} &= \frac{4\pi n_s e^2}{mc^2} \mathbf{B} \\ \nabla^2 \mathbf{j} &= \frac{4\pi n_s e^2}{mc^2} \mathbf{j} \end{aligned}$$

which in turn predict that currents and magnetic fields in superconductors only exist at the surface in a thin layer with thickness,

$$\lambda_L = \left(\frac{mc^2}{4\pi n_s e^2} \right)^{1/2},$$

and thus implies the Meissner effect along with the scenario of surface currents screening out the applied field.

I.C Type II

In magnetic fields below a lower critical field, $H_{c1}(T)$, type II superconductors also expel an applied magnetic field in the same manner as a type I superconductor. However, in fields H above $H_{c1}(T)$ and below an upper critical field, $H_{c2}(T)$, the magnetic field is able to penetrate the sample *without* destroying the superconductivity [17]. This is accomplished by means of a partial penetration wherein the formation of supercurrent vortices, or vortex flux lines takes place, a condition referred to as the mixed state. The cores of the vortices consist of normal state electrons and the magnetic field is able to pass through these regions. This

difference between type I and type II superconductors is explained by a fundamental property of superconducting materials. When an applied field penetrates into the surface of the material, as described above, there is an energy associated with the boundary separating the normal regions and the superconducting regions. In type I superconductors this surface energy, σ_{sn} , is positive and the stable state is the intermediate state. In type II superconductors σ_{sn} is negative and the energy of the system is lowered by the formation of vortices [15].

The mixed state is further divided into two regions: Below a characteristic field value, $H_m(T)$, the vortex ensemble is “frozen,” *i. e.* in a solid immobile state in which, for applied currents not exceeding a critical value, the superconductor retains the characteristic property of dissipation free current transport. At fields above this value the vortex solid “melts” into a “liquid” phase where individual vortex motion is possible and an applied current results in a measurable loss of power. Depending upon the level of disorder within the superconductor, the solid vortex state will either consist of a regular array of flux lines, the vortex lattice, or, an irregular distribution of flux lines, referred to as a vortex glass.

I.C.1 Ginzburg-Landau theory

Ginzburg and Landau [18] put forth the idea that the superconducting state should be described by a complex order parameter $\psi(\mathbf{r}) = |\psi|e^{i\phi}$ which vanishes above T_c and whose magnitude, $|\psi|$, is a measure of the degree of superconducting order below T_c at a position \mathbf{r} . In the context of BCS theory the order parameter can be viewed as a single particle wave function describing the center of mass of a Cooper pair. A fundamental aspect of the theory of Ginzburg and Landau is that current flowing through the superconductor in the presence of a magnetic field, described through the vector potential $\mathbf{A}(\mathbf{r})$, is given by the quantum mechanical formula for a particle of charge $-2e$ and mass $2m$. The assumption that Cooper pairs can flow, but will not accumulate or be lost from the system

leads to the relation

$$\mathbf{j} = - \left[\frac{2e^2}{mc} \mathbf{A} + \frac{e\hbar}{m} \nabla \phi \right] |\psi|^2. \quad (\text{I.3})$$

Since currents can only flow near the surface of the superconductor Eq. (I.3) leads to

$$\oint \mathbf{j} \cdot d\ell = 0$$

giving the fundamental result that a magnetic field penetrating a type-II superconductor will thread through the superconductor in quantized units of magnetic flux,

$$|\Phi| = \frac{n\hbar c}{2e} = n\Phi_0,$$

where $\Phi_0 = \hbar c/2e = 2.068 \times 10^{-15} \text{ T m}^2$ is the single flux quantum.

I.D Vortex dynamics

A number of forces act upon the moving vortex line in a type-II superconductor. Accounting accurately for their combined effects is a difficult task. The most familiar vortex equation of motion balances the the Lorentz force, which is exerted by an electric current density \mathbf{j} flowing perpendicular to the flux line length direction, $\hat{\mathbf{z}}$, which produces a transverse motion of the vortex flux line \mathbf{v}_L , with the Bardeen-Stephen friction force, caused by dissipative scattering in the vortex core,

$$\mathbf{f}_L + \mathbf{f}_{BS} = \Phi_0 \mathbf{j} \wedge \hat{\mathbf{z}} - \eta_\ell \mathbf{v}_L = 0,$$

where Φ_0 is the quantum of magnetic flux. The viscous drag coefficient η_ℓ , derived by Bardeen and Stephen [19], is given by,

$$\eta_\ell = \frac{\phi_0^2 \sigma_N}{2\pi \xi^2},$$

where σ_N is the normal state conductivity, and $\xi = \xi_0/(1 - T/T_c)^{1/2}$ is the temperature dependent Cooper pair correlation length. A moving vortex flux line, with velocity \mathbf{v}_L , also experiences an additional force, $\rho_s \Phi_0 [\mathbf{v}_L \wedge \hat{\mathbf{z}}]$ that drives it along the current direction, $\hat{\mathbf{j}}$, where ρ_s is the superfluid current density. The

modified Lorentz force is then given by $\mathbf{f}_L = \Phi_0(\rho_s \hat{\mathbf{j}} + \mathbf{j}) \wedge \hat{\mathbf{z}}$. The vortex flux line motion produces an electric field in the direction of the driving current density, $\mathbf{E} = \Phi_0 \hat{\mathbf{z}} \wedge \mathbf{v}_L$, resulting in a dissipation of power, $P = (\mathbf{j} \wedge \mathbf{B})^2 / \eta_\ell$, thus the superconducting property of dissipation free current flow is destroyed. Fortunately though, vortices interact with various defects in the host material, and are effectively pinned by a force characteristic to the nature of the defects. So, while the presence of defects will degrade superconductivity within the bulk material, a small to moderate amount of disorder will actually improve the supercurrent carrying capacity of the bulk materials in magnetic fields.

Within the solid phase of the vortex matter, there are two main vortex pinning regimes: The single vortex pinning scenario at very low fields, and / or at temperatures well below T_c , and the collective vortex bundle pinning regime, which is realized over the majority of the solid phase, and, most importantly, occupies the region of the $H - T$ phase diagram along the vortex solid – vortex liquid transition (except at extremely low fields), *i. e.* the boundary defined by the vortex lattice melting line, $H_m(T)$, or the vortex glass melting line, $H_g(T)$ [15, 20]. The collective nature of the vortices leads to the either the first order melting of the vortex lattice with a corresponding jump in magnetization and entropy [21, 22], or a second order melting of the vortex glass phase [23, 24].

The dynamic properties of vortices in the region of the continuous vortex glass melting transition is addressed in the theory of Fisher, Fisher, and Huse [24]. First proposed by M. P. A. Fisher [23], the vortex glass theory describes the emerging critical behavior of the vortex ensemble in the presence of random point disorder in terms of a diverging correlation length scale, $\xi_{VG} \sim |T - T_g|^{-\nu}$ and correlation time $\tau_{VG} \sim \xi_{VG}^z$, where T_g is the critical transition temperature, and ν and z are the correlation length- and dynamical exponents, respectively. Correlated disorder results in the Bose glass phase [25], also described in terms of a diverging length scale, and time, ξ_{BG} and $\tau_{BG} \sim \xi_{BG}'^z$. The two models are seen to be related though via renormalization group theory analysis [26], and from

the scaling properties of the superfluid density [27]. This topic is given more consideration in Chapter III. By measuring various transport properties in the critical region, the values of the critical exponents can be determined. In the context of various models, many physical properties of the host material can be inferred from the values of the critical exponents.

Bibliography

- [1] J. G. Bednorz and K. A. Müller, Z. Phys. B. **64**, 189 (1986).
- [2] T. Giamarchi and P. Le Doussal Phys. Rev. B. **52**, 1242 (1995).
- [3] H. Safar, P. L. Gammel, D. A. Huse, and D. J. Bishop, Phys. Rev. Lett. **70**, 3800 (1993).
- [4] U. Yaron, P. L. Gammel, D. A. Huse, R. N. Kleiman, C. S. Oglesby, E. Bucher, B. Batlogg, D. J. Bishop, K. Mortensen and K. Clausen, C. A. Bolle, and F. De La Cruz, Phys. Rev. Lett. **73**, 2748 (1994).
- [5] K. Takanaka, Prog. Theor. Phys. **46**, 1301 (1971).
- [6] K. Fischer and H. Teichler, Phys Lett. **58A**, 402 (1976).
- [7] Anisotropy Effects in Superconductors, edited by H. W. Weber (Plenum, New York, 1977).
- [8] R. Lortz, C. Meingast, U. Welp, W. K. Kwok, and G. W. Crabtree, Phys. Rev. Lett. **90**, 237002 (2003).
- [9] N. W. Ashcroft and N. D. Mermin, *Solid State Physics*, Harcourt College Publishers, Fort Worth, 1976.
- [10] H. W. Weber, Ed., *High- T_c Superconductors*, Plenum Press, New York and London, 1988.
- [11] P. G. DeGennes, *Superconductivity of Metals and Alloys*, W. A. Benjamin, Inc., New York, Amsterdam, 1966.
- [12] J. Bardeen, L. N. Cooper, and J. R. Schrieffer, Phys. Rev. **108**, 1175 (1957).
- [13] E. Maxwell, Phys. Rev. **78**, 477 (1950).
- [14] C. A. Reynolds, B. Serin, W. H. Wright, and L. B. Nesbitt, Phys. Rev. **78**, 487 (1950).
- [15] K. H. Bennemann and J. B. Ketterson (Eds.), *The Physics of Superconductors, Vol I., Conventional and High- T_c Superconductors* Springer-Verlag, Berlin Heidelberg, New York, 2003, (and references within).
- [16] F. London and H. London, Proc. Roy. Soc. (London) **A149**, 71 (1935), Physica **2**, 341 (1935).
- [17] A. A. Abrikosov, Zh. Eksp. Teor. Fiz. **32**, 1442 (1957).
- [18] V. L. Ginzburg and L. D. Landau, Zh. Eksp. Teor. Fiz. **20**, 1064 (1950).
- [19] J. Bardeen and M. J. Stephen, Phys. Rev. **140**, A1197 (1965).

- [20] G. Blatter, M. V. Feigel'man, V. B. Geshkenbein, A. I. Larkin, and V. M. Vinokur, *Rev. Mod. Phys.* **66**, 1125 (1994).
- [21] A. Schilling, R. A. Fisher, N. E. Phillips, U. Welp, D. Dasgupta, W. K. Kwok, and G. W. Crabtree, *Nature* **382**, 791 (1996).
- [22] M. J. W. Dodgson, V. B. Geshkenbein, H. Nordborg, and G. Blatter, *Phys. Rev. Lett.* **80**, 837 (1998).
- [23] M. P. A. Fisher, *Phys. Rev. Lett.* **62**, 1415 (1989).
- [24] D. S. Fisher, M. P. A. Fisher, and D. A. Huse, *Phys. Rev. B* **43**, 130 (1991).
- [25] D.R. Nelson and V.M. Vinokur, *Phys. Rev. Lett.* **68**, 2398 (1992); *Phys. Rev. B* **48**, 13060 (1993).
- [26] T. Hwa, D. R. Nelson, and V. M. Vinokur, *Phys. Rev. B* **48**, 1167 (1993).
- [27] J. Lidmar and M. Wallin, *Europhys. Lett.* **47**, 494 (1999).

II

Experimental Apparatus and Measurement Methods

II.A The pulsed laser ablation deposition technique

The use of a pulsed UV laser beam for vaporizing solid source material has been established as a standard technique for film deposition of many materials. Thin films are often grown to achieve properties or conditions unattainable in bulk or single crystal form. Further motivation to fabricate materials as films includes being able to explore phenomena of interest in controlled geometries not otherwise possible. In Chapters III and VI experimental studies on epitaxial films of $\text{Y}_{1-x}\text{Pr}_x\text{Ba}_2\text{Cu}_3\text{O}_{6.97}$ and granular films of CeRu_2 , both grown by the pulsed laser deposition method, are presented respectively. The $\text{Y}_{1-x}\text{Pr}_x\text{Ba}_2\text{Cu}_3\text{O}_{6.97}$ films were fabricated by Chuhee Kwon at the Los Alamos National Laboratory. The films of CeRu_2 were made by the author and coworkers in a specialized system described in the following section. Here, the method of pulsed laser ablation is briefly described. For a complete discussion of film growth in general and growth by pulsed laser deposition (PLD) see refs. [1, 2, 3].

The basic process for growth of a film by PLD is as follows: A large mass of target material is fashioned so that it has a flat surface, typically in the shape of

a disc, and mounted on a rotating assembly. A crystalline substrate material with a polished surface, upon which the film will be grown, is placed upon or adhered to a heater block assembly. The two assemblies are inserted into a vacuum chamber (see Figs. II.1 and II.2) in a geometry so that the target and substrate surfaces are opposite of each other at a distance typically ranging from 2 - 10 cm. The chamber is then pumped out to high vacuum pressures, and, depending on the material to be deposited, is either baked out at high vacuum and backfilled to a low pressure with an inert gas to achieve ultraclean atmospheric conditions, or backfilled with a reactive gas which takes part in the chemical dynamics of the growth process of the film. When the atmospheric conditions are suitable and the temperature of the substrate set to a desired value, the laser beam can be activated for ablation of the target material. The target is rotated to maintain a fresh surface for ablation, preventing the formation of a pit and also preventing superheating of a small region of the target. Both of these conditions can result in preferential ablation of constituent elements of the target material, resulting in an film with an undesired stoichiometry. The parameters to be varied or controlled during the growth process include the incident laser energy density at the target surface, the temperature of the substrate, the pressure and type of gas, and the target to substrate distance.

The growth of intermetallic films requires a vacuum chamber system capable of being pumped down to pressures in the UHV range, $p \sim 10^{-8} - 10^{-10}$ torr. The atmospheric conditions under which the films are grown must be non-reactive, *i. e.* oxygen free. To achieve this condition the chamber as well as the heater block assembly must be baked out during the pump down process. Heater strips on the outside of the chamber heat the chamber walls to 100° C. The heater block is set to 200° C. Care must be taken to avoid excessive heating of the pressure gauges as this will damage them. A table top fan provides sufficient cooling for this purpose. Typical bake out times of 18 - 36 hours are adequate to achieve a base pressure of $p \sim 10^{-9}$ torr.

Excimer lasers are capable of producing beams with wavelengths in the UV spectrum, ranging from $\lambda = 152$ nm (F_2) to $\lambda = 351$ nm (XeF). The laser used in the system described below uses a KrF gas mix which outputs a wavelength of $\lambda = 248$ nm. By focusing the beam with appropriate optics, it is possible to obtain energy densities as high as 100 J/cm² at the surface of the ablation target material.

II.A.1 Development of a unique laser ablation chamber for growth of volatile inter-metallic films

Intermetallic films are commonly grown by either evaporation or sputtering methods. The method of pulsed laser deposition is much more difficult for this class of materials. The combined properties of a target material which has a highly reflective metallic surface, and, a compound consisting of highly reactive elemental constituents, as well as constituents with vastly different vapor pressures, make the growth of such films by PLD quite a challenge. However, growth of intermetallic films by PLD has some advantages as well, including the ability to routinely fabricate an array of custom targets for unique experimental investigations.

A UHV vacuum chamber system was constructed for the purpose of growing high quality film samples of $CeRu_2$ as well as other various intermetallic compounds. As stated above, materials which consist of highly reactive constituents with significantly different vapor pressures are a challenge to produce. The main obstacle is that the volatile element will disperse throughout the chamber during the deposition process, covering all surfaces with a film. This is particularly detrimental to the growth process because, as the ablation process continues, a film deposits on the window through which the laser beam enters the chamber, reducing the energy which reaches the target. As this process continues the laser energy which passes through the window drops below that necessary for proper ablation conditions, resulting in films with compositional variance throughout its thickness. In addition to producing films which are not of high quality, the energy

degradation phenomenon makes exploration of the proper growth conditions for new materials almost impossible, since laser energy density at the target surface is an important variable in the growth process. Furthermore, the film deposited on the window is heated by the laser resulting in rapid damage to the window which reduces the ability of the window to pass the UV laser beam. The damaged windows must be replaced, leading to prohibitive costs.

A unique technique was explored and developed which makes possible the routine growth of volatile intermetallic films, overcoming this technical hurdle. As shown in Fig. II.1, a barrier to the spread of the vaporized target material to the laser window surface is provided by a pressurized canister. This canister is actually an insert made of thin wall stainless steel foil, spot welded with ends having openings just large enough to pass the laser beam profile. An additional hole in the end closest to the deposition region is made in order to pass through a stainless steel gas line into the canister. With the base pressure after bake out at $p \sim 10^{-8}$ torr, prior to activating the laser, UHP argon gas is flowed into the chamber via the pressurized canister, raising the pressure measured at the opposite end of the chamber to $p \sim 10^{-5}$ torr. The gas is flowed during the entire deposition time. The resulting pressure gradient effectively contains the vaporized target material to the main chamber preventing any material from reaching the laser window. The CeRu₂ films discussed in Chapter VI were grown in this one-of-a-kind chamber using the procedure described above.

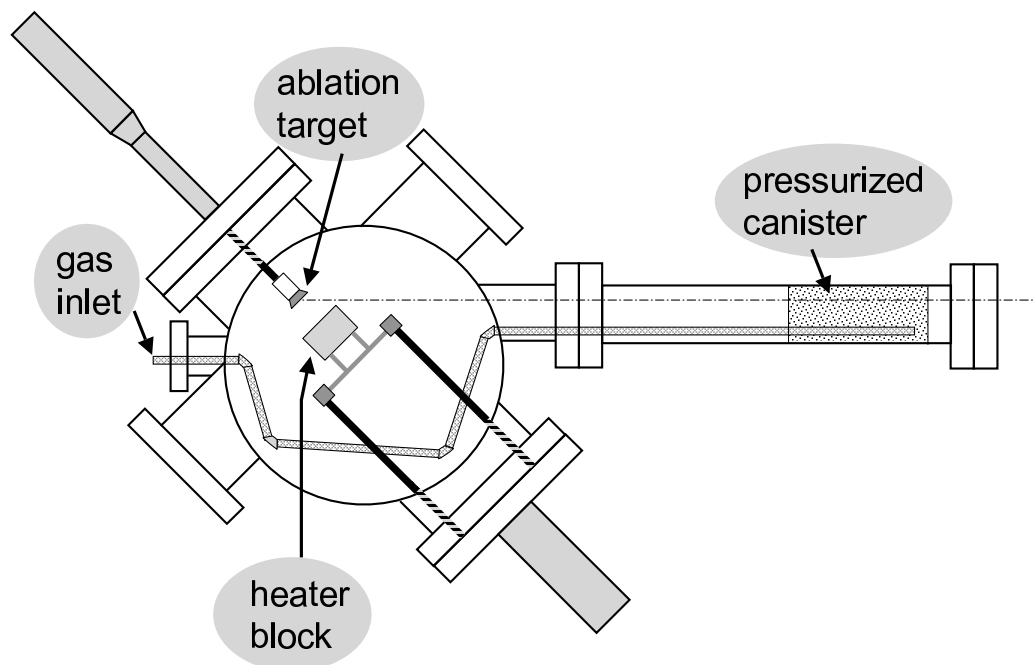


Figure II.1: Schematic of a pulsed laser ablation ultra high vacuum deposition chamber, designed for growth of volatile intermetallic films. The key component of the system is the pressurized canister which prevents vaporized material from reaching the laser window. The beam path, indicated by the dashed line, passes through the pressurized canister to the target surface. Argon gas flows from the canister region to the turbo pump shown in the following figure.

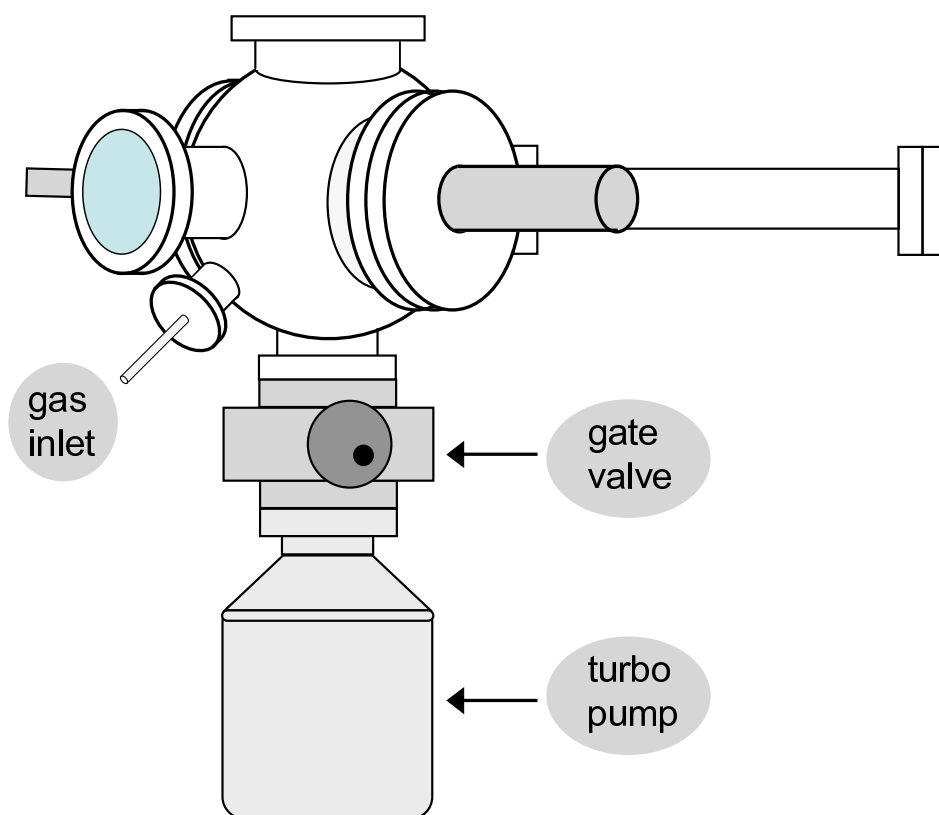


Figure II.2: Side view of the pulsed laser ablation ultra high vacuum deposition system. The mechanical pump, gas control panel, and electronics are not shown.

II.B Measurements

II.B.1 X-rays

Standard theta-2theta x-ray diffraction measurements of target materials and films were made using an industry standard Rigaku D/MAX B x-ray machine, to verify the sample composition and film growth orientation. The peaks in the resulting diffraction pattern were compared to the literature. Each peak was associated with an $\langle h, k, l \rangle$ number for a symmetry plane of the crystal or standard, or with an impurity peak.

II.B.2 Magnetization

Measurements of dc magnetization as a function of field and temperature, $M(H, T)$, were made in a commercial Quantum Design superconducting quantum interference device (SQUID) magnetometer. Samples were mounted on or between thin discs of teflon in a standard clear drinking straw, with the disc surfaces perpendicular to the field direction. Film samples were mounted with their surface either parallel or perpendicular to the field direction.

II.B.3 Electrical resistivity & Electric field-current density measurements

Electrical resistivity, $\rho(H, T)$, and electric field-current density, $E - J$, isotherms were measured in lab in a Quantum Design Physical Property Measurement System in temperatures $1.8 \text{ K} \leq T \leq 300 \text{ K}$ and fields $0 \text{ T} \leq H \leq 9 \text{ T}$. Additional measurements made in high magnetic fields were performed at the National High Magnetic Field Laboratory in Tallahassee, FL in a 32 tesla DC Bitter resistive magnet, and in a 45 tesla hybrid magnet. Gold wire (1 or 2 mil) was attached to single crystal and bulk samples with silver epoxy in the standard four-wire configuration. Leads for films were attached by pressing gold wire into indium pads which were bonded to gold pads on the film surface. Resistivity and $E - J$

data were measured with a Keithly 2182 nanovoltmeter and Keithly 2182 current source in all systems.

Bibliography

- [1] D. B. Chrisey and G. K. Huber, *Pulsed Laser Deposition of Thin Films*. John Wiley & Sons, Inc., New York, 1994.
- [2] D. L. Smith, *Thin-Film Deposition*. McGraw-Hill, Inc., 1995.
- [3] M. Ohring, *Materials Science of Thin Films, Deposition and Structure*, 2nd Edition. Academic Press, 2002.

III

Quantum Fluctuations, Vortex Flux Line Dynamics, and the Vortex-Solid to Vortex-Liquid Transition

III.A Introduction

Since the discovery of the high-temperature layered cuprate superconductors, the physics of the mixed state of strongly type-II superconductors has received considerable attention. A significant amount of effort has been devoted to developing a consistent theory of the melting transition of the vortex lattice. As there are many processes to be taken into consideration – thermal and quantum fluctuations, pinning mechanisms, anisotropy, coupling of the vortex lattice to the underlying electronic structure, and the critical dynamics of vortex motion as the melting transition is approached – arriving at an expression that is relevant over the entire vortex lattice melting line has proven elusive.

It is well understood that disorder within the superconductor is an important aspect of the physical picture under consideration. In a sufficiently clean

superconductor, vortex lines will penetrate the sample in a regular array forming a lattice. As the temperature of the sample is increased, eventually the vortex lattice will undergo a first order melting transition, with a corresponding jump in entropy and magnetization [1, 2]. The introduction of disorder or defects into a superconducting sample creates regions to which the normal cores of the vortices are attracted to, pinning the vortex to the site and producing a barrier to motion, thus enhancing the ability of the sample to carry an electrical current without dissipation, and subsequently destroying the long range order of the vortex lattice. The result is a variety of glassy vortex states [3]. The glassy phases can each be characterized by an exponent μ , describing their dynamical response where, as an applied current density goes to zero, the defect barriers impeding vortex motion diverge, $U(j \rightarrow 0) \sim U_c(j_c/j)^\mu$, and the vortex velocity goes to zero as $v \propto \exp[-U(j)/T]$. Alternatively, the effect of defect barriers on the dynamical properties of the vortices can be described by via a critical exponent, \tilde{s} characterizing the vanishing of resistivity as the temperature approaches from above a critical value, T_g , so that $\rho(T) \sim (T - T_g)^{\tilde{s}}$. The critical exponent \tilde{s} is itself a product of the static critical exponent, ν , and, depending on the kind of vortex glass, a factor composed of an expression involving the dynamical exponent, z , the dimensionality of the system, d , and an anisotropy exponent, ζ .

The introduction of random point disorder results in the “original” vortex glass (VG) considered by Fisher, Fisher, and Huse [4, 5]. Correlated columnar disorder, such as that introduced by ion bombardment, produces the Bose glass (BG) state [6]. In the case of extremely weak point disorder the vortex lattice, while distorted, is able to maintain short range order and is characterized by the absence of lattice dislocations. The preservation of long range periodicity is sufficient so that Bragg diffraction peaks are observed in scattering experiments, hence the name, Bragg glass (BrG) [7]. The pinning environments within a vortex glass and a Bose glass differ significantly in that point disorder encourages wandering of the vortex through the sample to seek out pinning centers, but in contrast, columnar

defects inhibit line wandering. Additionally, point disorder is isotropic with respect to the direction of the vortex lines, but columnar disorder produces an anisotropic environment within a few degrees of the alignment of the field to the columns, with corresponding angular dependences.

In spite of the difference of dynamical properties within the region of the melting transitions, the vortex glass and Bose glass are described by critical behavior with a very similar formalism, based upon the critical scaling properties of the superfluid density, resulting only in differing expressions for the critical exponents [5, 6, 8]. It has been shown that the vortex glass phase is recovered from the Bose-glass phase as correlated disorder becomes irrelevant, either by strong point disorder or the absence of correlated disorder [9]. The theoretical foundation employed to describe the Bragg glass state arises from the weak disorder case of the same Hamiltonian that was originally proposed to describe the vortex glass state [7, 10]. While the Bragg glass is expected to undergo a first order melting transition to a vortex liquid with increasing temperature, some experimental evidence and theoretical models suggest that the vortex glass state lies in a narrow region between the Bragg glass region and the melting line [11, 12]. Even though these three solid vortex phases have distinct properties it should be apparent that the dynamical properties of the vortices in the melting region of each kind of glass are quite related. Henceforth, in this chapter, the term vortex glass shall be used to encompass both the vortex- and Bose-glass ensembles, keeping in mind the different critical exponents. The Bragg-glass will be left as a separate case for now. The abbreviations VG or BG are used to indicate a specific type of vortex glass.

Theoretical analysis of the problem of the melting transition is complicated and a consistent theory describing a melting scenario is known for only a few special cases, the pancake-vortex system, treated via a self-consistent stability analysis [13], and a dislocation-mediated melting scenario in 2-dimensions [14] and in 3-dimensions [15]. The latter case allows for a unified phase diagram which includes all three vortex phases. However, this theory does not provide an explicit

temperature dependent form of the vortex glass to vortex liquid transition.

Absent a consistent theory, a Lindemann type criterion has often been employed. This criterion predicts a melting transition generally when the mean squared amplitude of fluctuations of a lattice approaches a sizable fraction of the lattice constant a_0 , $\langle u^2(T_m) \rangle \approx c_L^2 a_0^2$, where $c_L \sim 0.1 - 0.3$ ($a_0 \approx (\Phi_0/B)^2$ for a vortex lattice). A Lindemann type analysis of the vortex flux line displacements, leads to the classical thermal fluctuation result [16, 17],

$$B_m \approx \beta_m (c_L^4 / G_i) H_{c2}(0) (1 - t)^2,$$

where $G_i = [T_c / H_c^2(0) \epsilon \xi^3(0)]^2 / 2$ is the Ginzburg number, $\xi(0)$ is the in-plane superconducting coherence length, $H_c(0)$, and $H_{c2}(0)$ are the thermodynamic and upper critical fields, and $\beta_m \approx 2.5$ [18].

The Lindemann criterion approach has resulted in many theoretical and phenomenologically derived expressions which are expected to describe the shape of the vortex lattice melting line, $H_g(T)$, over specific ranges of magnetic field and temperature, and for various specific material conditions. For example, by taking into account the dominant conditions for each of the three cases of an electromagnetically coupled layered superconductor, a Josephson coupled layered superconductor, and a continuous anisotropic superconductor, three separate expressions are found to describe each scenario [10]. The first two cases describe the mid-temperature / mid-field and high-temperature / low field regions of a weakly coupled superconductor, respectively. The latter case describes the mid-high temperature / mid-low field region of a well coupled (anisotropic) superconductor. Each of the two cases then give way to a 2-d expression for the melting line at low-temperatures / high-fields.

More recent (Lindemann criterion based) theoretical efforts have arrived at quite different expressions for the vortex lattice (or glass) melting line, each of which also break the melting line into two or three segments, to account for dominant behavior in the various temperature-field regions [19, 20]. In addition to

accounting for the effects of disorder on destroying the vortex solid phase, the only source of vortex displacements considered in these models are thermal fluctuations.

Blatter and Ivlev have shown some time ago that quantum fluctuations are also a relevant source of vortex line displacements, particularly in the high- T_c superconductors [18, 21]. It should be understood that the vortex lattice melting line proposed by Blatter and Ivlev is not an interpolation formula between quantum and classical limits. Instead, quantum fluctuations are accounted for by going to a dynamical description where the relevant functional is the Euclidean action. The resultant quantum problem is then a $(d+1)$ -dimensional generalization of the d -dimensional classical problem with the additional dimension describing the dynamics of the system (in imaginary time). What the model proposed by Blatter and Ivlev shows is that quantum fluctuations are present for all temperatures, but are most relevant above a characteristic magnetic field. In the high- T_c cuprates they find that this field is ~ 2 -3 tesla, and so quantum fluctuations must be accounted for over the majority of the melting line.

In this chapter an experimental investigation of the vortex glass melting lines, $H_g(T)$, of $Y_{1-x}Pr_xBa_2Cu_3O_{6.97}$ thin film samples ($x = 0 - 0.4$) and an ultra high purity oxygen deficient $YBa_2Cu_3O_{6.5}$ single crystal in magnetic fields up to 45 tesla is presented. These measurements have made it possible to examine the evolution of vortex dynamics over a significantly greater portion of the melting line heretofore explored of this important high- T_c superconducting system. The complex problem of the vortex lattice melting transition is approached here starting from the universal form of the vortex lattice melting line of Blatter and Ivlev [18, 21]. It is found here that the *entire* $H_g(T)$ lines of all samples can be described by a modified form of their vortex lattice melting line expression. The key modification involves the introduction of a single vortex line relaxation time of the form,

$$\tau_r^v = \tau_0 \left(\frac{T}{T_c} \right)^s \left(1 - \frac{T}{T_c} \right)^{-s}, \quad (\text{III.1})$$

which is evaluated along the melting line at $T = T_g$.

It is proposed below that the above expression for τ_r can be obtained naturally from the scaling expression for the fluctuation conductivity [5, 22], and, that the exponent s is the critical scaling exponent associated with the vanishing of resistivity, $\rho \sim (T - T_g)^s$ at the critical temperature, T_g , where s is either that found from the vortex glass model of Fisher, Fisher, and Huse [5], or the Bose glass model of Nelson and Vinokur [6]. The value of s found by the fitting of the melting line expression to the data is seen to be in very good agreement with that found by a scaling of the resistivity data as described above. Any changes in the critical behavior of the vortex lattice along the melting transition, *i. e.*, a change of the value of the critical exponent, will be reflected in the expression for the melting line describing each section with the different exponents. A vortex lattice in a highly anisotropic material, such as the high- T_c cuprates, may undergo a transition from a 3D to a 2D (or quasi 2D) like structure at a characteristic temperature or field, when the interaction between vortex lines within a Cu-O plane becomes comparable to the elastic strength of a single vortex line, resulting in a decoupling of the pancake vortices [10]. We find that our new expression for the melting transition line describes the *entire* vortex glass melting lines of $\text{Y}_{1-x}\text{Pr}_x\text{Ba}_2\text{Cu}_3\text{O}_{6.97}$ ($x = 0 - 0.4$) thin film and $\text{YBa}_2\text{Cu}_3\text{O}_{6.5}$ single crystal samples as well as that of a $\text{Sm}_{1.85}\text{Ce}_{0.15}\text{CuO}_{4-y}$ film ($0.1 \leq T/T_c \leq 1$) [23], with constant values of the critical exponent, indicating no change in the dimensionality of the vortex lattice. However, the melting line ($0.2 \leq T/T_c \leq 1$) of the highly anisotropic superconductor $\text{Bi}_2\text{Sr}_2\text{CaCu}_2\text{O}_8$, along which a well known 3D to 2D transition occurs at $H \approx 1$ kOe [24], exhibits a change in the critical exponent from that of a 3D-XY like (~ 3) to a 2D-XY like ($\sim 6-8$) value at this field. The melting line expression arrived at below is also demonstrated to describe the vortex glass melting lines of the non-cuprate compounds MgB_2 and $\alpha\text{-Mo}_x\text{Si}_{1-x}$.

The terms vortex lattice and vortex glass are used here interchangeably, mainly due to the different terminology used in [18, 21] and [5]; however, it is also well known that in systems with sufficient random disorder, the first order vortex

lattice melting transition is replaced by a second order vortex glass melting transition [5], similar to what occurs when the elasticity of the vortex lattice becomes relevant [21, 25]. It should be noted though that the expression for the melting line derived below is neither limited to a weak pinning regime, nor to the anisotropic high- T_c cuprate materials.

III.B Experimental Details

Epitaxial thin film $Y_{1-x}Pr_xBa_2Cu_3O_{6.97}$ samples ($x = 0 - 0.4$) grown on $LaAlO_3$ substrates by pulsed laser ablation, as well as an ultra high purity oxygen deficient $YBa_2Cu_3O_{6.5}$ single crystal grown in a $BaZrO_3$ crucible, were investigated in magnetic fields up to 45 tesla. The $H_g(T)$ line was established from electrical transport measurements with $H \parallel c$. For magnetic fields $H \leq 9$ T resistivity, $\rho(H, T)$, data were taken in lab with fixed field H , and temperature in steps. High field $\rho(H, T)$ data were taken at the National High Magnetic Field Laboratory (Tallahassee, Fl) in a 30 tesla resistive magnet, and the 45 tesla hybrid magnet. In these systems the temperature was held fixed and the field was swept at 3 tesla/min, while continuously measuring $\rho(H)$. The value of T_g (H_g) was determined from the temperature (field) at which the resistance disappears in accordance with the Fisher-Fisher-Huse (FFH) vortex glass scaling expression of the resistivity as the melting transition is approached by decreasing T at constant H [5], $\rho \sim (T - T_g)^{\nu(z+2-d)}$ (or decreasing H at constant T , $\rho \sim (H - H_g)^{\nu(z+2-d)}$ [26]), where ν and z , are the correlation length- and dynamical exponents and d is the dimensionality of the vortex lattice. The value of T_g (H_g) is the temperature (field) at which the linear relation between $[d\log(\rho)/d(T, H)]^{-1}$ and (T, H) that results from the FFH expression vanishes. The films were etched lithographically to form resistance bridges with six terminals with sample dimensions $\ell \times w \times t = 0.50 \text{ cm} \times 0.010 \text{ cm} \times (1.2 - 2) \times 10^{-5} \text{ cm}$. The $YBa_2Cu_3O_{6.5}$ single crystal dimensions are $0.21 \text{ cm} \times 0.076 \text{ cm} \times 7.6 \times 10^{-4} \text{ cm}$. The current values

used were $I = 10 \mu\text{A}$ and 10 mA respectively, corresponding to a current densities of $J \lesssim 90 \text{ A/cm}^2$ and $J \approx 2 \text{ A/cm}^2$. The current density and electric field values used here were well below the criteria of $J_d \sim 10^5 \text{ A/cm}^2$ and $E \sim 10^{-1} \text{ V/cm}$ for films and $J_d \sim 10^2 \text{ A/cm}^2$ and $E \sim 10^{-6} \text{ V/cm}$ established by Charalambous *et al.* [27].

III.C The quantum- thermal-fluctuation model of Blatter and Ivlev

In their seminal work, Blatter and Ivlev [18, 21] included the contribution of quantum fluctuations to the statistical mechanics of the vortex ensemble of a type II superconductor. The scope of the classical formalism based upon the continuum elastic theory for the vortex lattice was extended to a dynamic formalism. Combining this new theoretical framework with the Lindemann criterion, they establish a universal form of the melting line, $H_m(T)$ ($\equiv H_g(T)$).

We begin by briefly restating the vortex lattice melting problem as approached by Blatter and Ivlev [18, 21]. In order to account for the contribution of quantum fluctuations to the mean squared displacement, $\langle u^2 \rangle$, of the single vortex line beyond the standard path integral formulation, a dynamical description is needed. The relevant functional is the Euclidean action $\mathcal{S}[\mathbf{u}]$, in Matsubara representation,

$$\frac{\mathcal{S}[\mathbf{u}]}{\hbar} = \frac{1}{T} \sum_n \{ \mathcal{T}[\mathbf{u}_n] + \mathcal{F}[\mathbf{u}_n] \}, \quad (\text{III.2})$$

with the dynamical term $\mathcal{T}[\mathbf{u}_n]$ given by

$$\mathcal{T}[\mathbf{u}_n] = \frac{1}{2} \int \frac{d^3k}{(2\pi)^3} \{ [\mu(\omega_n) \omega_n^2 + \eta(\omega_n) |\omega_n|] |\mathbf{u}_n(\mathbf{k})|^2 \}.$$

and the elastic free energy of the system, $\mathcal{F}[\mathbf{u}]$, is given by

$$\begin{aligned} \mathcal{F}[\mathbf{u}] = & \frac{1}{2} \int \frac{d^3k}{(2\pi)^3} \{ c_{11}(\mathbf{k}) [\mathbf{K} \cdot \mathbf{u}]^2 + c_{66}(\mathbf{k}) [\mathbf{K}_\perp \cdot \mathbf{u}]^2 \\ & + c_{44}(\mathbf{k}) [k_z \mathbf{u}]^2 \}, \end{aligned}$$

with c_{66} denoting the shear moduli and $c_{11}(\mathbf{k})$ and $c_{44}(\mathbf{k})$ the dispersive compression and tilt moduli, $\mathbf{u}(\mathbf{k})$ is the Fourier transform of the classical displacement field $\mathbf{u}(\mathbf{r})$, and $[\mathbf{k} = (\mathbf{K}, k_z), \mathbf{K}_\perp = (k_y, -k_x)]$.

The summation over Matsubara frequencies will be cut off by either the kinetic mass term $\mu(\omega_n)\omega_n^2$ or the intrinsic cutoff arising from the gap energy, Δ , where Ω is given by $\Omega = \min[\Omega_\mu, \Omega_\Delta]$. The kinetic cutoff frequency is given by $\Omega_\mu \approx \hbar\sqrt{\eta_\ell/\mu_\ell\tau_r}$ where τ_r is the relaxation time associated with vortex line displacements, and η_ℓ and μ_ℓ are the vortex viscosity and vortex mass per unit length, respectively. The gap limited cutoff frequency is $\Omega_\Delta \approx \frac{2}{\hbar}\Delta$.

Various contributions to the vortex mass, μ_ℓ , are well known. These include the mass due to the kinetic energy of the core, μ_ℓ^{core} , and that arising from the static electromagnetic energy of the vortex, μ_ℓ^{em} first calculated by Suhl [28]. Additional contributions to the dynamic vortex mass have been shown to arise from the inertia of quantum excitations of the quasiparticles within the vortex core having longitudinal and transverse components with respect to the vortex velocity, $\mu_\ell^{||e,h}$ and $\mu_\ell^{\perp e,h}$ [29], and from a strain field arising from the torsional shear deformations of the crystal lattice induced by the moving vortex, μ_ℓ^{sf} [30, 31, 32]. The mass contribution which will dominate at high frequencies is the electromagnetic mass, μ_ℓ^{em} [21]. Blatter and Ivlev find $\Omega_\mu \sim 10 \Omega_\Delta$ using the assumption that the value of τ_r is determined by the scattering rate of the quasiparticles in the normal vortex core. However, we consider instead that there are two separate intrinsic relaxation times for the quasiparticles within the vortex core [33, 34], τ_r^{core} , and for the vortex line displacements, τ_r^v , with $\tau_r^v \gg \tau_r^{core}$ as the melting transition is approached [35], leading to the condition $\Omega_\mu < \Omega_\Delta$.

It should be noted that two slightly different expressions are derived in [18] and [21]. In their initial work [18], when calculating the mean squared displacement amplitude, $\langle u^2 \rangle$, the term involving compressional modes is dropped. In the latter work [21], this term is retained.

For the first case, Blatter and Ivlev obtain

$$H_m(t) = \frac{4H_{c2}(0)\theta^2}{(1 + \sqrt{1 + 4Q\theta})^2} \quad (\text{III.3})$$

where θ is a reduced temperature given by $\theta = (\pi c_L^2 / \sqrt{G_i})(1 - t)$, the parameter $Q = [\tilde{Q}_u / (\pi^2 \sqrt{G_i})] \Omega \tau_r$ measures the relative strength of quantum to thermal fluctuations, $t \equiv T/T_c$, $\tilde{Q}_u = \frac{e^2 \rho_N}{\hbar d}$ is the dimensionless quantum of resistance, c_L is the Lindemann number, $G_i = [T_c / H_c^2(0) \epsilon \xi^3(0)]^2 / 2$ is the Ginzburg number, Ω is a cutoff frequency, τ_r is the scattering relaxation time of the quasiparticles in the vortex core given by the Drude formula $\rho_N^{-1} = \sigma_N = e^2 n \tau_r / m$ (σ_N is the normal state conductivity, n is the free charge-carrier density, and m the electron mass), and here, d is the distance between the superconducting planes, and Ω is the cutoff Matsubara frequency for Eq. (III.2).

For the latter case, they find,

$$H_m = \frac{4H_{c2}(0)\theta^2}{(1 + \sqrt{1 + 4S\theta/t})^2} \quad (\text{III.4})$$

where Q is replaced by S/t , and now $\theta = c_L^2 \sqrt{\frac{\beta_{th}}{G_i}} \frac{T_c}{T} (1 - t)$, $S = q + c_L^2 \sqrt{\frac{\beta_{th}}{G_i}}$, $q = \frac{2\sqrt{\beta_{th}}}{\pi^3} \frac{Q_u}{\sqrt{G_i}} \Omega \tau_r$, and $\beta_{th} \approx 5.6$.

Either expression above can be approximated by the power-law form $H_m \sim (1 - t)^\alpha$ over temperatures T ranging from T_c down to $0.6 T_c$. By estimating values for \tilde{Q}_u and $\sqrt{G_i}$ and leaving c_L and $\Omega \tau_r$ as fitting parameters in [18], they find $\alpha \approx 1.45$, in close agreement with experimental values. As pointed out by Blatter and Ivlev, the value of the approximate exponent α depends on the quantum parameter Q and the reduced temperature θ . This readily explains the experimentally observed increase of α as the temperature drops below $T \sim 0.6 T_c$, which has previously been considered as evidence for a dimensional crossover of vortex fluctuations from 3D to 2D [36].

III.D Modification of the Blatter and Ivlev model

Instead of using approximate constant values for the factors that go into the quantum parameters Q or q , the appropriate exact temperature and field dependences are included. Since it is not known *a priori* whether the appropriate cutoff frequency is Ω_μ or Ω_Δ for all type-II superconductors, both are considered here. The differing expressions found below provide a means of experimentally determining the relevant cutoff mechanism by comparing to independent scaling results, as explained in the next section. The analytical procedure in this section is valid for either of the original expressions of Blatter and Ivlev. Results for both expressions are given below for comparison in Figs. III.1 and III.2 and Tables III.1 and III.2.

Starting with the expression for the kinetic cutoff frequency, using the Bardeen-Stephen expression for the viscous drag coefficient [37],

$$\eta_\ell \approx \frac{\Phi_0^2 \sigma_N}{2\pi \xi^2}, \quad (\text{III.5})$$

using the electromagnetic contribution of the vortex mass [28],

$$\mu_\ell^{em} = \frac{1}{4\mu_0} \frac{\xi^2 H_c^2}{c^2} \left(\frac{\lambda}{\lambda_d} \right)^2 \quad (\text{III.6})$$

with $H_c = \frac{\Phi_0}{2\sqrt{2}\pi\lambda\xi}$, and including the temperature dependence of $\xi = \xi_0/(1-t)^{\frac{1}{2}}$, we then have

$$\Omega_\mu \approx \sqrt{\frac{\eta_\ell}{\mu_\ell^{em} \tau_r^v}} = \frac{4c\lambda_d}{\xi_0} \sqrt{\frac{\pi\mu_0\sigma_N}{\tau_r^v}} (1-t)^{\frac{1}{2}}, \quad (\text{III.7})$$

where λ_d is a shielding length, which is a few times that of $(k_F)^{-1}$.

If instead the frequency cutoff in Eq. (III.2) is due to the gap limitation, then we will have

$$\Omega_\Delta \approx \frac{2\Delta_0}{\hbar} (1-t)^{\frac{1}{2}} \quad (\text{III.8})$$

Blatter and Ivlev heuristically argue that the relaxation time, τ_r , of the vortices is determined by the normal state conductivity based upon the condition that the vortex velocity has to be consistent with the quasiparticle motion inside

the vortex core, thus $\tau_r = \frac{m}{ne^2}\sigma$ [21]. We however consider that, since the vortex motion under consideration is due to quantum or thermal fluctuations, the properties of the fluctuation conductivity will determine the vortex motion. In an isotropic system the zero field ac fluctuation conductivity in the critical region scales as [5, 22],

$$\sigma_f(\omega) \sim \xi^{z+2-d} \mathcal{S}(\omega \xi^z),$$

as $T \rightarrow T_c$ where $\xi \sim |T_c - T|^{-\nu}$. Then with $\tau_r^v \sim \sigma_f$, in the limit $\omega \rightarrow 0$, and the expression for the zero field fluctuation conductivity to be evaluated along the melting line ($T = T_g$), we arrive at

$$\tau_r^v \sim \xi^{z+2-d} \sim \left(\frac{T}{T_c}\right)^s \left(1 - \frac{T}{T_c}\right)^{-s}, \quad (\text{III.9})$$

in agreement with Eq. (III.1), where now the exponent is identified as $s \equiv \nu(z + 2 - d)$.

The ansatz of the vortex glass theory of Fisher, Fisher, and Huse [5] is that the zero field critical point is actually a multicritical point so that the vortex glass melting line is actually a line of critical points. The generalization of the zero field transition to the in-field transition leads to the scaling expression for the vanishing of the dc resistivity as $T \rightarrow T_g^+$,

$$\rho(T) = 1/\sigma(T) \sim 1/\xi_{VG}^{z+2-d} \sim (T - T_g)^{\nu(z+2-d)}$$

Thus, it can be seen that the critical exponent which characterizes the vanishing of the resistivity as the melting transition of the vortex ensemble is approached from temperatures/fields above the transition also characterizes the shape of the melting line in the $H - T$ plane.

If correlated columnar disorder is relevant, then the critical dynamics of the vortex ensemble is described by the Bose glass model where the diverging length scale is the wandering length of a localized vortex line transverse to the field direction, $\ell(T) \sim (T_{BG} - T)^{\nu'}$, and the relaxation time of a fluctuation diverges as $\tau \sim \ell_{\perp}^{z'}$, where ν' and z' are new critical exponents [6]. The vortex dynamics in

the melting region described by this model leads to a power law scaling of the dc resistivity, $\rho(T)$, with the same form as that found by the FFH vortex glass model with the exponent $s \rightarrow s'$, where s' is defined in accordance with the updated Bose glass scaling relations for the resistivity [8],

$$\begin{aligned}\rho_{\perp} &= \ell^{d+\zeta-3-z} \tilde{\rho}_{\pm}^{\perp}(H_{\perp} \ell^{d-2}) \\ \rho_{\parallel} &= \ell^{d-\zeta-1-z} \tilde{\rho}_{\pm}^{\parallel}(H_{\perp} \ell^{d-2}),\end{aligned}$$

where ζ is an anisotropy exponent, with $\zeta = 1$ for unscreened long-range interactions and $\zeta = 2$ for correlated disorder. In the case when H is parallel to the columnar defects, the relevant resistivity is ρ_{\perp} , so then $s' \equiv \nu'(z' + 3 - \zeta - d)$, with $\zeta = 2$.

Whether the correct form for the critical exponent is the vortex glass exponent, s , or the Bose glass, s' , can readily be determined by the angular dependence of the scaling of the resistivity at the melting transition, where, if the vortex ensemble is a Bose glass [38],

$$\begin{aligned}\rho_{\perp}(t, \theta) &= |t|^{\nu'_{\perp}(z'-2)} f_{\pm}(\theta/|t|^{\nu'_{\perp}}) \\ \rho_{\parallel}(t, \theta) &= |t|^{\nu'_{\perp} z'} g_{\pm}(\theta/|t|^{\nu'_{\perp}})\end{aligned}$$

and by the well known cusp in the phase boundary $T_{BG}(H_{\perp})$ where the perpendicular field $H_{\perp}^c(T)$ at the Bose glass to vortex liquid transition varies as [8, 38],

$$H_{\perp}^c \sim \pm(T_{BG}(0) - T)^{\nu'}.$$

The Bose glass phase will eventually give way to the vortex glass phase as the field increases past the matching field, (the field at which the number of vortex lines is equal to the number of columnar defects,) so that the majority of the vortex lines are far away from the correlated disorder and their dynamical properties are dominated by point defects. The change in vortex dynamics along the melting transition will be reflected in the shape of the melting line, $H_g(T)$, through a

change of the value of the critical exponent and of the quantum parameter Q or q . For simplicity we use below the vortex glass exponent, s , but it should be understood that $s \rightarrow s'$ in the case of a Bose glass.

Combining Eq. (III.7) with Eq. (III.9), and with all expressions to be evaluated at the melting temperature $T = T_g \equiv T_m$, we obtain the full expression for the kinetic cutoff frequency,

$$\Omega_\mu = \frac{4c\lambda_d}{\xi_0} \sqrt{\frac{\pi\mu_0\sigma_N}{\tau_0}} \left(\frac{T}{T_c}\right)^{-s/2} \left(1 - \frac{T}{T_c}\right)^{(1+s)/2} \quad (\text{III.10})$$

Next we use the expression for the dimensionless quantum of resistance given in ref. [3],

$$\tilde{Q}_u = \frac{e^2}{\hbar} \frac{\rho_N}{\epsilon\xi}, \quad (\text{III.11})$$

and the field dependent expression of the Ginzburg number [10],

$$G_i(H_g) \approx (G_i)^{\frac{1}{3}} \left(\frac{H_g}{H_{c2}(0)}\right)^{\frac{2}{3}}. \quad (\text{III.12})$$

Combining Eqns. (III.8) or (III.10), (III.9), (III.11), and (III.12), and including the temperature dependence of $\xi = \xi_0/(1-t)^{\frac{1}{2}}$ in the kinetic cutoff frequency Ω_μ , and in the expression for the dimensionless quantum of resistance, we arrive at the final expressions for the value of the quantum parameters, $Q_{[\mu,\Delta]}$, and $q_{[\mu,\Delta]}$, at the melting line $H_g(T)$,

$$Q_{[\mu,\Delta]} = \frac{\tilde{Q}_0 \Omega_0 \tau_0}{\pi^2 \sqrt{G_i(H_g)}} t^{\tilde{s}} (1-t)^{1-\tilde{s}} \quad (\text{III.13})$$

$$q_{[\mu,\Delta]} = \frac{2\sqrt{\beta_{th}}}{\pi^3} \frac{\tilde{Q}_0 \Omega_0 \tau_0}{\sqrt{G_i(H_g)}} t^{\tilde{s}} (1-t)^{1-\tilde{s}} \quad (\text{III.14})$$

with

$$\Omega_0[\mu, \Delta] = \left[\Omega_{\mu 0} \equiv \frac{4c\lambda_d}{\xi_0} \sqrt{\frac{\pi\mu_0\sigma_N}{\tau_0}}, \Omega_{\Delta 0} \equiv \frac{2\Delta_0}{\hbar} \right],$$

$\tilde{Q}_0 \equiv \frac{e^2}{\hbar} \frac{\rho_N}{\epsilon\xi_0}$, $\tilde{s}[\mu, \Delta] = [s/2, s]$, and $t \equiv T/T_c = T_g/T_c$.

Combining Eq. (III.3) with Eq. (III.13), we have

$$H_g(Q, t) = \frac{4H_{c2}(0) \frac{(\pi c_L^2)^2}{G_i(H_g)} (1-t)^2}{\left(1 + \sqrt{1 + 4(\tilde{Q}_0 \Omega_0 \tau_0) \frac{c_L^2}{\pi G_i(H_g)} t^{\tilde{s}} (1-t)^{2-\tilde{s}}}\right)^2}, \quad (\text{III.15})$$

Combining Eq. (III.4) with Eq. (III.14), gives

$$H_g(q, t) = \frac{4H_{c2}(0) \frac{\beta_{th} c_L^4}{G_i(H_g)} (t^{-1} - 1)^2}{\left(1 + \sqrt{1 + 4\left(\frac{2\tilde{Q}_0 \Omega_0 \tau_0}{pi^3} t^{\tilde{s}} (1-t)^{1-\tilde{s}} + c_L^2\right) \frac{c_L^2 \beta_{th}}{G_i(H_g)} t^{-1} (t^{-1} - 1)}\right)^2}. \quad (\text{III.16})$$

It should be noted that the expression used for the field dependent Ginzburg number in Eq. (III.12) is arrived at from a melting line that follows the power-law form $H_m \sim \frac{H_{c2}(0)}{\sqrt{G_i}} (1-t)^{\frac{3}{2}}$, and so is strictly valid only for $T \gtrsim 0.6 T_c$. In general, for a portion of the melting line that can be approximated by $H_m \sim \frac{H_{c2}(0)}{\sqrt{G_i}} (1-t)^\alpha$, the field dependent Ginzburg number will be given by,

$$G_i(H_g) \approx (G_i)^{\frac{1}{2\alpha}} \left(\frac{H_g}{H_{c2}(0)}\right)^{\frac{1}{\alpha}}. \quad (\text{III.17})$$

When performing a fit of Eq. (III.16) to melting line data, a temperature dependent expression for the Ginzburg number, $G_i(T_g)$, is needed. This is obtained from the field dependent Ginzburg number by evaluating Eq. (III.17) at each known field, $H_g(T)$, and inverting as a function of temperature.

Also, it should be recognized that at finite frequencies dispersive effects lead to, [21, 39]

$$\eta(\omega) \approx \Phi_0 \rho_s \frac{\omega_0 \tau_r^{core} (1 - i\omega \tau_r^{core})}{(1 - i\omega \tau_r^{core})^2 + (\omega_0 \tau_r^{core})^2}, \quad (\text{III.18})$$

with $\rho_s = 2e|\psi|^2$ the superfluid density. Note that for large frequencies ($\omega \tau_r \gg 1$) and with $\rho_s \sim (1-t)$, this leads to the same temperature dependence of Ω found in Eq. (III.7). Alternately, [21, 40] starting from Eq. (III.18) with the condition $\omega \tau_r \gg 1$, $\omega_0 \tau_r \ll 1$, and using $\rho_s = -en$, $\omega_o = \omega_c = eB/m$, with $B \approx H_{c2}$,

$$\eta_\ell(\omega) \approx \frac{\Phi_0^2}{2\pi\xi^2} \frac{e^2 n \tau_r^{core}}{m} \quad (\text{III.19})$$

which is identical to the Bardeen-Stephen result, Eq. (III.5).

An important result, addressed in more detail in Appendices A and B, is that in the large Q or q limit, the modified form of both expressions, Eq. (III.15) and Eq. (III.16) reduce to the form of the expression found empirically by Lundqvist *et al.* [41], $H_g = H_0[(1 - T/T_c)/(T/T_c)]^\alpha$, with $\alpha = \tilde{s}$. This expression was found to fit smoothly to the entire range of data examined there ($H \leq 12 T$), but, as seen in Fig. III.3, fails to fit the larger range of data shown here. The modified vortex glass model of Rydh, Rapp, and Andersson [42, 43], which is based upon the vortex glass melting line equation of Lundqvist *et al.*, as well as the Coulomb-gas scaling model [44], are shown to be special cases of the model considered here.

III.E Discussion

The melting line data, $H_g(T)$, of the $Y_{1-x}Pr_xBa_2Cu_3O_{6.97}$ films and $YBa_2Cu_3O_{6.5}$ single crystal obtained in this study, as well as that of a film of $Sm_{1.85}Ce_{0.15}CuO_{4-y}$ [23], a $Bi_2Sr_2CaCu_2O_8$ single crystal [24], a bulk MgB_2 sample [45], and an amorphous $\alpha-Mo_xSi_{1-x}$ film [46, 47], were fitted by Eqs. (III.15) and (III.16). We discuss in detail below the results for the fits to the data for the $Y_{1-x}Pr_xBa_2Cu_3O_{6.97}$ films and $YBa_2Cu_3O_{6.5}$ single crystals, shown in Figs. III.1 and III.2. Values of the parameters obtained from the fits corresponding to Figs. III.1 and III.2 are given in Tables III.1 and III.2 respectively. Results for the remaining samples are commented on in sections III.E.2 and III.E.3.

III.E.1 $Y_{1-x}Pr_xBa_2Cu_3O_{6.97}$ and $YBa_2Cu_3O_{6.5}$

The quantum parameters Q and q

Equations (III.15) and (III.16) can be seen to provide equally good descriptions of the experimental data for all the samples. With the experimental value $Q_0 = 0.34 \pm 0.15$ obtained from Eq. (III.15), we solve for the value of $\Omega_0\tau_{r0}^v$

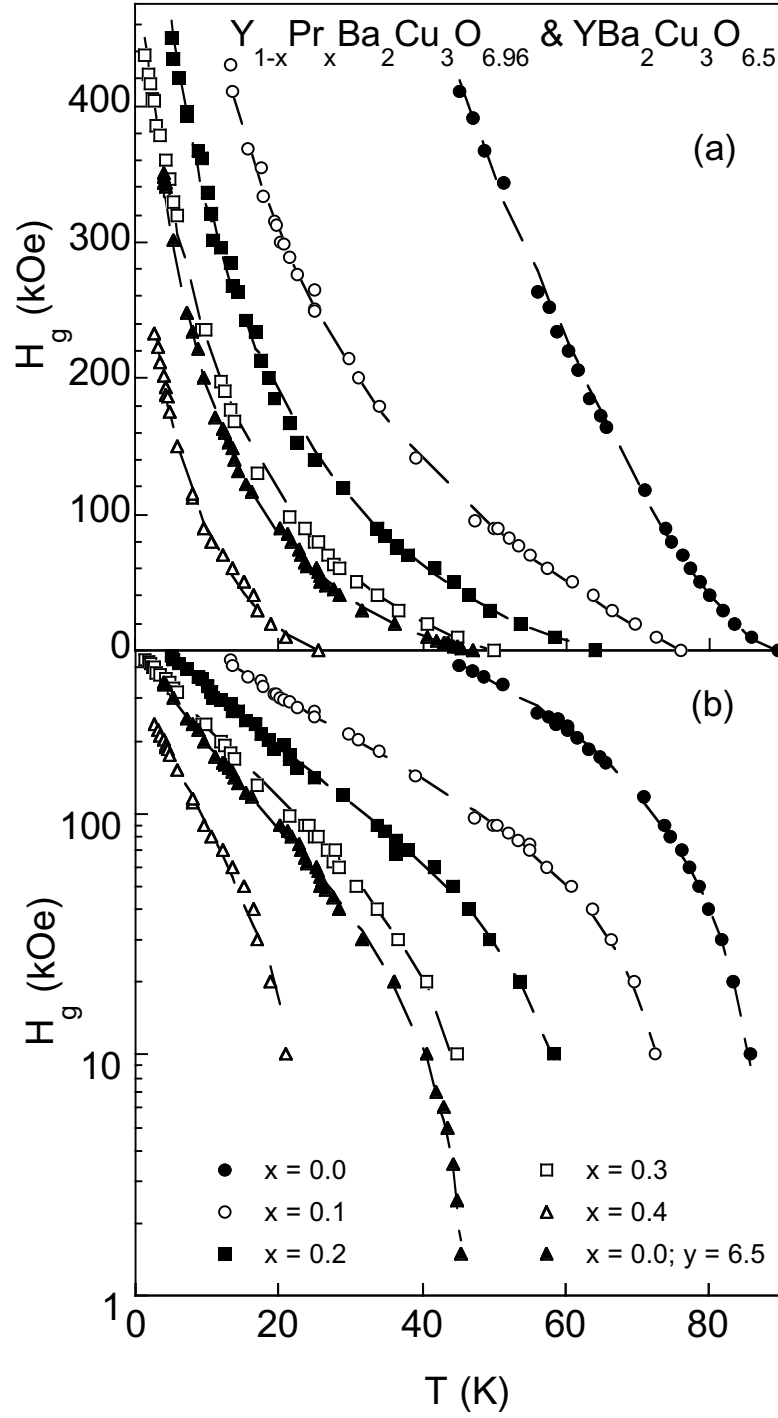


Figure III.1: Vortex glass melting line $H_g(T)$ vs T data for $Y_{1-x}Pr_xBa_2Cu_3O_{6.97}$ films ($1\text{kOe} < H < 450\text{ kOe}$) and a $YBa_2Cu_3O_{6.5}$ single crystal ($100\text{ Oe} < H < 450\text{ kOe}$) with fits of the modified melting line equation (III.15) shown in linear (a) and semi-log (b) plots to emphasize the quality of the fits over the entire $H - T$ range.

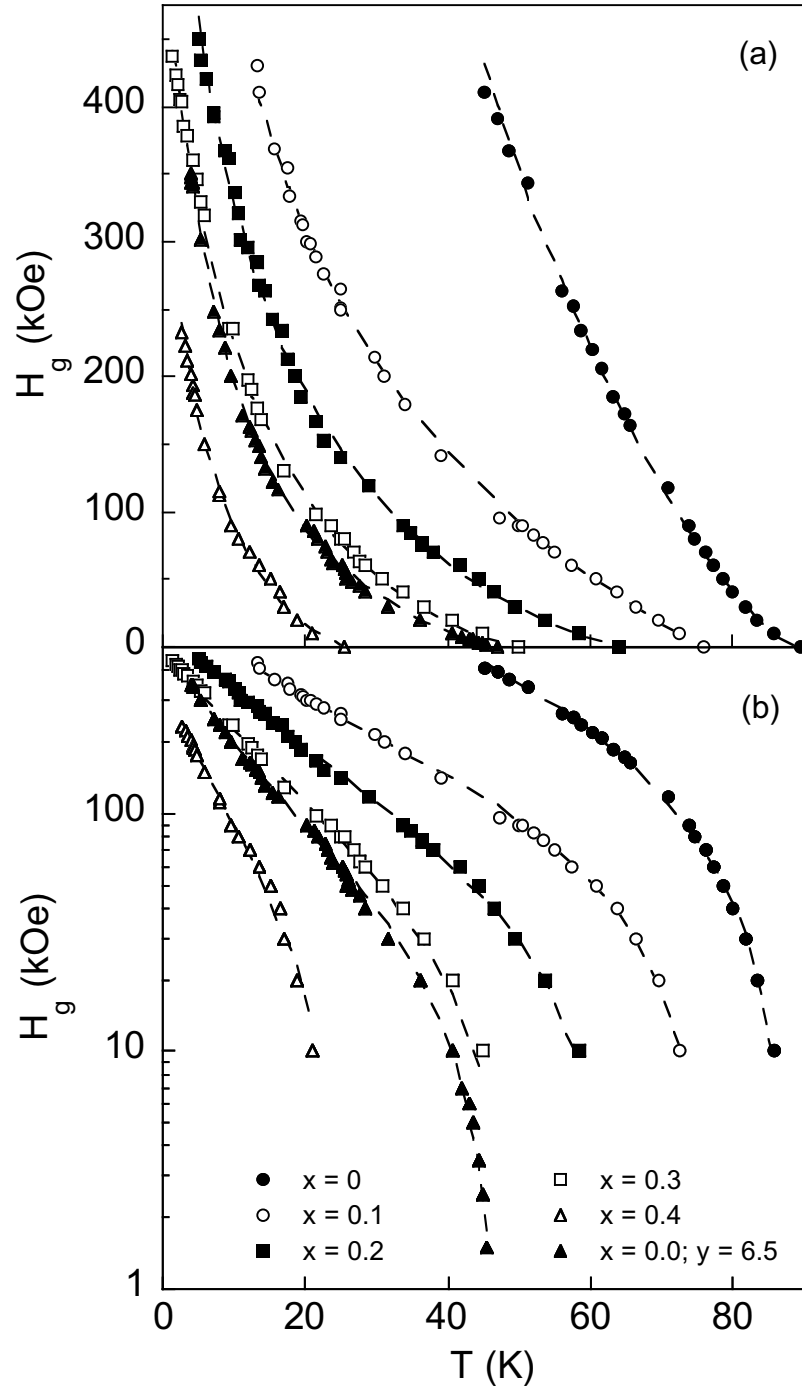


Figure III.2: (a) Fit of Eq. (III.16) to vortex glass melting line, $H_g(T)$, data of $Y_{1-x}Pr_xBa_2Cu_3O_{6.97}$ ($x = 0 - 0.4$) and $YBa_2Cu_3O_{6.5}$. (b) Same data as in (a) shown in a semi-log plot to emphasize the quality of the fit to the low field region.

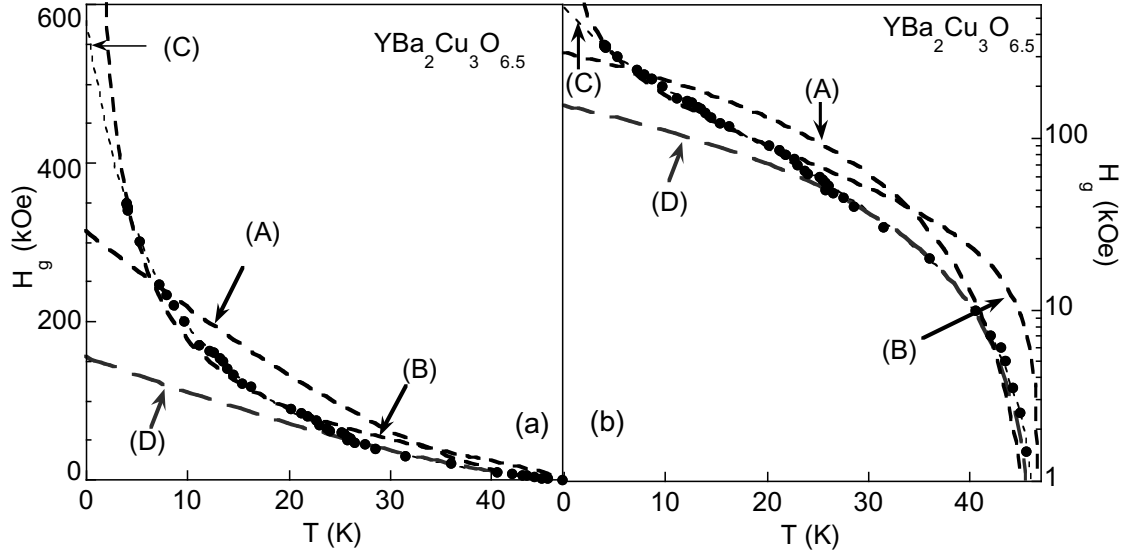


Figure III.3: Comparison of the quality of the fits to the *entire* vortex melting line data of the $\text{YBa}_2\text{Cu}_3\text{O}_{6.5}$ single crystal by the expressions of Blatter and Ivlev [18] (A), Lundqvist et al. [41] (B), and that obtained here (C) (Eq. (III.15)) shown in linear (a) and semi-log (b) plots, demonstrating that only Eq. (III.15) adequately describes the data over the entire $H - T$ range. Also shown is the empirically observed expression $H_m \sim (1 - t)^\alpha$, for $T \gtrsim 0.6 T_c$ [36] (D).

for the $\text{YBa}_2\text{Cu}_3\text{O}_{7-\delta}$ film. Using $\xi_0 = 13 \text{ \AA}$, $\epsilon = 1/8$ [10], $\rho_N \approx 0.2 \mu\Omega m$; we obtain $\Omega_0 \tau_{r0}^v \approx 1.1$. If we use the second modified melting line equation, Eq. (III.16), then we get an equally good fit, indistinguishable from Eq. (III.15) with similar values of \tilde{s} and c_L , with $q_0 \sim 1/2 - 1/10 \times Q_0$ (Table I.2). The result, $q < Q$, can be understood by recalling that Q (and q) is a measure of the ratio of the quantum to thermal contributions to vortex line displacements. The inclusion of the additional thermal contribution of the compressional modes in the modified form of the second melting line equation of Blatter and Ivlev [21], leads to a relative increase of the contribution of thermal displacements over that of quantum displacements, so naturally, $q < Q$. The non-monotonic variation of Q_0 with respect to Pr doping and reduced oxygen content (see Table III.1) results from the dependence upon many physical properties of these systems, including the magnetic field penetration depth λ , the superconducting coherence length ξ , the critical temperature T_c , anisotropy of the system, and the strength and type of disorder. The value of the quantum of resistance $\tilde{Q}_u(0)$ of each system is given in Table III.1, and is seen to exhibit a similar trend, particularly with respect to the values for the $\text{YBa}_2\text{Cu}_3\text{O}_{7-\delta}$ and $\text{YBa}_2\text{Cu}_3\text{O}_{6.5}$ samples. The values of s found here are notably different for the clean $\text{YBa}_2\text{Cu}_3\text{O}_{7-\delta}$ and the disordered $\text{Y}_{1-x}\text{Pr}_x\text{Ba}_2\text{Cu}_3\text{O}_{6.97}$ and $\text{YBa}_2\text{Cu}_3\text{O}_{6.5}$ systems, and are presumably due the dynamical response of the vortices being dependent upon more than just the extent of disorder.

Enhancement of the vortex line mass

Using the values of $\epsilon = 1/\gamma$, ρ_N , and q_0 in Table III.2, with $\lambda_d \approx k_F^{-1}$ ($k_F \sim 0.2 \text{ \AA}^{-1}$ [21]) and $G_i(0) \approx 10^{-2}$ we can then calculate values for Ω_0 and τ_0 using Eq. (III.14) and Eq. (III.10). We find $\Omega_\mu \sim 10^3 \Omega_\Delta$ for $x = 0.1-0.4$ and $y = 6.5$, and $\Omega_\mu \sim 10^4 \Omega_\Delta$ for $x = 0$. This would imply that the correct expression for the quantum parameter is q_Δ , and thus $\tilde{s} = s$. However, as shown by the example in Fig. III.4 for $\text{YBa}_2\text{Cu}_3\text{O}_{6.5}$, the critical exponent, $s \equiv \nu(z-1)$,

obtained from scaling of the resistivity data, $\rho(T)$, agrees well with the value of \tilde{s} found from the fit to the melting line data by using Ω_μ (Eq. (III.10)) in Eq. (III.16) for all of the melting lines, *i. e.* $\tilde{s} = s/2$. This leads to an apparent contradiction, since the condition $\Omega = \min[\Omega_\mu, \Omega_\Delta]$ means we expect Ω to be given by Eq. (III.8).

This contradiction can be resolved if the effective vortex line mass is larger than the individual line mass, μ_ℓ^{em} used in Eqs. (III.7) and (III.10). From Eq. (III.14) we can solve for τ_0 in terms of the experimentally determined fit parameters, giving,

$$\tau_0 = \left(\frac{q_0}{\tilde{Q}_0} \right)^2 \frac{\pi^6}{4\beta_{th}} \frac{\mu_\ell^{em}}{\eta_\ell}. \quad (\text{III.20})$$

Then, substituting Eq. (III.20) into Eq. (III.7) and assuming an effective mass $\mu_\ell^{em*} = \alpha \mu_\ell^{em}$, we solve for the enhancement factor necessary to satisfy $\Omega_\mu = \Omega_\Delta$,

$$\alpha = \frac{\eta_\ell}{\mu_\ell^{em}} \frac{\tilde{Q}_0}{q_0} \frac{2\sqrt{\beta_{th}}}{\pi^3} \frac{1}{\Omega_\Delta}. \quad (\text{III.21})$$

This gives $\alpha \sim 10^4$ for the $\text{YBa}_2\text{Cu}_3\text{O}_{7-\delta}$ film and $\alpha \sim 10^3$ for the remaining samples.

The friction encountered by a vortex line mass due to dissipation and quantum vortex tunneling has been considered by Blatter *et al.* [48]. The dynamic vortex friction produces an enhanced and dispersive vortex effective mass, $\mu_\ell^* = \mu_\ell(1 + \eta_\ell/|\omega|\mu_\ell)$, where ω is an inverse quantum tunneling time, η_ℓ is the total viscosity per unit length, and μ_ℓ is the total vortex mass per unit length. In the dissipative limit, the quantum tunneling time is found to be [48],

$$t = \frac{\eta_\ell L_c^2}{\epsilon_o \mu_\ell},$$

where $\epsilon_o = [\Phi_0/4\pi\lambda]^2$, is the basic energy scale of the vortex line energy, $\epsilon_\ell = \epsilon_o \ln(\lambda/\xi)$, and L_c is the collective pinning length. Since all contributions to the vortex mass are expected to be enhanced by the same factor, and $\mu_\ell \gtrsim \mu_{core}$, the effective electromagnetic vortex mass is,

$$\mu_{em}^* \approx \mu_{em} \left(1 + \frac{\eta_\ell^2 L_c^2}{\epsilon_o \mu_{core}} \right). \quad (\text{III.22})$$

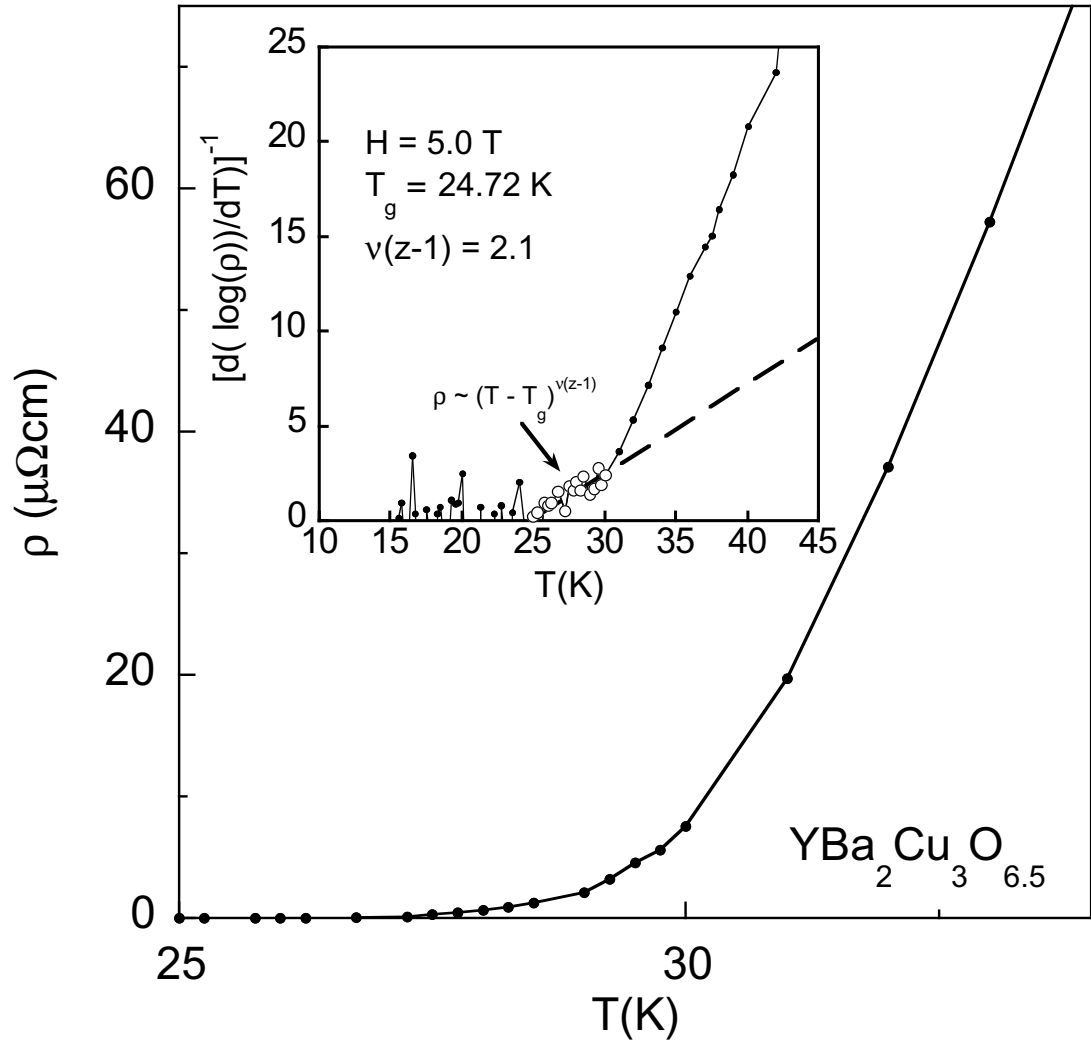


Figure III.4: Resistivity data, $\rho(T)$, and scaled resistivity data, $[\text{d} \log \rho(T)/\text{d}T]^{-1}$ vs T , of a $\text{YBa}_2\text{Cu}_3\text{O}_{6.5}$ single crystal.

A lower limit of the value of the collective pinning length, L_c , can be set by the vortex lattice constant, $a_\Delta \approx (\Phi_0/B)^{1/2}$. For $B \sim 100$ T, $a_\Delta \approx 45$ Å. With a carrier density $n \approx 2.5 \times 10^{21} \text{ cm}^{-3}$, this gives $\mu_{core} = (2/\pi^3)mk_F \approx 2.5 \times 10^{-22}$ kg/m. Using $\lambda \approx 1400 - 2900$ Å [49], then $\epsilon_o \approx (0.3 - 1) \times 10^{-12}$ J/m. Using the values of ρ_N and ξ given in Table III.2, $\eta_\ell(0) \approx 2 \times (10^{-6} - 10^{-5})$ Ns/m². Finally then, the lower limit of the effective electromagnetic vortex mass is found to be, $\mu_{em}^* \sim (10^5 - 10^6)\mu_{em}$, a considerable increase. Substituting the effective mass value back into Eq. (III.14), and solving again for Ω_0 and τ_0 for each sample, we find $\Omega_{\mu^*} \sim (10^{-1} - 10^{-2})\Omega_\mu$. It is seen then, that dissipation from quantum tunneling produces an enhancement of the vortex mass sufficient to result in $\Omega_{\mu^*} < \Omega_\Delta$, removing the apparent contradiction of the exponent values described above.

Evolution of quantum fluctuations along the vortex glass melting line

The values of the quantum parameter as a function of temperature, $q(t)$, for each of the samples are shown in Fig. III.5. The results here are in contrast to what might be expected, in that the value of $q(t)$ increases with temperature, becoming very large as $T \rightarrow T_c$. This can be understood physically from the contribution of various intrinsic properties: First, the line tension $\epsilon_\ell \propto \lambda^{-2}$ vanishes as $(1 - t)$. So, while the effect of quantum fluctuations are significant at low temperatures, the quantum tunneling of a segment of the vortex flux line, in this case a pancake vortex, becomes easier as the flux line becomes more flexible with increasing temperature. Additionally we would expect quantum tunneling to be easier at lower fields (higher temperatures) with the increased distance between the flux lines. Secondly, with the dynamic behavior of the vortices along the melting line set by the relaxation time, τ_r^v , which follows from the scaling properties of the fluctuation conductivity, the superfluid density plays a significant role in the problem of the melting transition.

Experimental evidence, at least in the case of $\text{YBa}_2\text{Cu}_3\text{O}_{6.95}$, indicates that the field dependence penetration depth, λ_{ab} , in magnetic fields up to 6 tesla,

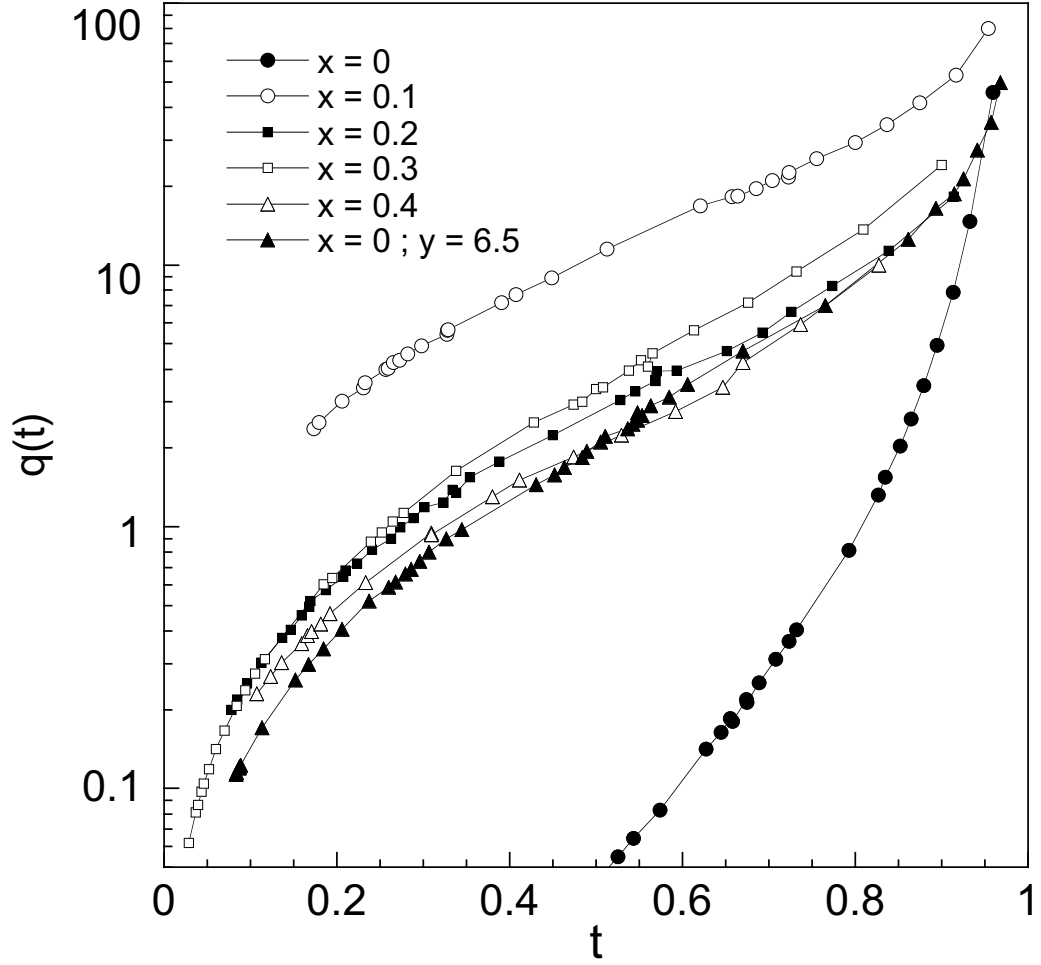


Figure III.5: The quantum parameter, $q(t)$, measuring the relative contribution of quantum to thermal displacements of a single vortex line for the $Y_{1-x}Pr_xBa_2Cu_3O_{6.97}$ and $YBa_2Cu_3O_{6.5}$ samples obtained from the fit of the melting line data to Eq. (III.16).

seem to indicate that $\lambda_{ab}(H = H_{c2}) \approx 2\lambda_{ab}(H = 0)$ at $T = 0$ [50, 51]. Additionally, Amin *et al.* [52], studied the consequences of the nonlinear, nonlocal, and nonanalytic nature of the effect of the anisotropic superconducting gap on the effective penetration depth, and find, that contrary to the common belief, the effective penetration depth is not a linear function of the magnetic field, a result that is in agreement with the experimental data of ref. [50]. From the temperature and field dependence of the penetration depth, λ , it can be seen that the superfluid density in the region of the vortex solid melting line is larger at high fields than at low fields. This adds to the impedance of the tunneling process, since this means moving a core of normal electrons through a more dense superfluid. It is predicted that the melting line will terminate prior to reaching H_{c2} when it gives way to what is referred to as a quantum vortex liquid state (QVL) [3, 18, 21, 53]. Experimental evidence for the QVL state was found in $a\text{-Mo}_x\text{Si}_{1-x}$ amorphous films at fields above $H \approx 0.9 B_{c2}(0)$ [46, 47], so it is quite possible that the melting line terminates well before any strong field suppression effects of the superfluid density are relevant. Lastly, as can be seen in Fig. III.6, and discussed below, the distance over which quantum fluctuations displace the vortex is of the order of the size of the vortex core. At low fields, as the melting line approaches the critical temperature, T_c , the size of the vortex cores at the melting transition increases as $(1 - T/T_c)^{-1/2}$, thus the distance over which a quantum fluctuation displaces a vortex line segment grows.

An important aspect of the physical picture that needs to be kept in mind, is that disorder *promotes* quantum fluctuations, as can be seen by the expressions for $\tilde{Q} \propto \rho_N$ and $\Omega_\mu \propto \sqrt{\rho_N}$, so that $q_{[\mu, \Delta]} \propto [\sqrt{\rho_N}, \rho_N]$. This is understood by the fact that the vortices need somewhere to tunnel to, so then, up to a certain level of disorder the value of q should increase as random disorder increases, and then decrease as the increasing disorder begins to shorten the distance over which a vortex segment tunnels. This effect can be seen in Fig. III.5 where, the clean $\text{YBa}_2\text{Cu}_3\text{O}_{7-\delta}$ film has a much lower value of $q(t)$ than

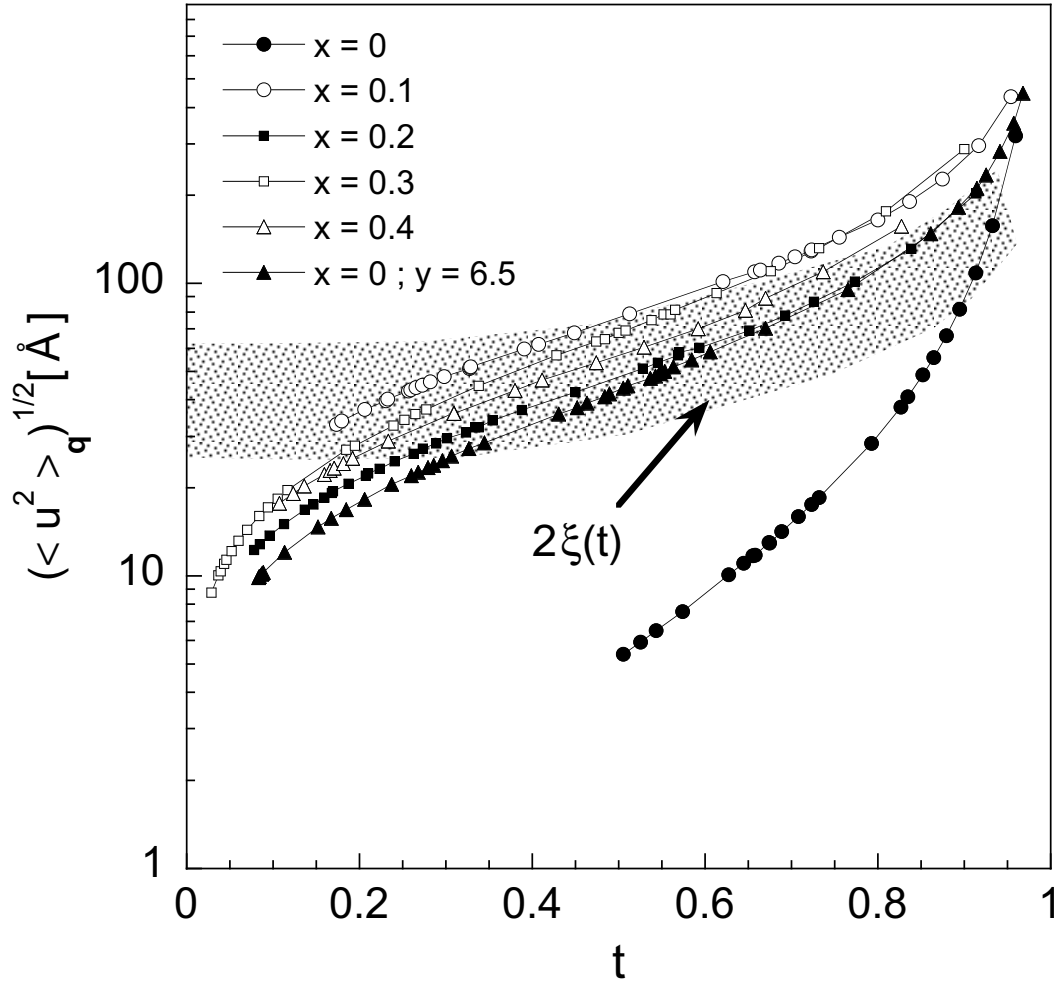


Figure III.6: Temperature dependence of the quantum tunneling length scale defined by the square root of the quantum contribution to the mean squared displacement field $\langle u^2 \rangle_q$ for the $\text{Y}_{1-x}\text{Pr}_x\text{Ba}_2\text{Cu}_3\text{O}_{6.97}$ and $\text{YBa}_2\text{Cu}_3\text{O}_{6.5}$ films. The shaded region corresponds to the range of the diameters of the vortex cores, $d \sim 2\xi$.

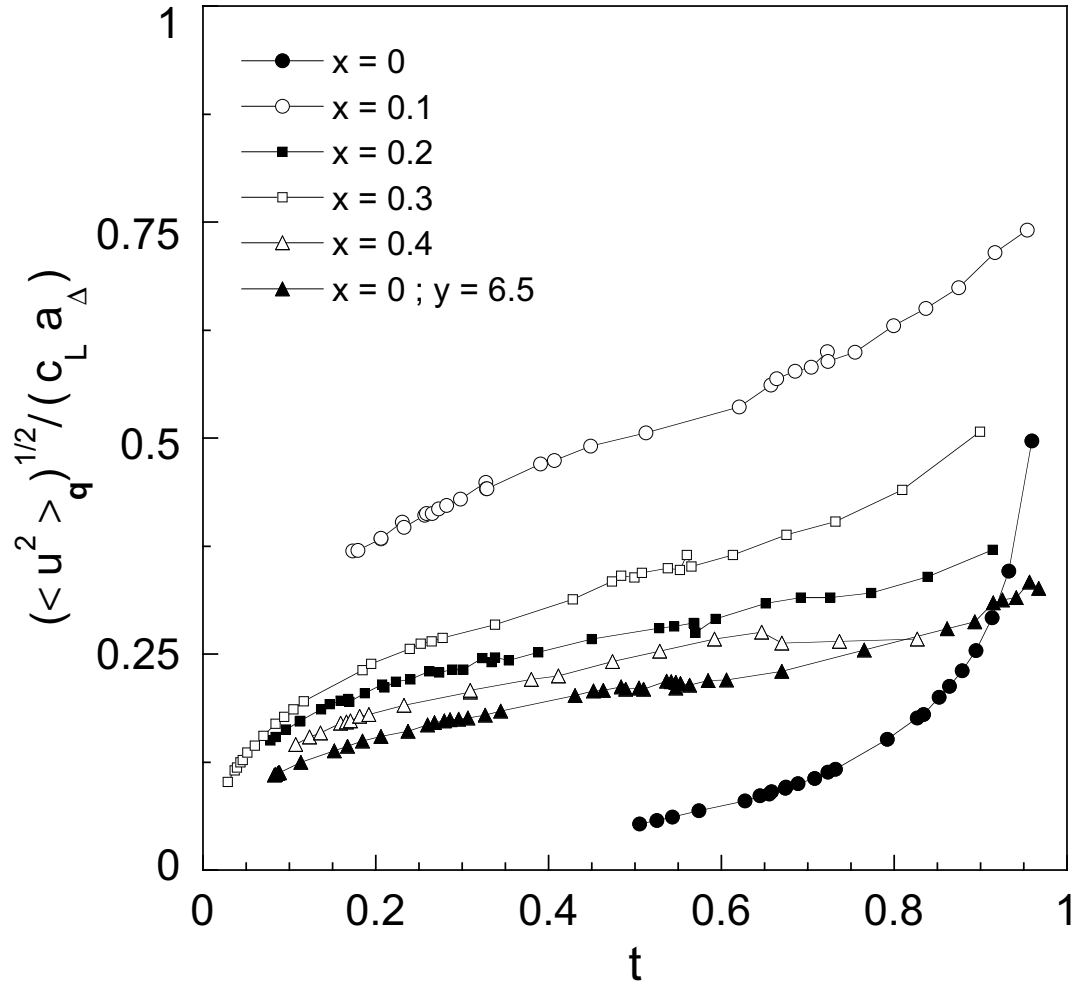


Figure III.7: Fraction of the quantum contribution to the mean squared displacement field to the total displacement, $\sqrt{\langle u^2 \rangle_q / \langle u^2 \rangle_{T_m}}$, at the melting transition, where $\langle u^2 \rangle_{T_m} \approx c_L^2 a_0^2$ is Lindemann criterion for the melting of the vortex lattice. The error of the values shown are estimated as $\sim 10\%$.

the doped $Y_{1-x}Pr_xBa_2Cu_3O_{6.97}$ and oxygen deficient $YBa_2Cu_3O_{6.5}$ samples, and, also from the result where the $x = 0.1$ sample has a notably larger value of $q(t)$ than the other samples. This same behavior can be also be seen in Fig. III.6 where the distance over which quantum fluctuations displace the vortex core is found shown as the square root of the quantum contribution to the mean squared displacement field, $\langle u^2 \rangle_q$ versus the reduced temperature t , where [21],

$$\langle u^2 \rangle_q \approx \frac{4}{\pi^2} Q \Omega \tau_r \xi^2.$$

The quantum tunneling length is shortest in the clean $YBa_2Cu_3O_{7-\delta}$ film, longest in the $x = 0.1$ film, and close to, or less than, the tunneling length of the $x = 0.1$ sample in the remaining films. The apparent non-monotonic dependence of the quantum tunneling length on x for the $x = 0.1 - 0.4$ films is likely attributable to the error of $\sim 15\%$ of the values shown. For comparison, the range of the size of the vortex cores, $d \sim 2\xi$, over all the samples is indicated by the range of the shaded region. With the exception of the $YBa_2Cu_3O_{7-\delta}$ sample, it is observed that, over most of the temperature range, the quantum fluctuations smear the core over a distance that is comparable to the size of the core, a result that is in agreement with the observation of Blatter and Ivlev for $YBa_2Cu_3O_{7-\delta}$ where they used a constant value of q and the zero temperature value of the coherence length ξ_0 [18, 21].

The fraction of the quantum contribution to the displacement of the vortex line to the total displacement necessary for melting of the vortex lattice, $\sqrt{\langle u^2 \rangle_q} / c_L a_0$, where the critical displacement is defined by the Lindemann criterion, $\langle u^2 \rangle \approx c_L^2 a_0^2$, is shown in Fig. III.7. The contribution of quantum fluctuations to the melting of the vortex lattice is found to be a significant to dominant part of the melting process.

III.E.2 The vortex glass melting lines of $\text{Sm}_{1.85}\text{Ce}_{0.15}\text{CuO}_{4-y}$ and $\text{Bi}_2\text{Sr}_2\text{CaCu}_2\text{O}_8$

Equation (III.15) was used to analyze melting line data from a thin film of $\text{Sm}_{1.85}\text{Ce}_{0.15}\text{CuO}_{4-y}$ [23] (Fig. III.8a), and a $\text{Bi}_2\text{Sr}_2\text{CaCu}_2\text{O}_8$ single crystal [24] (Fig. III.8b). The data for the $\text{Sm}_{1.85}\text{Ce}_{0.15}\text{CuO}_{4-y}$ sample are described well by Eq. (III.15) over the entire range of field/temperatures examined. Interestingly, while it is observed that the exponent s has a value similar to that found for the $\text{Y}_{1-x}\text{Pr}_x\text{Ba}_2\text{Cu}_3\text{O}_{6.97}$ and $\text{YBa}_2\text{Cu}_3\text{O}_{6.5}$ samples, the value of the Lindemann number, $c_L \approx 0.17$ for $\text{Sm}_{1.85}\text{Ce}_{0.15}\text{CuO}_{4-y}$ is nearly half of that found for the $\text{Y}_{1-x}\text{Pr}_x\text{Ba}_2\text{Cu}_3\text{O}_{6.97}$ and $\text{YBa}_2\text{Cu}_3\text{O}_{6.5}$ samples, and the value of $Q_0 \approx 19$ is greater than all of the above, even that of the highly point disordered $\text{YBa}_2\text{Cu}_3\text{O}_{6.5}$, $Q_0 \approx 17$. The relatively low value of c_L suggests that the vortex lattice in $\text{Sm}_{1.85}\text{Ce}_{0.15}\text{CuO}_{4-y}$ is much less stable in the presence of fluctuations than that in the $\text{Y}_{1-x}\text{Pr}_x\text{Ba}_2\text{Cu}_3\text{O}_{6.97}$ and $\text{YBa}_2\text{Cu}_3\text{O}_{6.5}$ systems. This may be due to effects from interactions of the vortex lines with the moments of the Sm ions, however this idea is speculative at this point and beyond the scope of this study.

Unlike the preceding examples, the $\text{Bi}_2\text{Sr}_2\text{CaCu}_2\text{O}_8$ data, can be fit by Eq. (III.15) in two segments, with a corresponding change in the critical exponent s . This is interpreted readily as evidence for a 3D-2D vortex glass transition in this highly anisotropic compound at $H_{2D} \approx 1$ kOe, in agreement with the conclusions of many different studies [11, 24, 54, 55, 56]. However, a change in the dynamical vortex behavior due to a crossover to a fundamentally different pinning regime will also result in a change of the critical exponent $s \equiv \nu(z + 2 - d)$ due to a change of the dynamical exponent z or possibly the anisotropy exponent ζ .

III.E.3 The vortex glass melting lines of MgB_2 and $\alpha\text{-Mo}_x\text{Si}_{1-x}$

To further demonstrate that the melting line equation developed here is not limited to just high- T_c compounds, Eq. (III.16) has been fit to vortex glass melting line data of two very different compounds, MgB_2 and $\alpha\text{-Mo}_x\text{Si}_{1-x}$.

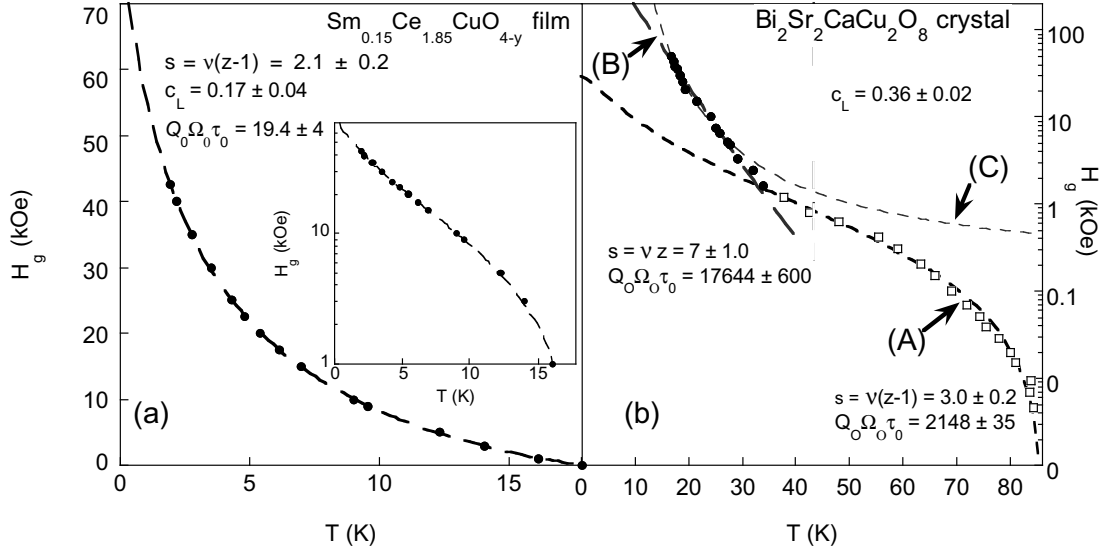


Figure III.8: (a) Fit of Eq. (III.15) to the melting line, $H_g(T)$, of a thin film of the electron-doped cuprate superconductor $\text{Sm}_{1.85}\text{Ce}_{0.15}\text{CuO}_{4-y}$ [23]. The inset shows the same data on a semi-log plot. (b) Fit of Eq. (III.15) to $H_g(T)$ of a $\text{Bi}_2\text{Sr}_2\text{CaCu}_2\text{O}_8$ single crystal [24]. A 3D - 2D transition at $H_{2D} \approx 1$ kOe is inferred by a corresponding change of the exponent, $\nu(z + 2 - d)$, from a 3D-XY like (A) to 2D-XY like (B) value. The upper portion of the curve is fit to the 2D melting line expression of Schilling et al. [24] (C) for comparison.

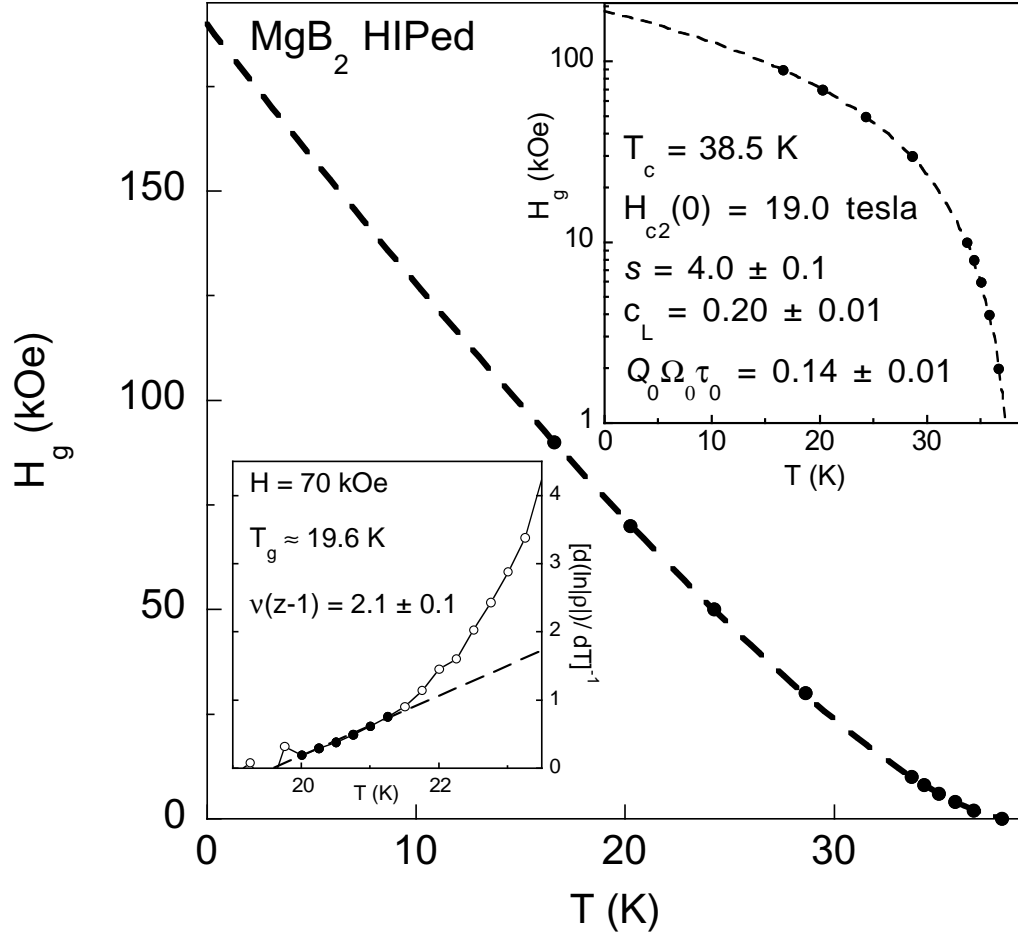


Figure III.9: Fit of Eq. (III.16) to vortex glass melting line, $H_g(T)$, data of a bulk MgB_2 sample prepared by hot isostatic pressing (HIP). The upper inset shows the same data on a semi-log plot. The lower inset shows resistivity data plotted as $[d \ln \rho(T)/dT]^{-1}$ vs T , demonstrating vortex glass behavior, with $\rho(T) \sim (T - T_g)^{\nu(z-1)}$. The value of the critical exponent $s \approx 4.0$, obtained from the fit of Eq. (III.16) to the melting line data, is a factor of two greater than that found from scaling of the resistivity data, $\nu(z-1) \approx 2.1$. Data taken from ref [45].

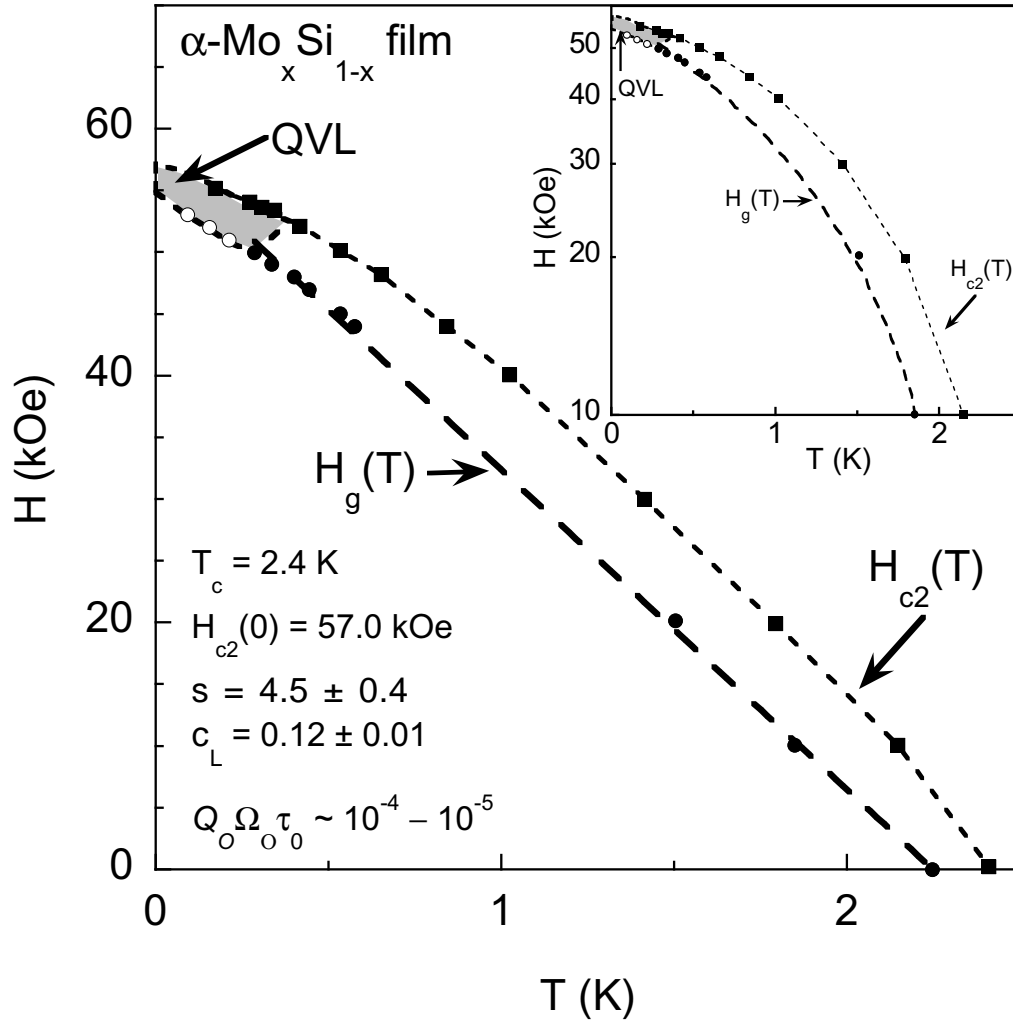


Figure III.10: Fit of Eq. (III.16) to vortex glass melting line, $H_g(T)$, data of a 100 nm thick film of α - $\text{Mo}_x\text{Si}_{1-x}$ ($x \approx 0.44$). The inset shows the the same data on a semi-log plot. Data taken from ref [46]. Okuma *et al.*, find $\nu \sim 1$ and $z \sim 5.4$ for all fields $H \lesssim 5\text{T}$ from scaling of the dc resistivity by the form $\rho(T) \sim (T/T_g - 1)^{\nu(z-1)}$. At fields above 5 T, Okuma *et al.* find evidence from scaling analysis of the ac resistivity, ρ_{ac} , of a quantum liquid vortex state. Thus the melting line terminates prior to connecting to the upper critical field line $H_{c2}(T)$.

The vortex glass melting line, $H_g(T)$, of a bulk sample of MgB_2 , was determined by a scaling of the dc resistive transition in accordance with the vortex glass theory of FFH, $\rho(T) \sim (T - T_g)^{\nu(z-1)}$ [45]. The fit of Eq. (III.16) to the data is shown in Fig. III.9. The exponent $s = 4.0$ obtained from the fit to the melting line data was obtained assuming that the limiting frequency $\Omega = \Omega_\mu$, *i. e.*, $\tilde{s} = s/2$, as in the case for the high- T_c samples considered above. However, the exponent $s_{VG} \equiv \nu(z - 1) \approx 2.1$ found from the scaling of the resistivity data, is approximately equal to half of the exponent s found from the fit of the melting line equation. This indicates that the energy gap, Δ , provides the scale of the energy cutoff which limits the dynamical properties of the vortices, and therefore, the correct expression for the quantum parameter q in this case is q_Δ (Eq. (III.14)).

The vortex glass transition has been shown directly to exist in amorphous films of the low temperature superconductor $a\text{-Mo}_x\text{Si}_{1-x}$ down to $T \sim 0.04 T_c$ by measurements of the dc and ac complex resistivities in constant fields [46, 47]. The transition was identified by the scaling relation of the dc resistivity stated above, and from the ac resistivity which, in agreement with FFH theory, follows a power-law frequency dependence $\rho_{ac} \propto f^{(z-1)/z}$ and the phase has a frequency-independent value $\phi_g = (\pi/2)(z - 1)/z$. The fit of Eq. (III.16) to the $a\text{-Mo}_x\text{Si}_{1-x}$ data is shown in Fig. III.10. In this case the exponent obtained from the melting line fit, $s \approx 4.5$ agrees well with the exponent $\nu(z - 1) \approx 4.4$ found by vortex glass scaling of the resistivity.

III.F Summary

The vortex glass melting lines, $H_g(T)$, of epitaxial thin film samples of $\text{Y}_{1-x}\text{Pr}_x\text{Ba}_2\text{Cu}_3\text{O}_{6.97}$ ($x = 0 - 0.4$) grown on LaAlO_3 substrates by pulsed laser ablation, as well as an ultra high purity oxygen deficient $\text{YBa}_2\text{Cu}_3\text{O}_{6.5}$ single crystal grown in a BaZrO_3 crucible, were measured in magnetic fields up to 45 tesla. Analysis of the evolution of vortex dynamic properties along the melting

lines of each system was carried out in the context of a modified melting line expression based upon the quantum- thermal-fluctuation model of Blatter and Ivlev [21]. We have also provided further evidence that the equation provides truly a universal description of the melting line in type-II superconductors, by fitting to vortex glass melting line data from a wide spectrum of superconducting systems; the electron-doped $\text{Sm}_{1.85}\text{Ce}_{0.15}\text{CuO}_{4-y}$ system, the highly anisotropic $\text{Bi}_2\text{Sr}_2\text{CaCu}_2\text{O}_8$ compound, and the non-cuprate non-High- T_c systems, MgB_2 and $\alpha\text{-Mo}_x\text{Si}_{1-x}$.

The melting line equation developed here provides an experimental means for determining the physical mechanism responsible for the energy scale which limits vortex motion at high frequencies. By determining the exponent s from vortex (or Bose) glass scaling analysis of the resistive transitions and comparing the to the exponent \tilde{s} obtained from the fit to the melting line data of Eq. (III.16) the appropriate cutoff frequency, Ω_μ or Ω_Δ can be determined.

It is found that the effective vortex mass is enhanced significantly by quantum fluctuations in the $\text{Y}_{1-x}\text{Pr}_x\text{Ba}_2\text{Cu}_3\text{O}_{6.97}$ and $\text{YBa}_2\text{Cu}_3\text{O}_{6.5}$ samples studied here, leading to a value of the kinetic cutoff frequency $\Omega_\mu \ll \Omega_\Delta$. By examining the values of the quantum parameter as a function of temperature, $q(t)$, it is shown that quantum fluctuations play an important role in the physics of the vortex-solid to vortex-liquid transition. The value of $q(t)$ is found to increase significantly with temperature, becoming very large as $T \rightarrow T_c$. This is explained primarily due to the increase of the size of the vortex cores as the melting line approaches the critical temperature, T_c ; the distance over which quantum fluctuations displace a segment of the vortex flux line. The vanishing line tension $\epsilon_\ell \propto \lambda^{-2} \sim (1 - t)$ and reduced superfluid density high-temperature/low-field region also likely contribute to quantum tunneling effects. The quantum tunneling length is found to be shortest in the relatively clean $\text{YBa}_2\text{Cu}_3\text{O}_{7-\delta}$ film, particularly at low temperatures. The tunneling distance is longest in the $x = 0.1$ film, and similar to or less than that of the $x = 0.1$ sample for the remaining films. This is understood

by the physical result that, up to a point, disorder actually promotes quantum fluctuations.

The idea that the intrinsic single vortex relaxation time, τ_r , changes as a function of temperature along the melting line is akin to the idea that the pinning potential changes along the melting line, an idea which Rydh *et al.* [42], used to modify the vortex glass theory of FFH. This modification of the FFH theory was motivated by a prior empirical scaling form of the vortex melting line by Lundqvist *et al.* [41], who referred to the model of Blatter and Ivlev [21] as possible theoretical support for their melting line expression. In the large Q limit, the expression for the melting line found here, reduces to that found by Lundqvist *et al.*, so, from the prior work of Lundqvist *et al.* and Rydh *et al.* it can be seen that there does indeed appear to be a relation between the thermal- and quantum-fluctuation Lindemann criterion based model of Blatter and Ivlev and the critical dynamic vortex glass model of FFH, and, by extension, the Bose glass model.

The exceptionally good agreement between the experimentally determined vortex lattice melting lines and the fits to the data by the melting line expression proposed here, and the agreement of the exponent s found from the above analysis with the exponent $\nu(z = 2 - d)$, found from scaling of the resistivity in the critical region of the vortex glass melting transition, supports the idea that dynamical properties of a vortex glass and of a single vortex line at the melting transition have the same physical origin; arising from the scaling properties of the fluctuation conductivity. By incorporating this essential idea into the work of Blatter and Ivlev [18, 21], a form of the melting line is arrived at which unifies the quantum/thermal nature of vortex fluctuations with the critical dynamic properties of vortices in the region of the melting line transition, providing a more complete picture of the physics involved.

Table III.1: Values of the Lindemann number c_L , critical exponent $s \equiv \nu(z + 2 - d)$, the quantum parameter $Q_0 \equiv \tilde{Q}_0 \Omega_0 \tau_0$ using Eq. (III.15), and the quantum of resistance $\tilde{Q}_u(0) \equiv \tilde{Q}_0$ for the data in Fig. III.1.

x	c_L	s	Q_0	\tilde{Q}_0
0	0.31	3.33	0.34	0.32
0.1	0.28	1.90	11.5	10.1
0.2	0.29	2.07	12.8	16.2
0.3	0.30	2.10	9.8	15.1
0.4	0.27	2.22	9.6	18.0
y=6.5				
0	0.28	2.21	16.9	37.6

Table III.2: Values of the Lindemann number c_L , critical exponent $s \equiv \nu(z+2-d)$, the quantum parameter $q_0 \equiv \tilde{Q}_0 \Omega_0 \tau_0$ using Eq. (III.16) for the data in Fig. III.2. The error values are $\Delta c_L \sim 0.02$, for all c_L , and $\approx 15\%$ for all values of s and q_0 . The values of the anisotropy parameter, γ for $\text{Y}_{1-x}\text{Pr}_x\text{Ba}_2\text{Cu}_3\text{O}_{6.97}$ are from ref. [49] and $\text{YBa}_2\text{Cu}_3\text{O}_{6.5}$ given in ref. [57]. The values of ξ are derived from the value of $H_{c2}(0)$ obtained from the fits to the data.

x	c_L	s	q_0	γ	$\rho_N(\mu\Omega\text{m})$	$\xi(\text{\AA})$
0	0.34	4.6	0.7	7.4	0.2	13
0.1	0.31	1.6	4.1	8.4	8.4	17
0.2	0.29	1.8	1.3	14.3	9.3	20
0.3	0.30	2.0	1.5	16.4	9.8	26
0.4	0.31	1.8	0.8	20.8	10.3	29
y=6.5						
0	0.28	2.0	0.8	65	2.2	22

A portion of the text and data of this chapter appears as it will be published in the articles, “Evolution of Vortex Dynamics Along the Vortex-Lattice Melting Line,” B. J. Taylor and M. B. Maple; “Quantum Fluctuations, Critical Dynamic Vortex Motion, and the Vortex Solid-Liquid Transition,” B. J. Taylor, D. J. Scanderbeg, M. B. Maple, C. Kwon, and Q. X. Jia. The dissertation author was the primary investigator and author of these articles.

Bibliography

- [1] A. Schilling, R. A. Fisher, N. E. Phillips, U. Welp, D. Dasgupta, W. K. Kwok, and G. W. Crabtree, *Nature* **382**, 791 (1996).
- [2] M. J. W. Dodgson, V. B. Geshkenbein, H. Nordborg, and G. Blatter, *Phys. Rev. Lett.* **80**, 837 (1998).
- [3] G. Blatter, M. V. Feigel'man, V. B. Geshkenbein, A. I. Larkin, and V. M. Vinokur, *Rev. Mod. Phys.* **66**, 1125 (1994).
- [4] M. P. A. Fisher, *Phys. Rev. Lett.* **62**, 1415 (1989).
- [5] D. S. Fisher, M. P. A. Fisher, and D. A. Huse, *Phys. Rev. B* **43**, 130 (1991).
- [6] D.R. Nelson and V.M. Vinokur, *Phys. Rev. Lett.* **68**, 2398 (1992); *Phys. Rev. B* **48**, 13060 (1993).
- [7] T. Giamarchi and P. Le Doussal, *Phys. Rev. B* **52**, 1242 (1995); **55**, 6577 (1997).
- [8] J. Lidmar and M. Wallin, *Europhys. Lett.* **47**, 494 (1999).
- [9] T. Hwa, D. R. Nelson, and V. M. Vinokur, *Phys. Rev. B* **48**, 1167 (1993).
- [10] K. H. Bennemann and J. B. Ketterson (Eds.), *The Physics of Superconductors, Vol I., Conventional and High- T_c Superconductors* (Springer-Verlag, Berlin Heidelberg, New York, 2003), p. 789 - 800.
- [11] M. B. Gaifulin, Y. Matsuda, N. Chikumoto, J. Shimoyama, and K. Kishio, *Phys. Rev. Lett.* **84**, 2945 (2000).
- [12] G. I. Menon, *Phys. Rev. B* **65**, 104527 (2002).
- [13] M. J. W. Dodgson, V. B. Geshkenbein, and G. Blatter, *Physica B* **280**, 220 (2000); M. J. W. Dodgson, A. E. Koshelev, V. B. Geshkenbein, and G. Blatter, *Phys. Rev. Lett.* **84**, 2698 (2000).
- [14] D. R. Nelson and B. I. Halperin, *Phys. Rev. B* **19**, 2457 (1979).
- [15] J. Kierfeld and V. Vinokur, *Phys. Rev. B* **61**, R14928 (2000).
- [16] E. H. Brandt, *Phys. Rev. Lett.* **63**, 1106 (1989).
- [17] A. Houghton, R. A. Pelcovits, and A. Sudbø, *Phys. Rev. B* **40**, 6738 (1989).
- [18] G. Blatter and B. Ivlev, *Phys. Rev. Lett.*, **70**, 2621 (1993).
- [19] G. P. Mikitik and E. H. Brandt, *Phys. Rev. B* **64**, 184514 (2001); **68**, 054509 (2003).

- [20] J. Kierfeld, V. Vinokur, Phys. Rev. B **69**, 024501 (2004).
- [21] G. Blatter and B. I. Ivlev, Phys. Rev. B **50**, 10272 (1994).
- [22] M. E. Fisher, M. N. Barber, and D. Jasnow, Phys. Rev. A **8**, 1111 (1973).
- [23] D. J. Scanderbeg, B. J. Taylor, and M. B. Maple, Physica C, (to be published).
- [24] A. Schilling, R. Jin, J. D. Guo, and H. R. Ott, Phys. Rev. Lett. **71**, 1899 (1993).
- [25] E. H. Brandt, J. Supercond. **6**, 201 (1993).
- [26] See Appendix A.
- [27] M. Charalambous, R. H. Koch, T. Masselink, T. Doany, C. Feild, and F. Holtzberg, Phys. Rev. Lett. **75**, 2578 (1995).
- [28] H. Suhl, Phys. Rev. Lett **14**, 226 (1965).
- [29] N. B. Kopnin and V. M. Vinokur, Phys. Rev. Lett. **81**, 3952 (1998).
- [30] M. W. Coffey, Phys. Rev. B **49**, 9774 (1994).
- [31] Ji-Min Duan and Eugen Šimánek, Phys. Lett. A **190**, 118 (1994).
- [32] E. M. Chudnovsky and A. B. Kuklov, Phys. Rev. Lett. **91**, 067004 (2003).
- [33] C. Caroli, P. G. de Gennes, and J. Matricon, Phys. Lett. **9**, 307 (1964).
- [34] K. Karrai, E. J. Choi, F. Dunmore, S. Liu, H. D. Drew, Qi Li, D. B. Fenner, Y. D. Zhu, and Fu-Chun Zhang, Phys. Rev. Lett. **69**, 152 (1992).
- [35] L.T. Sagdahl, S. Gjølmesli, T. Laegreid, K. Fossheim, and W. Assmus, Phys. Rev. B **42**, R6797 (1990).
- [36] C. C. Almasan, M. C. deAndrade, Y. Dalichaouch, J. J. Neumeier, C. L. Seaman, M. B. Maple, R. P. Guertin, M. V. Kuric, and J. C. Garland, Phys. Rev. Lett. **69**, 3812 (1992).
- [37] J. Bardeen and M. J. Stephen, Phys. Rev. **140**, A1197 (1965).
- [38] D. R. Nelson and V. M. Vinokur, Phys. Rev. B **61**, 5917 (2000).
- [39] N. B. Kopnin and M. M. Salomaa, Phys. Rev. B **44**, 9667 (1991).
- [40] Z. Schlesinger, R. T. Collins, F. Holtzberg, C. Feild, S. H. Blanton, U. Welp, G. W. Crabtree, Y. Fang, and J. Z. Liu, Phys. Rev. Lett. **65**, 801 (1990).
- [41] B. Lundqvist, A. Rydh, Yu. Eltsev, Ö. Rapp, and M. Andersson , Phys. Rev. B **57**, R14064 (1998).

- [42] A. Rydh, Ö. Rapp, and M. Andersson, Phys. Rev. Lett. **83**, 1850 (1999).
- [43] M. Andersson, A. Rydh, and Ö. Rapp, Phys. Rev. B **63**, 184511 (2001).
- [44] P. Minnhagen, Rev. Mod. Phys. **59**, 1001 (1987).
- [45] S. Li, B. J. Taylor, N. A. Frederick, M. B. Maple, V. F. Nesterenko, and S. S. Indrakanti, Physica C **382**, 177 (2002).
- [46] S. Okuma, Y. Imamoto, and M. Morita, Phys. Rev. Lett. **86**, 3136 (2001).
- [47] S. Okuma, S. Togo, and M. Morita, Phys. Rev. Lett. **91**, 067001 (2003).
- [48] G. Blatter, M. V. Feigel'man, V. B. Geshkenbein, A. I. Larkin, V. M. Vinokur, Rev. Mod. Phys. **66**, 1125 (1994).
- [49] C. C. Almasan and M. B. Maple, Phys. Rev. B **53**, 2882 (1996).
- [50] J. E. Sonier, R. F. Keiff, J. H. Brewer, D. A. Bonn, S. R. Dunsinger, W. N. Hardy, R. Liang, W. A. Macfarlane, T. M. Riseman, D. R. Noakes, and C. E. Stronach, Phys. Rev. B **55**, 11789 (1997).
- [51] J. E. Sonier, J. H. Brewer, R. F. Keiff, G. D. Morris, R. I. Miller, D. A. Bonn, J. Chakhalian, R. H. Heffner, W. N. Hardy, and R. Liang, Phys. Rev. B **55**, 11789 (1997).
- [52] M. H. S. Amin, I. Affleck, and M. Franz, Phys. Rev. B **58**, 5848 (1998).
- [53] M. P. A. Fisher, G. Grinstein, and S. M. Girvin, Phys. Rev. Lett. **64**, 587 (1990).
- [54] T. Shibauchi, T. Nakano, M. Sato, T. Kisu, N. Okuda, S. Ooi, and T. Tamegai, Phys. Rev. Lett. **83**, 1010 (1999).
- [55] Y. Yamaguchi, G. Rajaram, N. Shirakawa, A. Mumtaz, H. Obara, T. Nakagawa, and H. Bando, Phys Rev B **63**, 014504 (2000).
- [56] T. Shibauchi, L. Krusin-Elbaum, G. Blatter, and C. H. Mielke, Phys. Rev. B **67**, 064514 (2003).
- [57] T.R. Chien, W. R. Datars, B. W. Veal, A. P. Paulikas, P. Kostic, Chun Gu, and Y. Jiang, Physica C **229**, 273 (1994).

IV

Inhomogenous vortex matter in a high purity twinned YBa₂Cu₃O_{7- δ} single crystal

IV.A Introduction

The vortex lattice in weakly-disordered single crystals of high temperature superconductors (HTSC) is one of the classical systems for phase transition studies. It has been investigated extensively by means of magnetization, electrical resistivity, and specific heat measurements [1]. The generic magnetic field versus temperature, $H(T)$, phase diagrams of high- T_c cuprate superconductors such as YBa₂Cu₃O_{7- δ} and Bi₂Sr₂CaCu₂O_{4- δ} , continue to be investigated and updated with results from new experiments. In the case of YBa₂Cu₃O_{7- δ} single crystals, the evolution of the melting transition in the $H - T$ plane, $H(T)$, was first examined by Safar *et al.* up to 16 tesla with electrical resistivity measurements [2]. It was shown that there is a well-defined upper critical point $H_{\text{cr}}^{\text{u}}(T)$ which terminates the first order vortex lattice melting line at high field, above which the vortex-solid to vortex-liquid phase transition becomes continuous. It is now widely accepted that the melting line in clean YBa₂Cu₃O_{7- δ} single crystals consists of a (relatively) low

field section characterized by first order vortex lattice melting, and a high field section characterized by second order vortex glass melting, with an intervening critical point.

The evolution of the melting transition line and the critical point have been further examined by the introduction of artificially induced disorder. These studies indicate that there exist not just one, but two critical points: an upper critical point $H_{\text{cr}}^{\text{u}}(T)$ at high H and a lower critical point $H_{\text{cr}}^{\ell}(T)$ at low H , both of which are sensitive to microstructural disorder in the single crystals investigated [3]. The position of $H_{\text{cr}}^{\text{u}}(T)$ was shown to be dependent upon columnar disorder. For example, no upper critical point was found in high purity, fully oxygenated ($\delta = 0$) YBCO single crystal up to a field of 30 tesla, presumably due to the absence of oxygen vacancies [4]. Proton irradiation induced point disorder caused $H_{\text{cr}}^{\text{u}}(T)$ to decrease towards the intermediate field range, while columnar defects produced by heavy ion irradiation moved $H_{\text{cr}}^{\text{u}}(T)$ to higher fields. The lower critical point, $H_{\text{cr}}^{\ell}(T)$, was moved to higher fields with proton irradiation; while heavy ion irradiation resulted in a lower critical point at higher field, which separates a low field Bose-glass (BG) state to high field vortex lattice state [3, 5].

The temperature dependence of electrical resistivity in $\text{YBa}_2\text{Cu}_3\text{O}_{7-\delta}$ single crystals frequently shows a sharp kink or step at which the resistance rapidly drops to zero. This feature was shown to be hysteretic indicating a first order transition [6]. This conclusion is also confirmed by anisotropic specific heat measurements which showed a finite jump in specific heat at the melting point [7]. However, at temperatures just below the melting step, the sample resistance often vanishes with a small trailing tail [4], an indication that the sample is not in the true superconducting state with zero dissipation immediately below the melting temperature T_{M} . Additionally, while the trailing resistive tail usually becomes more prominent as point or line disorder is created artificially, the kink in $\rho(T)$ continues to be used to define a melting transition temperature [3]. In such a case, the superconducting transition is not adequately described only by a first

order melting transition. Measurements and a scaling analysis of $E(J)$ isotherms and measurements of the electrical resistivity $\rho(T)$ are needed to achieve a more complete picture of the phase transition dynamics.

Experimental evidence of the existence of a vortex-glass transition in weakly-disordered YBCO single crystals is well established [8, 9, 10, 11]. Universal scaling of $E(J)$ data on twinned YBCO single crystals was demonstrated by Yeh *et al.*, yielding universal static and dynamic exponents $\nu \sim \frac{2}{3}$ and $z \sim 3$, and indicating a second-order vortex-liquid to vortex-solid transition [8]. Besides conventional electrical transport measurements, other novel methods were also employed to study the $E(J)$ characteristics in YBCO single crystals, such as a contactless technique with subpicovolt voltage resolution, and have also provided strong evidence for a vortex-glass transition [9]. In addition, in single crystals that showed a first order melting transition, $E(J)$ data demonstrated Bose-glass scaling at magnetic fields below the lower critical point [5].

The recent development of BaZrO₃ crucibles and the subsequent growth of high purity YBCO single crystals using these crucibles have brought significant improvement in experimental results related to the flux lattice melting transition and the phase diagram of YBa₂Cu₃O_{7- δ} . Chemical analysis has shown a significant reduction in the level of impurities in YBCO single crystals grown in BaZrO₃ crucibles, compared to those grown previously in yttria-stabilized zirconia or alumina crucibles [12]. As a result, first order melting can be seen resistively even in heavily twinned YBCO single crystals [13], which was not possible previously. With this large reduction in the level of impurity disorder, the question can be asked whether the vortex-glass transition still exists in these very “clean” single crystals.

A study of the evolution of the vortex-solid to vortex-liquid transition in a high purity twinned YBCO single crystal sample that shows clear evidence of a first order melting transition is presented here. The melting transition was investigated via electrical transport, $\rho(H, T)$, and $E(J)$ isotherm measurements and

their scaling behavior in magnetic fields H up to 90 kOe. These samples are comparable in quality to those studied by Roulin et.al by means of adiabatic specific heat measurements that provided conclusive evidence of a first-order vortex-lattice melting line for various oxygen concentrations [4]. The vortex lattice melting line in this report is clearly established from electrical resistivity $\rho(T, H)$ measurements for $H \geq 8$ kOe. We address the question of whether or not a vortex-glass melting transition exists below the vortex-lattice melting temperature. Electric field vs current density $E(J)$ data over a field range that includes the entire first order melting transition provides clear evidence of a transition below the melting temperature to a true superconducting state with non-linear $E - J$ behavior ($E \sim \exp[-(j_c/j)^\mu]$). It is seen that the transition from a high temperature vortex liquid to a low temperature vortex-glass takes place through multiple dynamic regimes. The intermediate phase has been referred in earlier work as a “vortex slush” or plastic vortex flow regime [14, 15]. Analysis of the data in the context of the critical scaling model indicates the vortex matter in the single crystal is dynamically inhomogeneous, and that the nature of the inhomogeneity evolves with temperature. Scaling of the resistivity data points to the existence of two independent vortex-glass critical regions, with distinct critical exponents $\nu(z - 1)$, separated in temperature by a vortex-lattice melting transition. This scenario is further supported by the observation of scaling of the $E - J$ data wherein the upper and lower universal scaling branches do not scale in a consistent manner; *i.e.*, with the vortex-glass melting temperature T_g and the dynamic critical exponent z held fixed, a variation of the static exponent will improve the collapse of the data on one branch at the expense of the other. It is found that the dynamic scaling exponent z is non-universal for low H fields, and the static scaling exponent ν is unusually low. The extent to which the scaling exponents can be considered reliable in light of the apparent inhomogeneity and crossover between critical scaling regimes is addressed. The data are seen to support a scenario where the nature of the inhomogeneity is such that the intermediate phase involves a transition (in increasing

temperature) from a state where initially vortex lines in the twin boundaries are pinned and those within the bulk undergo driven plastic vortex flow, to a state where the vortex lines in and near the twin boundaries undergo driven disordered motion and those within the bulk move as an ordered lattice.

IV.B Experimental Details

BaZrO₃ powder was prepared from high purity BaCO₃(99.95%) and ZrO₂(99.95%) starting materials. The powder was reacted and sintered at 1200 °C three times with ball milling in between, followed by wet-milling for 24 hours to achieve grain size less than 1 micron. The BaZrO₃ crucibles were formed by cold isostatic pressing at 30 kpsi pressure, and sintered at 1700 °C for 24 - 48 hours. A self-flux method was used for the single crystal growth of YBCO with the atomic composition $Y : Ba : Cu = 1 : 18 : 42$. A flux-pouring technique which produces large single crystals, as described by Erb *et al.*, [16] was used. The as-grown single crystals are twinned, with a clean surface and typical dimensions of $\sim 1 \text{ mm} \times 1 \text{ mm} \times 0.05 \text{ mm}$. Twin boundaries are oriented at 45° to the edges of the well formed rectangular crystals. The as-grown single crystals were annealed in 1 bar flowing oxygen at 420 °C for 10 days and quenched (420 °C to 30 °C in 30 min) to optimize the oxygen content. The uncut sample used in this study had dimensions of $\ell \times w \times t = 0.80 \text{ mm} \times 0.35 \text{ mm} \times 0.056 \text{ mm}$, with voltage lead distance $d = 0.22 \text{ mm}$. Average distance between twin boundaries is $\approx 1\text{--}3 \text{ }\mu\text{m}$, as seen under a microscope. Three major aligned twinned regions $\approx 0.2 \text{ mm} \times 0.1 \text{ mm}$ in size (oriented at 45° to the crystal edges) extend over the entire crystal. The above annealing conditions and magnetically determined critical temperature $T_{c(\text{mag})} = 92.3 \text{ K}$ for this crystal are consistent with a value of oxygen content $7-\delta = 6.96 \pm 0.01$ [17, 18]. For electrical transport measurements, 0.002 inch diameter gold wires were attached to the single crystals using H20E silver epoxy. The samples with contacts were annealed in flowing oxygen at 200 °C for 2 hours

to reduce the contact resistance to less than $1\ \Omega$. The resistive superconducting critical temperature at $H = 0$ occurs at $T_c = 93.5\ \text{K}$ with a $0.3\ \text{K}$ transition width.

Measurements of the temperature and magnetic field dependence of resistivity $\rho(T, H)$ and the electric field vs current density isotherms $E(J)$ were performed on the single crystals using a standard four-wire technique. The crystal twin defects were oriented at 45° to the current flow. For any given value, the dc current was applied in alternating directions in order to avoid contact heating and to subtract offset voltage due to thermal *emfs*; this results in a high voltage resolution of a few nanovolts. Voltage data were taken with a Keithley 220 current source and a Keithley 2182 nanovoltmeter (set at 1 PLC sample rate, equivalent to a 60 Hz signal aperture). The voltage was measured 1 second after the current was applied to ensure any vortex flow had reached the steady state. Confirmation of a steady state vortex flow was established by observation of a voltage signal rise time of approximately 200–400 msec for measurements in the temperature range associated with the critical region of each applied magnetic field H . This observed voltage rise time is definitely associated with a delay of vortex flow in response to the applied dc current as the current source rise time is less than 6 msec. Additionally no such rise time was observed for measurements at temperatures outside the critical region. For all measurements, a dc magnetic field ranging from 0 to 90 kOe was applied parallel to the c -axis of the single crystals. The dc electrical resistivity $\rho(T)$ was measured by first cooling the sample in zero field to the lowest temperature. Data were collected on warming, with a temperature ramp rate of $0.1\ \text{K/min}$. A typical current value used in the $\rho(T)$ measurements was $500\ \mu\text{A}$, equivalent to a current density $J \sim 2.5\ \text{A/cm}^2$. For $E(J)$ measurements, the sample was initially cooled to the lowest temperature in zero field, the magnetic field was applied, and $E(J)$ isotherms were then measured in successive increasing temperature increments [19]. The temperature stability during the $E(J)$ measurements was better than $0.01\ \text{K}$.

IV.C Results and Discussion

Shown in Fig. IV.1(a) is electrical resistivity ρ vs temperature T data for a twinned YBCO single crystal sample in various magnetic fields H between 0 and 90 kOe, applied along the c -axis of the crystal. The $\rho(T)$ curves broaden rapidly with increasing magnetic field. A kink feature in the $\rho(T)$ data develops in magnetic fields $H \geq 8$ kOe, at a characteristic temperature T_M , where ρ abruptly drops to zero. This feature is generally attributed to a first order melting transition from a high temperature flux line liquid to a low temperature ordered flux line lattice [4]. As shown in Fig. IV.1(a), the kink feature becomes sharper with increasing magnetic field until 90 kOe, at which it begins to smooth out.

The temperature derivative of the electrical resistivity, $d\rho/dT$ vs T for various values of H , derived from the $\rho(T)$ data in Fig. IV.1(a) are shown in Fig. IV.1(b). The melting temperature T_M can be clearly determined from the temperature of the peak in the $d\rho(T)/dT$ vs T . The width of the peak in the $d\rho/dT$ vs T plots remains narrow (~ 0.5 K) in fields between 10 and 80 kOe, only starting to broaden at $H = 90$ kOe, suggesting the approach of an upper limit at which the vortex lattice melting transition vanishes [4]. Displayed in the inset of Fig. IV.1(b) are plots of $d\rho(T)/dT$ vs T at low H ranging from 2 to 8 kOe. The sharp peak associated with the melting transition is no longer observable below $H = 8$ kOe. This is consistent with previous reports of a lower critical point on the melting line, below which the discontinuous melting transition is replaced by a continuous melting transition. This has been shown via electrical resistivity data for proton irradiated untwinned single crystal YBCO samples grown conventionally in gold crucibles [3], as well as for twinned single crystals grown in BaZrO₃ crucibles for various oxygen concentrations by adiabatic specific heat measurements [4]. The latter samples were grown in the same manner as those reported in this study.

The electrical resistivity $\rho(T)$ of the YBCO single crystals grown in BaZrO₃ crucibles clearly demonstrates the significance of sample quality in the

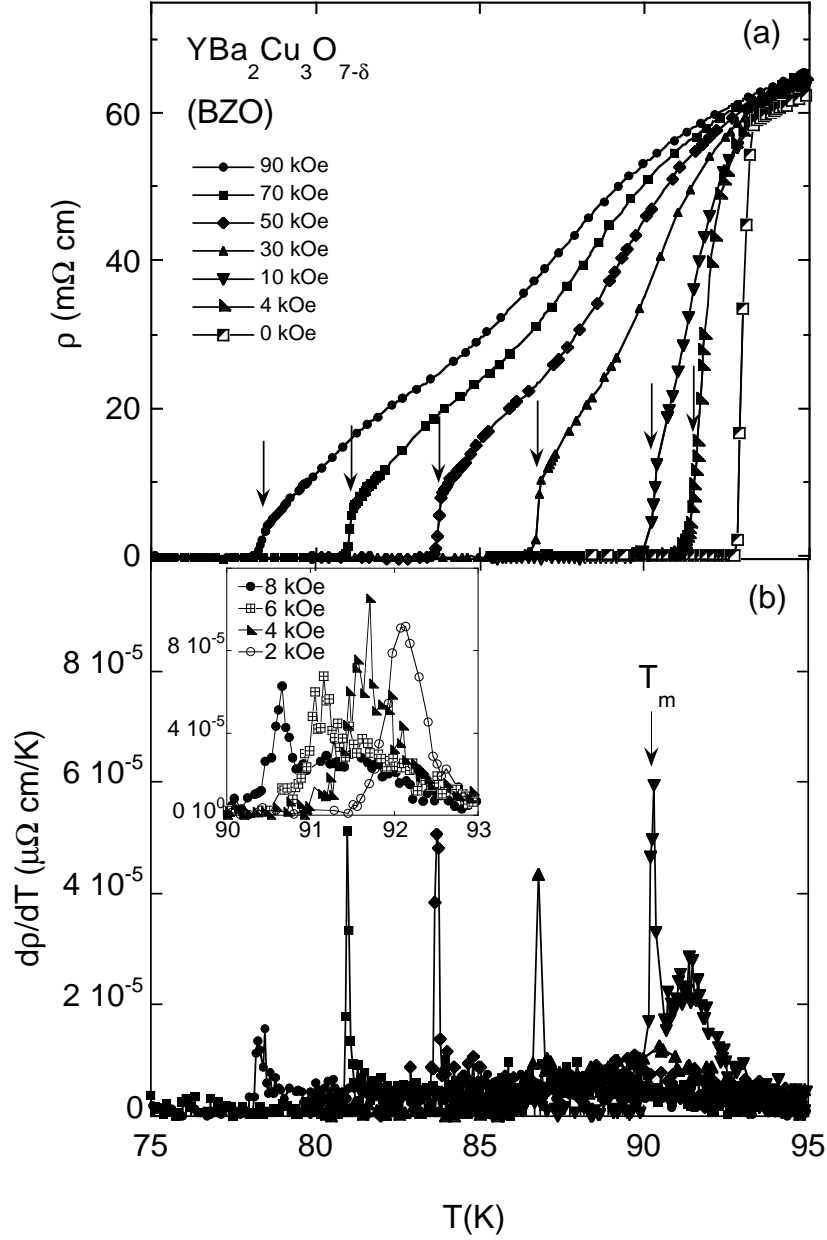


Figure IV.1: (a) Electrical resistivity ρ of the twinned YBCO single crystal as a function of temperature T and applied magnetic field H . The melting of the flux line lattice is indicated by the sudden vertical drop of the electrical resistivity. (b) The delta function-like peak in the temperature derivative of electrical resistivity, $d\rho/dT$, was used to determine the melting transition temperature T_M . This peak becomes non-distinguishable at fields lower than 8 kOe as shown in the inset.

electrical transport studies of phase transitions in the vortex ensemble. Even with the presence of twin boundaries, the step feature associated with the flux line lattice melting is still clearly observable in the field range between 8 kOe and 90 kOe. The melting transition has been previously observed via electrical resistivity in twinned YBCO single crystals which were grown with the same method used here in BaZrO₃ crucibles [13]. The melting transition was only reported previously via resistivity measurements in conventionally grown detwinned YBCO single crystals [3, 5]. Based on our results, we can determine the lower critical point, $H_{\text{cr}}^{\ell}(T)$, for our single crystal to be about 8 kOe.

Measurements of electric field vs current density $E(J)$ isotherms were performed on the same YBCO single crystal sample at constant applied magnetic field H . Two representative sets of $E(J)$ isotherms taken at $H = 1$ kOe and $H = 90$ kOe are presented in Fig. IV.2 on a log-log scale plot. The data obtained for this sample are comparable to those obtained by Worthington *et al.*, particularly for fields $H \geq 8$ kOe, who reported $E - J$ behavior (shown as resistivity vs. current density, ρ vs. J) of single crystal YBa₂Cu₃O₇ samples with enhanced disorder, grown with a conventional molten flux method [14]. The data of Worthington *et al.* have been widely regarded as evidence for the existence of both vortex-melting and vortex-glass transitions, separated in temperature. The significant feature in the $\rho - J$ data (plotted on a log-log scale) is an intermediate temperature and low current density region where the isotherms display linear behavior. This region separates the upper vortex-lattice melting temperature T_{M} from the data displaying definite downward exponential curvature, beginning at a temperature T_g . This was interpreted as evidence for an intermediate vortex matter phase bounded by the first-order phase transition temperature T_{M} and the second-order phase transition temperature T_g .

The data in Fig. IV.2(b) ($H = 90$ kOe) (and for all data with $H \geq 8$ kOe) are remarkably similar to those reported by Worthington *et al.* for $H = 30$ kOe - 70 kOe. The intermediate linear (on a log-log plot) $E - J$ regime in the low field

$E - J$ data in Fig. IV.2(a) is not as readily apparent as at high fields, yet is weakly retained as demonstrated by the ‘S’ shaped isotherms, $T = 91.8 - 92.0$ K. The data in low field are more consistent with the gradual evolution from the high temperature normal state to the superconducting state via a second order vortex-glass melting phase transition, consistent with the vortex-glass theory (VG) of Fisher, Fisher, and Huse [20]. The negative downward curvature in the $E(J)$ isotherms at lower T is consistent with the behavior of a frozen vortex glass state.

Even though there is an intermediate linear region in the single crystal $E(J)$ isotherm data (Fig. IV.2), the scaling ansatz of the Fisher-Fisher-Huse (FFH) vortex-glass transition theorem was applied to the data for all fields H . The FFH scaling functions are $(E/J)|T - T_g|^{\nu(d-2-z)}$ and $(J/T)|T - T_g|^{(1-d)\nu}$, where ν and z are the static and dynamic scaling exponents and d is the dimensionality of the system [20]. The glass transition temperature T_g was first determined from the critical isotherm with the single power law $E \sim J^{(z+1)/d-1}$. This curve was identified by plotting the power of the $E(J)$ curves, $d\ln E/d\ln J$ vs J and choosing the curve with a $d\ln E/d\ln J$ value that is constant (independent of J) [19]. For $H = 1$ kOe, the best curve thus identified ($d = 3$) gives $T_g = 91.7 \pm 0.1$ K and $z \sim 10.0 \pm 3$. The method used here for determining the error for z is based on the preceding $d\ln E/d\ln J$ plot. A range of values for $(z+1)/2$ was established about the isotherm displaying the constant power law exponent. This range was chosen so that it does not include data from adjacent isotherms. The error for ν follows by observing the best scaling of the data with respect to ν by holding the previously determined values of T_g and z fixed, and noting the range of values of ν over which a deviation from this is small. As the value of ν is varied, the slopes of the overlapping portions of the adjacent (in temperature) scaled isotherm data change with respect to the slope of a given scaled isotherm. A mismatch of slope is readily seen as the value of ν is varied away from the above determined value by more than a small range. This range determines the error reported for ν .

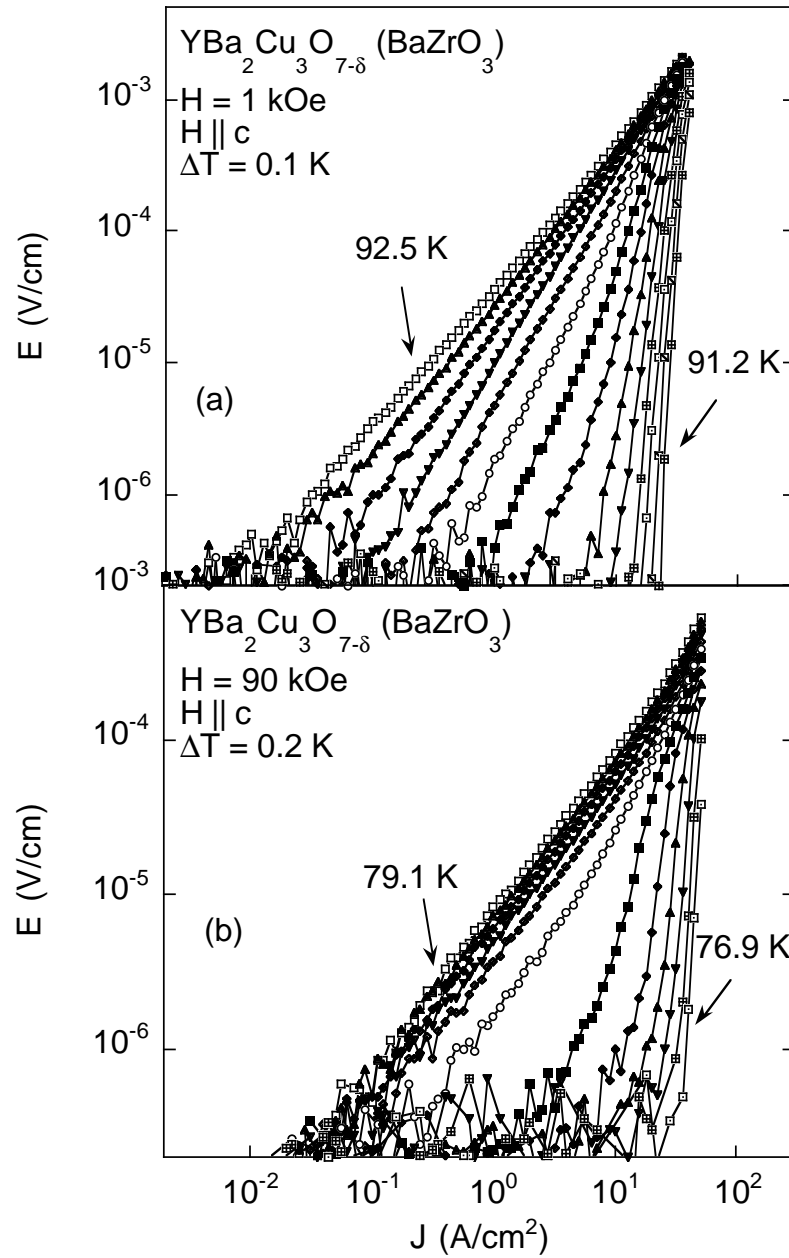


Figure IV.2: Electric field versus current density, $E(J)$, isotherms of the YBCO single crystal for (a) $H = 1$ kOe and (b) $H = 90$ kOe, plotted on a log-log scale. The characteristic differences between $E(J)$ isotherm sets at high field and low field are consistent with the existence of a lower critical point, that separates the first order melting transition at high field and continuous transition at low field.

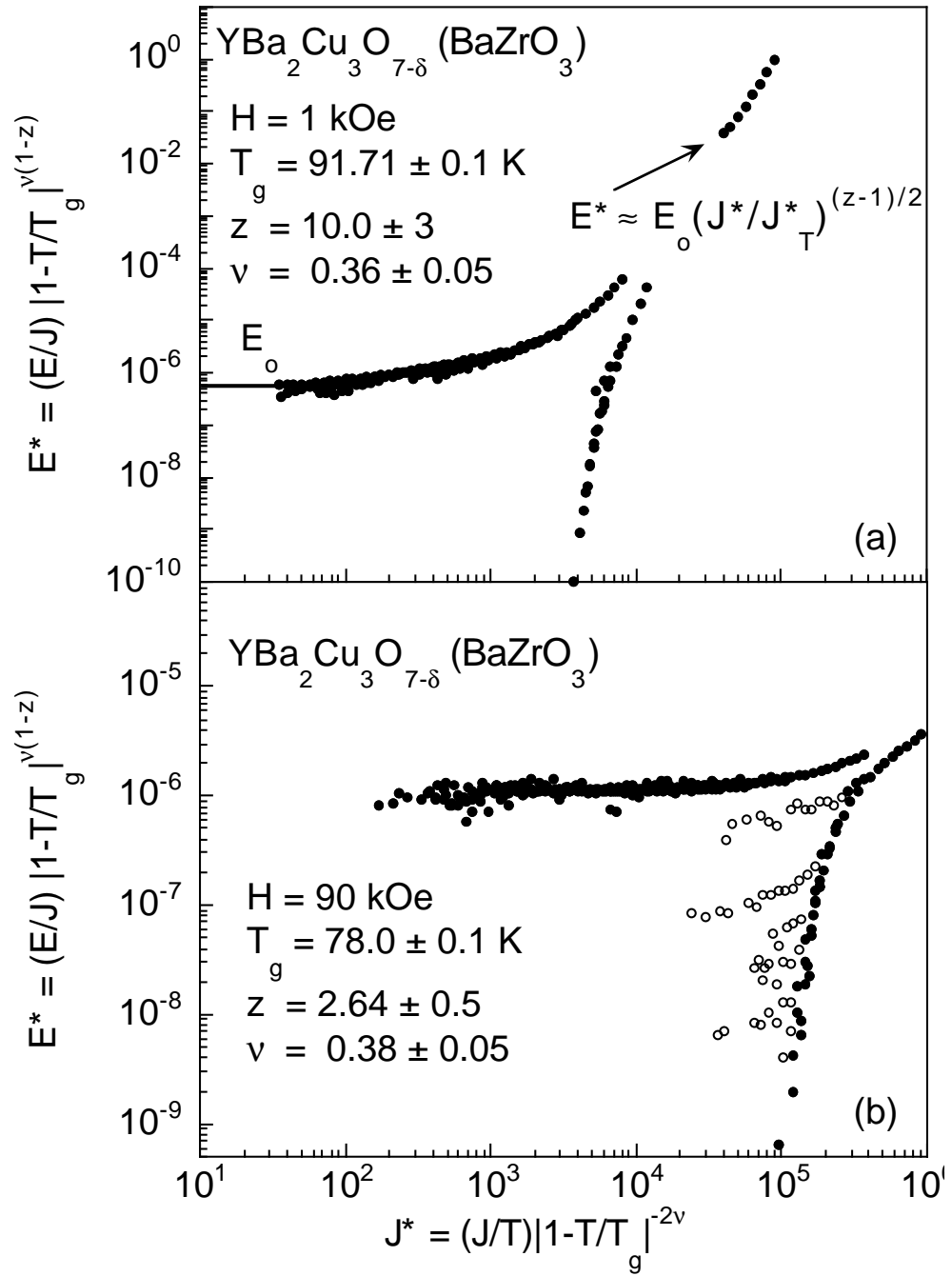


Figure IV.3: The vortex-glass scaling analysis of the $E(J)$ isotherm sets for (a) $H = 1$ kOe and (b) $H = 90$ kOe. The open circles correspond to the $E(J)$ data which exhibits the intermediate linear behavior.

The scaling functions corresponding to the $E(J)$ data at $H = 1$ kOe and $H = 90$ kOe are shown in Fig. IV.3 (a) and (b). To scale the $E(J)$ data for a given field H , the exponent ν was varied while fixing T_g and z to obtain the best collapse possible. Then, the values of T_g and z were varied slightly and in a correlated manner to further improve the scaling within the bounds of the error from the determination of T_g . The static exponent ν remains constant ($\nu \sim 0.37$) for all fields. On the other hand, the dynamic exponent z is larger ($z \sim 5 - 10$) below the lower critical point $H_{\text{cr}}^{\ell}(T)$ of the melting line, but drops to $z \sim 2.64$ for all $H \geq H_{\text{cr}}^{\ell}(T)$. The error of ν and z for $H \geq 20$ kOe were estimated to be 0.05 and 0.1, respectively. The error in z increases rapidly for lower H fields ($\Delta z \sim 2-3$), while the error in ν remains the same.

The electrical resistivity in the critical region ($T \geq T_g$) takes the scaling form $\rho \sim |T - T_g|^{\nu(z-d+2)}$ [8]. The value of $\nu(z-1)$ is obtained by plotting $d(\ln \rho)/dT$ vs. T , as shown Fig. IV.4. The data over which a linear fit is applied is shown in open circles. Two important features are seen for each field H shown. The first is the location (or lack thereof) of a vortex-lattice melting temperature T_M , seen as a kink in the region over which a linear fit is applied. For $H = 6$ kOe, no kink is present, consistent with $H < H_{\text{cr}}^{\ell}(T)$ where only a vortex-glass melting transition takes place and there is no vortex-lattice melting temperature. At $H = 8$ kOe and 70 kOe, the kink is easily seen as indicated by the arrow locating T_M . By $H = 90$ kOe, the kink has mostly disappeared, indicating the approach of H to $H_{\text{cr}}^u(T)$. The second feature noted is the location of the upper temperature of the critical region denoted T_g^u . This temperature lies above the vortex-lattice melting temperature for all fields for which first order melting is observed. This would seem to suggest, in this case, that the vortex matter in the single crystal is *inhomogeneous*, with the result that the vortex-lattice melting and vortex-glass melting transitions are independent phenomena. If instead, the *entire* vortex-matter ensemble within the sample were to undergo (upon warming) a vortex - glass melting transition followed by a vortex - lattice melting

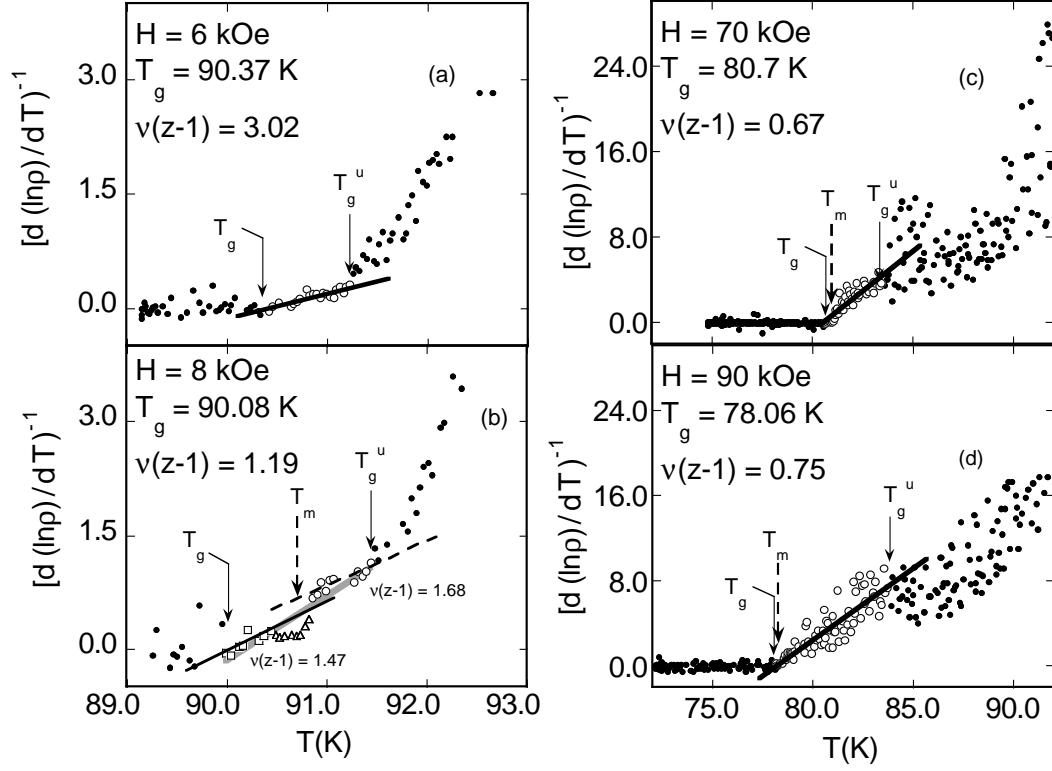


Figure IV.4: $[d \ln(\rho)/dT]^{-1}$ vs T for various fields H . The linear fit is applied to the data displayed as open circles (figures a, c, d), for which T_g is determined by the y-axis intercept and $\nu(z-1)$ is the reciprocal of the slope. Additional fits to the data for temperatures $T < T_M$ (open squares) and $T > T_M$ (open circles) separately are shown in figure b, with the different values of $\nu(z-1)$ indicated (the value of $\nu(z-1) = 1.19$ is from the linear fit to all open circles, squares, and triangles).

transition into the liquid state, the critical fluctuations of the second-order vortex-glass state must cease at a temperature T_g^u *below* the vortex-lattice melting temperature T_M so that the lattice may form and then melt, a rather unphysical scenario and contradictory to the observation of resistive critical scaling behavior at temperatures above T_M . A closer examination of the scaled resistivity data (to be commented on in detail below) indicates that there are actually two vortex-glass regimes with *different* critical behavior separated in temperature by the vortex-lattice melting phenomenon at T_M . This is in contrast to the “vortex slush” scenario in which the intervening state *between* T_g and T_M is a sluggish vortex-liquid [14].

At this point, the difficulties of obtaining a reasonable scaling of the $E - J$ and $\rho(T)$ data, the validity of applying the FFH theorem, and the critical exponent values and errors must be addressed. As noted above, an intermediate linear $E - J$ regime separates the low and high temperature isotherms, interrupting the smooth evolution characteristic of a second order vortex-glass melting phase transition. This is observed definitively at high fields $H \geq 8 \text{ kOe}$ and to a much weaker extent at low fields. However, for all H fields, the data display a temperature below which $E(J)$ exhibits a response characteristic of a true superconducting state, $E \sim \exp[-(j_c/j)^\mu]$. In attempting to scale the $E - J$ data it was noticed that the upper and lower scaled curves did not scale in a mutually consistent manner. That is, the improvement of the quality of the scaling of the $T < T_g$ data came at the expense of the $T > T_g$ data and vice versa. The quality of scaling was determined by the low temperature data only, since the data with $T > T_g$ are approaching T_M , and it was not clear what influence the proximity of the first order phase transition would have on the $E - J$ scaling analysis. As can be easily seen in Fig. IV.3, the intermediate linear data of the high H field $E - J$ data, denoted as open circles, do not lie on the either of the two universal scaling curves.

As stated above, evidence for two entirely different vortex-glass regimes is obtained from the scaled resistivity data. A closer examination of the portion

of the plot of $[d\ln(\rho)/dT]^{-1}$ vs T over which the linear fit shown is applied (open circles) reveals a significant detail, namely, the slope of the plot is steeper at temperatures $T < T_M$ than it is at temperatures $T > T_M$, indicating directly different values of the critical exponents $\nu(z-1)$. This is most easily seen in Fig. IV.4(b) where additional lines are fit to the upper and lower temperature portions with the corresponding values of $\nu(z-1)$ indicated. If the linear fit shown in Fig. IV.4 (b),(c), and (d) to $[d\ln(\rho)/dT]^{-1}$ vs T , is only applied to data for which $T < T_M$, the values obtained for $\nu(z-1)$ increase significantly for the intermediate fields $8 \text{ kOe} \leq H \leq 70 \text{ kOe}$, from $\sim 0.64 - 1.2$ to $\sim 1.5 - 3.0$. This disagrees with the results from $E - J$ scaling where $\nu(z-1) \sim 0.62 - 1.6$. However, the intermediate H field values of $\nu(z-1)$ from the above $T < T_M$ constrained linear fit are in close agreement with the low field ($H \leq 6 \text{ kOe}$) values of $\nu(z-1) \sim 3.0 - 3.3$ obtained from fitting to $[d\ln(\rho)/dT]^{-1}$ vs T for which there is no melting temperature constraint. This would seem to indicate that the single vortex-glass regime observed at low fields ($H \leq 6 \text{ kOe}$) is the same as that observed at intermediate fields ($8 \text{ kOe} \leq H \leq 70 \text{ kOe}$) at temperatures $T < T_M$. At intermediate fields and temperatures $T > T_M$, $\nu(z-1) \sim 0.7 - 1.7$ in close agreement with the values obtained from $E - J$ scaling. Consequently, the vortex-glass regime at intermediate fields and at temperatures $T > T_M$ likely originates from entirely different vortex-glass dynamics. At $H = 90 \text{ kOe}$ the restriction of fitting the data only to $T < T_M$ changes the value of $\nu(z-1)$ negligibly, again supporting the conclusion of nearing the upper critical point $H_{\text{cr}}^u(T)$.

Past the lower critical point $H_{\text{cr}}^\ell(T)$, on the vortex lattice melting line, YBCO has been shown to exhibit Bose-glass scaling behavior at low fields in heavily twinned samples [21]. Assuming a Bose-glass for low fields ($d=4$), the $E - J$ data are scaled as $(E/J)|T - T_g|^{\nu(2-z)}$ and $(J/T)|T - T_g|^{(-3\nu)}$, resulting in critical exponent values of $\nu \sim 0.29$ and $z \geq 8.9$. This disagrees significantly with the reported values of $\nu \approx 1.0$ $z \approx 6$ [21], leading to the conclusion that Bose-glass scaling is not likely the case here. The existence of a Bose-glass transition cannot

be ruled out though, since it appears there may be two separate second-order transitions, with different critical temperatures T_g and critical exponents z and ν , complicating definitive $E - J$ scaling results. This will be commented on further below. The considerable difference between the values of the critical exponents found here ($\nu \approx 0.37, z \approx 2.64$) and those typically reported ($\nu \approx \frac{2}{3} - 2, z \approx 3 - 6$) [8, 22] raises the question as to the accuracy of the former. However, it has been shown that the critical correlation length exponent ν must satisfy $\nu \geq 2/d$ for systems where disorder is irrelevant to the critical behavior [23]. The value of $\nu \approx 0.37 < 2/3$ obtained here may be the result of the “cleanness” of the BaZrO₃ grown YBa₂Cu₃O_{7- δ} single crystals, in the context of the criterion of Harris [24]. Harris argues that wherein if $\nu < 2/d$ for a uniform system, then the critical behavior of the corresponding disordered system must be different.

Even though the accuracy of the scaling exponent values is questionable, the data do definitely demonstrate a scaling of the quality that is typically reported. A scenario investigated by Crabtree et al. is considered as a likely model to explain the results obtained here [25]. Crabtree et al. produced numerical simulations of a driven vortex system in a clean twinned YBCO ‘sample’, a scenario applicable to the sample examined in this work. The twin boundaries were modelled at 45° to the driving Lorentz force (and thus to the applied current) as was the case in our resistivity $\rho(T)$ and $E - J$ measurements. The results of low, intermediate, and high current regimes are outlined below, and are illustrated in the lower portion of Fig. IV.5.

Low Current: Vortices in the twin boundary are stationary. The twin boundaries are impenetrable, and highly correlated plastic motion occurs in the bulk. Motion within the bulk is determined by the twin boundaries. The twin boundary is seen by the vortices as an extended object.

Intermediate Current: Vortices in the twin boundary move under the Lorentz force of an applied current. The vortices may cross the twin boundary at weak spots. Vortices move primarily parallel to the boundary and internal to it.

Vortex motion within the bulk is elastic and the direction is determined primarily by the Lorentz force. The twin boundary is no longer an extended object but a line of random pinning wells, and motion within and near to the twin boundary is random.

High current: Motion is elastic everywhere, and the twin boundaries become nearly irrelevant to the motion of the driven vortices.

In the resistivity measurements, the current is low (kept within the vortex glass scaling regime) and the temperature is swept with the applied field H held fixed. At low temperatures, the vortex matter in the bulk is plastic and will exhibit critical behavior [26] as the temperature increases from the true superconducting state through a vortex-glass melting temperature T_g . The size of the correlated vortex regions is bounded by the bulk area between the interleaving twin boundaries and the usual interlayer interactions. As T increases further, the vortex matter and sample then effectively enter the intermediate current scenario. The vortices within and in close proximity to the twin boundaries are now moving in a disordered manner, and will also exhibit critical behavior. The vortices in the clean bulk are uniformly driven and form a lattice which melts [15] at the critical temperature $T_M > T_g$, becoming a liquid, with perhaps a portion joining the glassy ensemble. The glassy regions are now elongated objects localized around the twins, with two characteristic coherence lengths ξ_\perp and ξ_\parallel (with respect to the twin boundary) with the correlation fluctuations (presumably) primarily in the parallel direction. This scenario then implies that there are in fact two different vortex-glass states, the latter coexisting with, and bounding regions of a vortex-lattice. This may explain the difficulty of obtaining a readily correlated scaling of the upper and lower branches of the $E(J)$ isotherms via the FFH ansatz. Such a scenario is also compatible with the observation that restricting the linear fit to the data satisfying $T < T_M$ in the plots of $[d\ln(\rho)/dT]^{-1}$ vs T resulted in values of $\nu(z-1)$ in the intermediate fields $8 \text{ kOe} \leq H \leq 70 \text{ kOe}$ that agree with the $\nu(z-1)$ values below 6 kOe instead of those obtained from $E(J)$ scaling. It appears then,

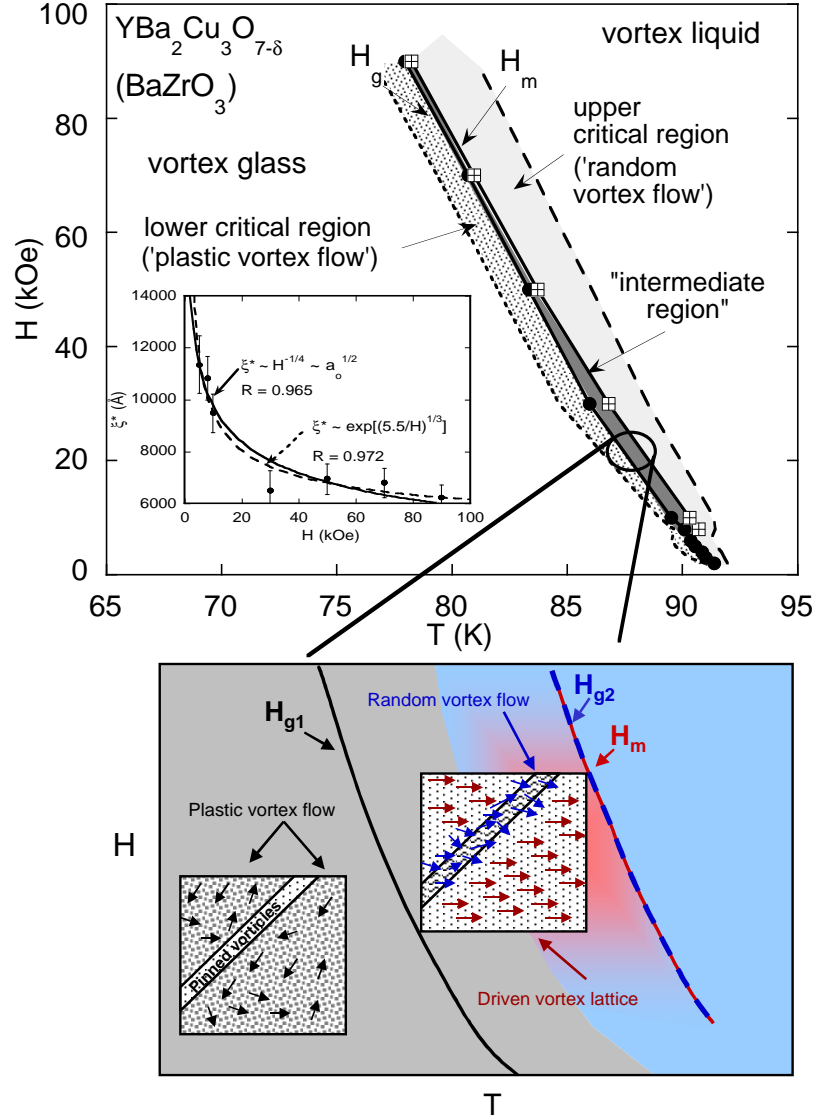


Figure IV.5: Magnetic field versus temperature, $H(T)$, phase diagram of the YBCO single crystal grown in BaZrO_3 crucibles. Inset: the H dependence of the correlation length at the boundary of the critical region, ξ^* , derived from the scaling of $E(J)$ isotherms. An exponential and power law fit as a function of field H are indicated for comparison. No particular physical model is inferred by the fits. Lower portion: Illustration showing an enlarged portion of the phase diagram where it is proposed that the presence of crystal twin boundaries produces a crossover regime where first a order vortex-lattice melting behavior and a continuous vortex-glass melting transition coexist. See text for further details.

from the resistivity data (plotted as $[d\ln(\rho)/dT]^{-1}$ vs T) that there are in fact two critical regions, above and below T_M with differing critical exponent $\nu(z-1)$. The two glassy states could conceivably have differing critical exponents due to the different geometrical constraints outlined above, and must have different characteristic vortex-glass melting temperatures T_g .

This suggested scenario would not contradict the observation of a vortex-lattice melting via adiabatic specific heat measurements on samples comparable to that examined here [4]. The cleanness of the sample would not require that the vortices within the bulk be driven by a current to form an ordered lattice. It is anticipated that de-twinning the sample would remove all vortex-glass like behavior below the melting transition.

Most experimental results for clean high- T_c single crystal samples indicate the connection of the vortex-lattice melting and vortex-glass melting lines at a critical point at high field. This has been the most widely accepted $H(T)$ phase diagram for YBCO single crystals, including the above mentioned high-purity samples of Roulin *et al.* grown in BaZrO₃ crucibles. However, the trailing tail at temperatures below T_M in the resistivity $\rho(T)$ data, the separation of the isotherm associated with the melting temperature from those seen to exhibit a true superconducting response ($E \sim \exp[-(j_c/j)^\mu]$) in the $E-J$ data (for $H \geq 8$ kOe) and, to a lesser extent, the critical scaling results of the $E-J$ data, all point to a scenario where a vortex-glass melting line exists at a temperature below the vortex-lattice melting line at fields ranging from the upper critical point $H_{cr}^u(T)$ past the lower critical point $H_{cr}^\ell(T)$.

The magnetic field H versus temperature T phase diagram of the twinned YBCO single crystal is shown in Fig. IV.5. The vortex-lattice melting line $H_M(T)$ was determined from the peak in the temperature derivative of the electrical resistivity $d\rho/dT$ vs T . Below the lower critical point $H_{cr}^\ell(T) = 5$ kOe, the peak in $d\rho/dT$ vs T is no longer distinguishable from the main superconducting transition. The vortex-glass melting line $H_g(T)$ is determined from the vortex-glass (VG)

scaling of the $E(J)$ isotherms, which lies at a slightly lower temperature below the vortex-lattice melting line $H_M(T)$. The intermediate region is seen to narrow at high field H , suggesting an eventual connection at the critical point $H_{cr}^u(T)$ where the vortex-lattice melting gives way to an entangled vortex-glass melting transition [5]. If this is indeed the case, it would not contradict, but instead supplement, previously established phase diagrams, which are widely accepted. Also shown are the upper (long dash) and lower (short dash) boundaries of the critical region. The upper boundary is readily established by the value of T_g^u for each field H . The lower boundary, which is usually established as $T_g - T_g^u$, is instead determined by the range of temperature of the isotherms on the lower branch of the scaled $E(J)$ data. This is done since the critical behavior at temperatures $T < T_M$ is interrupted by the crossover of vortex regimes, and the temperature establishing the boundary can not be obtained by the usual criterion of the extent of the linear fit to the scaled resistivity data. Voltage data resolution and heating due to high applied currents limits the range of observable isotherms. Thus the low temperature boundary of the critical region shown should be considered an upper limit in temperature.

In the case of clean single crystals, the weak-pinning limit is most relevant, and the vortex-lattice order extends over large regions which are characterized by the Larkin–Ovchinnikov length, L_p [27]. Vortex glass scaling occurs only when the VG correlation length ξ_{VG} exceeds L_p . Thus, estimation of the VG correlation length ξ_{VG} gives an upper limit of the Larkin–Ovchinnikov length L_p , which is the size of the ordered flux-line lattice regions. ξ_{VG} can be estimated using the analysis of Xenikos *et. al* [28]. The temperature of the upper limit of the critical region, T_g^u , can be used to determine a vortex correlation length ξ^* , which represents the shortest length, above T_g , over which the motion of the vortex segments is still correlated. Yeh et al. applied a similar analysis to the $E(J)$ data of twinned conventionally grown YBCO samples, and reported the value of the zero temperature correlation length $\xi_{VG}(T = 0) \equiv \xi_{0VG}$ of the vortex glass ensemble [8]. The field

dependence of $\xi_{0VG}(H)$ for $10 \text{ kOe} < H < 70 \text{ kOe}$ increased exponentially from $\sim 400 \text{ \AA}$ to $\sim 800 \text{ \AA}$. The low field behavior of $\xi_{0VG}(H)$ is different than in high fields. $\xi_{0VG}(H)$ increases rapidly from $\sim 200 \text{ \AA}$ to the initial high field value of $\sim 400 \text{ \AA}$.

The same analysis was applied here to examine how these quantities evolve with applied field H . The zero temperature vortex-glass correlation length ξ_{0VG} was calculated from the preceding scaling of E and J for each applied field H . The values of $\Delta\xi_{0VG}$ reported here have been obtained by a series of variations of the parameters T_g , z and ν . These values are considered reasonable as an estimate of the error. The analysis did not yield the exponential behavior as a function of field as seen by Yeh *et al.* Instead, we see ξ_{0VG} decreases from $\sim 2200 \text{ \AA}$ for $H \leq 10 \text{ kOe}$ to $\xi_{0VG} \sim 2000 \text{ \AA}$ for $H > 30 \text{ kOe}$. With $\xi^* = \xi_{0VG}/(1 - T_g/T_g^u)^\nu$, $\Delta\xi^* = \Delta\xi_{0VG}/(1 - T_g/T_g^u)^\nu$ [1, 20], this yields a coherence length (Fig. IV.5 inset) at the critical region boundary that appears to decrease exponentially as $\xi^* \sim \exp^{(5.5/H)^{\frac{1}{3}}}$, or as a power law with $\xi^* \sim H^{1/4}$. (These fits are intended to illustrate the trend of ξ^* decreasing with field and are not necessarily indicative of any physical model.) As pointed out by Chayes *et al.* [23], in systems with intermediate phases or first-order transitions, it is possible that a finite-volume event such as that associated with an intrinsic correlation length ξ is undefinable or yields a “correlation length” unrelated to the intrinsic ξ .

The existence of a vortex-glass state is well established by the data reported herein. However, a certain amount of caution should be taken as to the values arrived at for the critical exponents ν and z , and correlation length ξ . The trends with field and temperature, though, should be considered reliable. The values obtained for the critical exponents and vortex-glass correlation length are summarized in Table IV.1.

IV.D Summary

In summary, electrical transport properties of high purity $\text{YBa}_2\text{Cu}_3\text{O}_{7-\delta}$ single crystals grown in BaZrO_3 crucibles have been studied. The melting of the flux line lattice is clearly demonstrated by the kink feature in the electrical resistivity $\rho(T)$. The characteristics of the $E(J)$ isotherms revealed a more complex picture of the vortex liquid to vortex solid phase transition. The experimental data provides evidence for the co-existence of a first order vortex-lattice melting transition and a continuous vortex-glass melting transition at a lower temperature in high purity twinned $\text{YBa}_2\text{Cu}_3\text{O}_{7-\delta}$ single crystal samples grown in BaZrO_3 crucibles. The correlation of temperature T and magnetic field H dependence of the electrical resistivity ρ and electric field versus current density E vs J isotherms, is consistent with a two-step phase transition from the normal to the superconducting state. Analysis of the data strongly indicates the vortex matter in the single crystal is inhomogeneous. This scenario is supported by the observation of a vortex-lattice melting at a temperature separating two vortex-glass states with *different* critical exponents $\nu(z - 1)$. In light of independently performed numerical simulations [Crabtree *et al.*, Physical Review B **61**, 1446 (2000)], the data support a scenario where the intermediate phase crosses over from a state where vortex lines in the twin boundaries are pinned and those within the bulk undergo driven plastic vortex flow, to a state where the vortex lines in and near the twin boundaries undergo driven disordered motion and those within the bulk move as an ordered lattice.

Table IV.1: Parameters determined from $E(J)$ and $\rho(T)$ for BaZrO₃ grown YBa₂Cu₃O_{7- δ} single crystals including the vortex-glass melting temperature T_g and the static and dynamic critical scaling exponents ν and z , the resistivity critical exponent, $s \equiv \nu(z - 1)$, and the vortex-glass coherence length at the critical region boundary, ξ^* .

$H(\text{kOe})$	T_M	$T_g _{E(J)}(\text{K})$	$\nu _{E(J)}$	$z _{E(J)}$	$T_g _{\rho}(\text{K})$	$s _{\rho}$	$s _{E(J)}$	$\xi^*(\text{\AA})$	$\Delta\xi^*(\text{\AA})$
1.0	—	91.7	0.36	10.0	—	—	3.2	—	—
2.0	—	—	—	—	91.4	3.29	—	—	—
3.0	—	—	—	—	91.0	3.27	—	—	—
4.0	—	—	—	—	90.9	3.14	—	—	—
5.0	—	90.6	0.36	6.25	90.6	2.97	1.9	11359	604
6.0	—	—	—	—	90.4	3.02	—	—	—
8.0	90.7	89.8	0.36	5.50	90.1	1.19	1.6	10832	570
10.0	90.3	89.4	0.36	4.87	89.5	1.24	1.4	9493	471
30.0	86.8	86.2	0.38	2.64	86.0	0.67	0.62	6521	432
50.0	83.7	83.3	0.38	2.64	83.3	0.64	0.62	6960	375
70.0	81.0	80.7	0.38	2.64	80.7	0.67	0.62	6803	363
90.0	78.2	78.0	0.38	2.64	78.0	0.77	0.62	6234	317

A portion of the text and data of this chapter is a reprint of the material as it appears in “Vortex-melting and vortex-glass transitions in a high purity twinned $\text{YBa}_2\text{Cu}_3\text{O}_{7-\delta}$ single crystal,” Phys. Rev. B **68**, 054523 (2003), B. J. Taylor, S. Li, M. B. Maple, and M. P. Maley. The dissertation author was the primary investigator and author of this article.

Bibliography

- [1] G. Blatter, M. V. Feigel'man, V. B. Geshkenbein, A. I. Larkin, and V. M. Vinokur, *Rev. Mod. Phys.* **66**, 1125 (1994).
- [2] H. Safar, P. L. Gammel, D. A. Huse, D. J. Bishop, W. C. Lee, J. Giapintzakis, and D. M. Ginsberg, *Phys. Rev. Lett.* **70**, 3800 (1993).
- [3] L. M. Paulius, W. -K. Kwok, R. J. Olsson, A. M. Petrean, V. Tobos, J. A. Fendrich, G. W. Crabtree, C. A. Burns, and S. Ferguson, *Phys. Rev. B* **61**, R11910 (2000).
- [4] M. Roulin, A. Junod, A. Erb, and E. Walker, *Phys. Rev. Lett.* **80**, 1722 (1998).
- [5] W. -K. Kwok, R. J. Olsson, G. Karapetrov, L. M. Paulius, W. G. Moulton, D. J. Hofman, and G. W. Crabtree, *Phys. Rev. Lett.* **84**, 3706 (2000).
- [6] H. Safar, P. L. Gammel, D. A. Huse, D. J. Bishop, J. P. Rice, and D. M. Ginsberg, *Phys. Rev. Lett.* **69**, 824 (1992).
- [7] A. Schilling, R. A. Fisher, N. E. Phillips, U. Welp, W. K. Kwok, and G. W. Crabtree, *Phys. Rev. Lett.* **78**, 4833 (1997).
- [8] N. -C. Yeh, W. Jiang, D. S. Reed, U. Kriplani, and F. Holtzberg, *Phys. Rev. B* **47**, 6146 (1993).
- [9] M. Charalambous, R. H. Koch, T. Masselink, T. Doany, C. Feild, and F. Holtzberg, *Phys. Rev. Lett.* **75**, 2578 (1995).
- [10] P. L. Gammel, L. F. Schneemeyer, and D. J. Bishop, *Phys. Rev. Lett.* **66**, 953 (1991).
- [11] G. W. Crabtree, W. -K. Kwok, L. M. Paulius, A. M. Petrean, R. J. Olsson, G. Karapetrov, V. Tobos, W. G. Moulton, *Physica C* **332**, 71 (2000).
- [12] A. Erb, E. Walker, J. -Y. Genoud, and R. Flükiger, *Physica C* **282**, 89 (1997).
- [13] J. -C. Grivel, Yu. Eltsev, M. Anderson, Ö. Rapp, A. Erb, E. Walker, R. Flükiger, *Physica C* **322**, 203 (1999).
- [14] T. K. Worthington, M. P. A. Fisher, D. A. Huse, J. Toner, A. D. Marwick, T. Zabel, C. A. Feild, and F. Holtzberg, *Phys. Rev. B* **46**, 11854 (1992).
- [15] A. E. Koshelev, and V. M. Vinokur, *Phys. Rev. Lett.* **73**, 3580 (1994).
- [16] A. Erb, E. Walker, and R. Flükiger, *Physica C* **245**, 245 (1995).
- [17] T. B. Lindemer, J. F. Hunley, J. E. Gates, A. L. Sutton, Jr., J. Brynastad, C. R. Hubbard, and P. K. Gallagher, *J. Am. Ceram. Soc.* **72** [10], 1775 (1989).

- [18] R. Liang, D. A. Bonn, and W. N. Hardy, *Physica C* **304**, 105 (1998).
- [19] J. Deak, M. McElfresh, J. R. Clem, Z. Hao, M. Konczykowski, R. Muenchausen, S. Foltyn, and R. Dye, *Phys. Rev. B* **47**, 8377 (1993).
- [20] D. S. Fisher, M. P. A. Fisher, and D. A. Huse, *Phys. Rev. B* **43**, 130 (1991).
- [21] S. A. Grigera, E. Morre, E. Osquiguil, C. Balseiro, G. Nieva, and F. de la Cruz, *Phys. Rev. Lett.* **81** 2348 (1998).
- [22] L. Hou, J. Deak, P. Metcalf, M. McElfresh, and G. Preosti, *Phys. Rev. B* **55** 11806 (1997).
- [23] J. T. Chayes, L. Chayes, D. S. Fisher, and T. Spencer, *Phys. Rev. Lett.* **57**, 2999 (1986).
- [24] A. B. Harris, *J. Phys. C* **7**, 1671 (1974).
- [25] G. W. Crabtree, D. O. Gunter, H. G. Kaper, A. E. Koshelev, G. K. Leaf, and V. M. Vinokur, *Phys. Rev. B* **61**, 1446 (2000).
- [26] D. Dominguez, *Phys. Rev. Lett.* **72** 3096 (1994).
- [27] A. I. Larkin, and Yu. N. Ovshnikov, *J. Low Temp. Phys.* **34**, 409 (1979).
- [28] D. G. Xenikos, T. R. Lemberger, L. Hou, M. W. McElfresh, *Physica C* **235-240** 2661 (1994).

V

Vortex glass and Bragg glass phases in MgB₂

V.A Introduction

The binary compound MgB₂ holds a unique place among superconducting materials. With a critical temperature of $T_c \approx 40$ K, this places it as an intermediary between the existing high-field superconductors used in modern applications, Nb-Ti ($T_c = 9$ K) and Nb₃Sn ($T_c = 18$ K), and the high-temperature cuprate superconductors YBa₂Cu₃O_{7- δ} ($T_c \sim 90$ K) and Bi₂Sr₂CaCu₂O₈ ($T_c \sim 90$ K). Furthermore, the unusual superconducting properties of MgB₂ come from the fact that it is a two-gap superconductor. The energy gaps are associated with distinct disconnected portions of the Fermi surface [1, 2, 3, 4], with the larger gap, $\Delta_\sigma \approx 7$ meV, arising from the in-plane σ antibonding p_{xy} orbitals of B, and the smaller gap, $\Delta_\pi \approx 2$ meV, comprised of the out-of-plane π bonding and antibonding p_z orbitals of B [5]. MgB₂ has superior mechanical properties compared to high temperature superconducting cuprates due to its much simpler crystal structure. The grain boundaries, which remain the major obstacle impeding the application of high- T_c materials, do not appear to be a limiting factor on the critical current density of MgB₂ [6]. Since its discovery in 2001 [7], the considerable quantity of research

devoted to MgB_2 has produced a rapidly developing picture of the material in its normal and superconducting states. An important issue in the development of MgB_2 for use in technological applications is the critical current density, which is directly related to the nature of vortex pinning and vortex dynamics in the system. In addition to the industrial usefulness of such knowledge, a study of the physics of the vortex matter states of MgB_2 over the magnetic field – temperature ($H - T$) phase diagram provides further insight into the fundamental properties of this unique type-II superconductor.

In type-II superconductors with sufficient disorder, the superconducting region below the upper critical field $H_{c2}(T)$ is further divided by a vortex-glass transition line $H_g(T)$, which separates the dissipative vortex-liquid (VL) phase at higher temperatures, and the truly superconducting vortex-glass (VG) phase with a finite critical current density at lower temperatures [8]. Vortex dynamics in a high quality bulk MgB_2 sample was investigated via measurements of electric field vs current density isotherms, $E(J)$, over a range of applied magnetic field. Analysis of the $E(J)$ data was performed within the context of the critical scaling model of a vortex glass [9, 10, 11]. In this chapter, analysis of $E(J)$ isotherms, the critical current density, J_c , and its gradient ∇J_c , and further calculations based upon the vortex glass critical scaling model are presented. This work provided the first evidence for the existence of the Bragg glass vortex phase along the low field portion ($H \lesssim 8$ kOe) of the vortex glass melting line in this compound. The interpretation of the data as an indication of the Bragg glass state was later confirmed by independent reports from other groups based on magnetization measurements on MgB_2 single crystals [12, 13, 14]. Neutron scattering measurements have since revealed that the vortex lattice undergoes a structural realignment at a magnetic field value $5 \text{ kOe} < H < 9 \text{ kOe}$, which is attributed to the suppression of the smaller superconducting gap, Δ_π [15].

V.B Experimental Details

High quality MgB_2 bulk samples were produced from commercial MgB_2 powder (Alfa Aesar) by means of dense material cooling under pressure (DMCUP), a technique based on hot isostatic pressing (HIPing). Initial characterization of the HIPed samples by scanning electron microscopy (SEM) was unable to distinguish grain boundaries, possibly as a result of the rapid cooling of the molten material under pressure [16]. The HIPed MgB_2 displayed superior superconducting properties as well, including a very high critical current density J_c , and a relatively low rate of decrease of J_c with increasing magnetic field [17]. The values of J_c obtained for the HIPed material are about an order of magnitude larger than those achieved on dense Fe clad MgB_2 wires prepared by the powder in tube technique [18].

The superconducting transition temperature T_c was 38.5 K with a transition width ΔT_c of 0.75 K, determined from electrical resistivity $\rho(T)$ measurements. Here, T_c is defined as the temperature of the 50% value and ΔT_c as the difference in temperatures of the 10% and 90% values of the $\rho(T)$ superconducting transition curve. Magnetization measurements were made with a commercial Quantum Design SQUID magnetometer. Magnetization M vs applied field H hysteresis loops were taken at temperatures between 10 and 38 K and in applied fields between 0 and 50 kOe. Electrical transport measurements were made using the standard four-probe technique in a commercial Quantum Design Physical Property Measurement System with a maximum field of 90 kOe. The dc current was applied using a Keithley K220 current source, and the sample voltage was measured with a Keithley K2182 nanovoltmeter. To study $E(J)$ characteristics, a thin rectangular strip was polished to have final dimensions of $\sim 2.8 \times 1.2 \times 0.12$ mm. For the measurements of the $E(J)$ isotherms, the sample was first cooled to the lowest temperature in zero field, the magnetic field was applied, and the $E(J)$ isotherms were taken in increasing temperature increments [19]. The temperature drift in the $E(J)$ measurements was less than 0.01 K.

V.C Results and Discussion

Two sets of $E(J)$ isotherms for the HIPed MgB_2 are shown in Fig. V.1, on a $\log E$ vs $\log J$ plot. As shown in Fig. V.1(a), from top to bottom with decreasing T and steps of $\Delta T = 0.05$ K, the $E(J)$ isotherms at $H = 2$ kOe consist of three distinguishable regimes: ohmic behavior at the highest temperatures, ohmic (at small J) to power law dependence (at large J) at intermediate temperatures, and exponential dependence with a negative downward curvature at the lowest temperatures. This is consistent with results on MgB_2 thin films [20] and high- T_c cuprate superconductors [11]. The $E(J)$ isotherms at $H = 90$ kOe which range from 15.0 K to 19.8 K with 0.4 K increments (Fig. V.1(b)), exhibit similar characteristics compared to the low field data, except that the critical region is noticeably larger. The negative curvature of $E(J)$ at low temperature is a clear indication of the sample being in a true superconducting state (vortex-glass), while the ohmic $E(J)$ curve suggests a vortex-liquid state with dissipation upon application of transport current. The $E(J)$ isotherm with a single power law dependence over the whole current range separates these two phases; this isotherm temperature identifies the vortex-glass transition temperature T_g [9, 10].

$E(J)$ isotherm sets shown in Fig. V.1 were scaled using the ansatz of the Fisher-Fisher-Huse (FFH) vortex-glass transition model [8]. The FFH scaling functions of the electric field and current density are $(E/J)/|1 - T/T_g|^{-\nu(z-1)}$ and $(J/T)|1 - T/T_g|^{-2\nu}$, where ν and z are the static and dynamic scaling exponents, respectively. If the melting of the solid vortex ensemble is that of a vortex glass, then, all isotherms will collapse onto two universal curves corresponding to critical behavior of the vortex-liquid phase above T_g and the vortex-glass phase below T_g . The glass transition temperature T_g was first determined from the critical isotherm which conforms to a power law $E \sim J^{(z+1)/2}$. This curve was identified by plotting the power of the $E(J)$ curves, $d\ln E/d\ln J$ vs J , and choosing the curve with a $d\ln E/d\ln J$ value that is constant in J [19]. For $H = 2$ kOe, the best curve thus

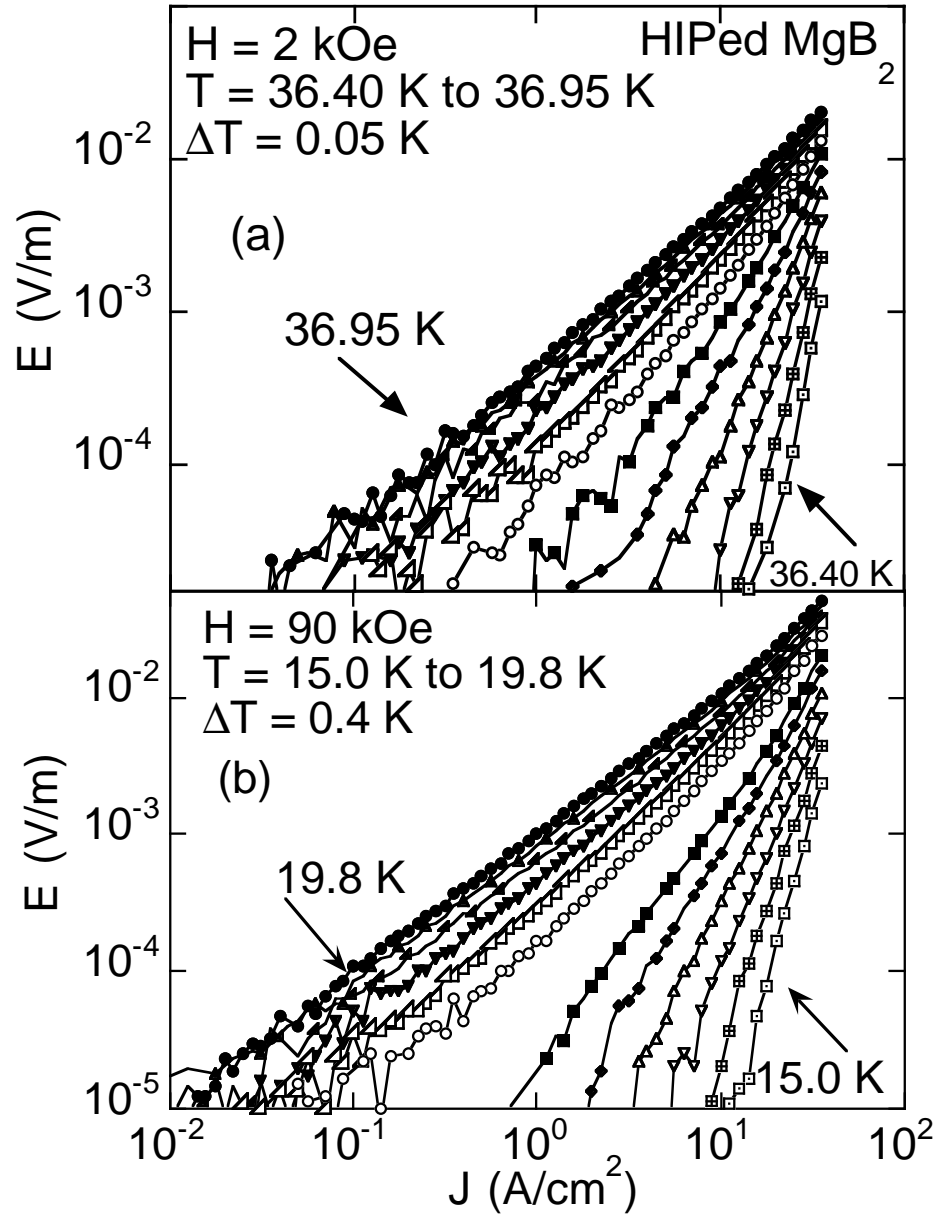


Figure V.1: Isotherm sets of electric field E vs transport current density J of HIPed Alfa Aesar MgB₂ at (a) $H = 2$ kOe, with increasing temperature from the bottom ($T = 36.40$ K) to the top ($T = 36.95$ K) of the figure, in 0.05 K increments; and (b) $H = 90$ kOe, from $T = 15.0$ K (bottom) to $T = 19.8$ K (top), in 0.4 K increments.

identified gives the glass temperature $T_g = 36.64 \pm 0.02$ K and dynamic exponent $z \sim 3.1 \pm 0.1$. The small uncertainty in the values of T_g and z is due to the discrete temperature increments in the $E(J)$ isotherm sets collected.

The T_g and z values obtained through the procedure described above are used to start the scaling of $E(J)$ isotherm sets. The scaling functions corresponding to $E(J)$ data at $H = 2$ kOe and $H = 90$ kOe are shown in Fig. V.2. To scale a particular set of $E(J)$ data, the static exponent ν was varied with T_g and z fixed to obtain the best collapse possible. Then, the values of T_g and z were varied slightly and in a correlated manner to further improve the scaling. This variation is justified due to the small error in the determination of T_g and z . As listed in Table IV.1, the scaling process yields $\nu \sim 0.9$ consistently in the field range from 8 kOe to 90 kOe, while giving a smaller value of $\nu \sim 0.6$ below 8 kOe. The z values were ~ 3.1 for $2 \text{ kOe} \leq H \leq 10 \text{ kOe}$ and jump to ~ 3.4 at $H > 10 \text{ kOe}$. The error margins in the ν and z values were estimated to be 0.05 and 0.1, respectively. The method used here for determining the error for z is based on the aforementioned $d \ln E / d \ln J$ plot. A range of values for $(z+1)/2$ was established about the isotherm displaying the constant power law exponent. This range was chosen so that it encompasses no data from adjacent isotherms. The error for ν follows by observing the best scaling of the data and noting the window over which a deviation from this is small. As a consistency check, $\nu(z-1)$ values were also determined from $\rho(T)$ data and agree well with those obtained from $E(J)$ scaling. The current used in the $\rho(T)$ scaling method was in the range of 2 mA to 10 mA so as to remain in the scaling regime. These values are summarized in Table IV.1.

The values of the critical exponents of HIPed MgB_2 at low fields are close to the exponents of $\nu \sim \frac{2}{3}$ and $z \sim 3.0$ reported by Yeh *et al.*, for lightly twinned, proton irradiated $\text{YBa}_2\text{Cu}_3\text{O}_{7-\delta}$ single crystals [11], but quite different from the values of $\nu \sim 1$ and $z \sim 4.5$ reported for MgB_2 thin films [20]. At high fields, $\nu \sim 0.9$ is closer to that of MgB_2 thin films ($\nu \sim 1.0$), but $z \sim 3.4$ is still much smaller in comparison to $z \sim 4.5$ for MgB_2 thin films. These differences are thought

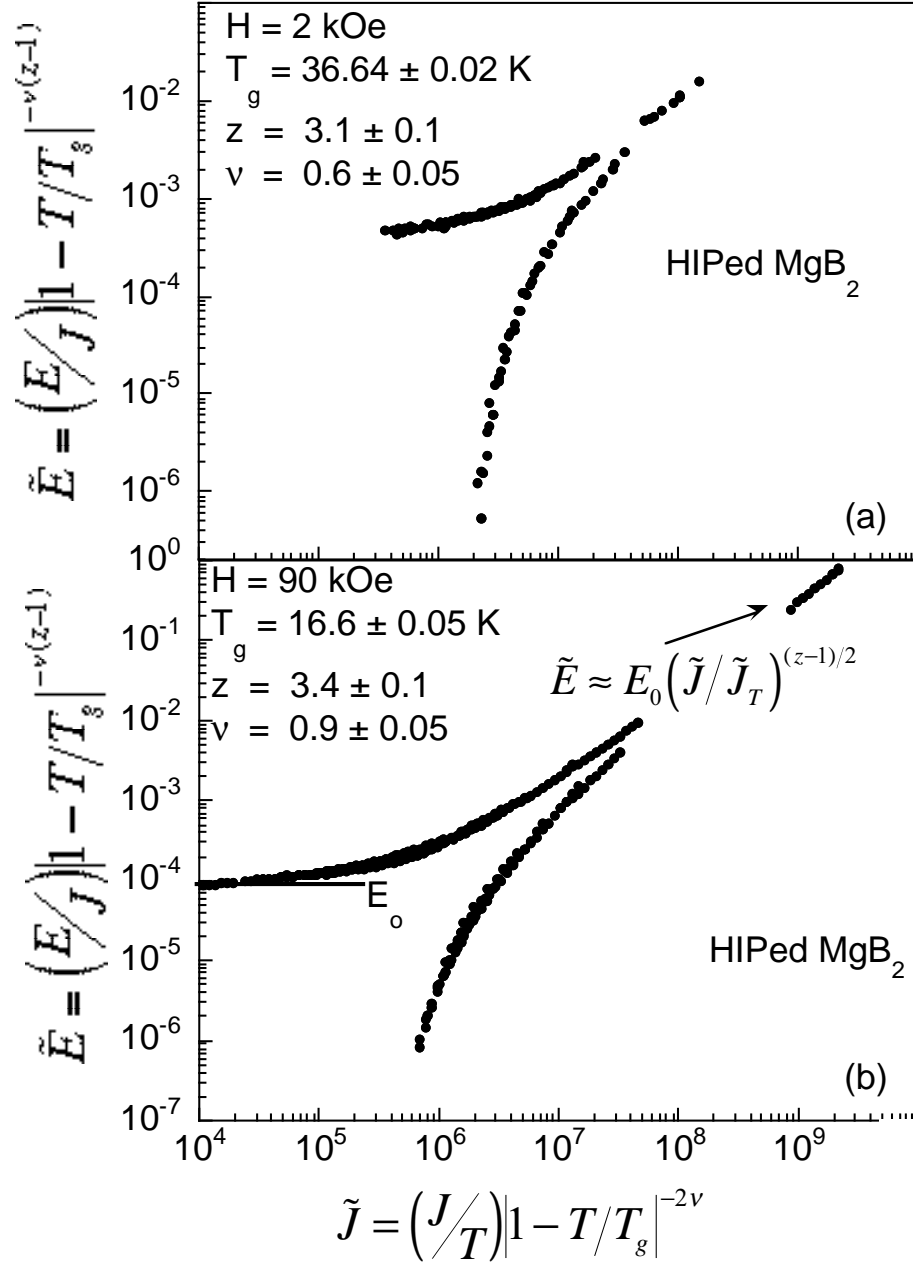


Figure V.2: Vortex-glass scaling functions corresponding to the $E - J$ isotherm sets at $H = 2$ kOe and $H = 90$ kOe shown in Figure 1. For $T \rightarrow T_g$, $\tilde{E} \approx \tilde{E}_0 (\tilde{J}/\tilde{J}_T)^{(z-1)/2}$ as indicated in (b).

to reflect a weak point defect dominated microstructure of the HIPed MgB_2 samples as a result of the DMCUP process, in contrast to MgB_2 thin films prepared by pulsed laser deposition, which would be plagued by thin film topological defects, i.e., dislocations, faults, etc. The comparison to the results for the $\text{YBa}_2\text{Cu}_3\text{O}_{7-\delta}$ films is made so as to emphasize the dominance of point defects and the resulting exponents obtained experimentally. Magnetization measurements [21, 22, 23], on untwinned YBCO single crystals, both with and without electron irradiation, have revealed a Bragg-glass state over a large region of the phase diagram. The boundary of this region includes the vortex-glass to vortex-liquid transition in the range of H and T consistent with that examined by Yeh *et.al.* The different values of the critical exponents for low and high fields obtained from the above scaling analysis indicate that the dynamics of vortices in these two regions along the melting transition are different. This then points to two different vortex solid phases with boundaries along the vortex-solid to vortex-liquid transition.

The zero temperature vortex-glass correlation length $\xi(T = 0) \equiv \xi_0$ can be calculated from the preceding scaling of E and J for each applied field H . Following the assumption, $\tilde{E} \approx \tilde{E}_0 (\tilde{J}/\tilde{J}_T)^{(z-1)/2}$ for $T \approx T_g$ [11], the current density, \tilde{J}_T , is directly obtained from the scaled $\tilde{E} - \tilde{J}$ isotherm for $T \approx T_g$ ($\tilde{E}[T \approx T_g]$ vs $\tilde{J}[T \approx T_g]$). \tilde{J}_T is the scaled crossover current density separating the current and temperature dominated vortex depinning regimes. \tilde{E}_0 is a temperature independent constant obtained in the limit $(\tilde{J}/\tilde{J}_T)^{(z-1)/2} \rightarrow 0$, as indicated in Fig. V.2(b). \tilde{J}_T can be calculated from any of the scaled pairs $(\tilde{E}_i, \tilde{J}_i)$ on the $T \approx T_g$ line. Using the relation $\tilde{J}_T \approx k_B/(\Phi_0 \xi_0^2)$ in the critical region [11] (see Fig. V.2(b)), a value for $\xi_0(H)$ can be found. As seen in Fig. V.2, some of the data points deviate from a smooth line fit. In order to obtain the best *rms* value of $\xi_0(H)$, some of the scaled data points $(\tilde{E}_i, \tilde{J}_i)$ were removed from the $T \approx T_g$ line under the following criteria. A power law curve is fitted to the data (satisfying $\tilde{E} \approx \tilde{E}_0 (\tilde{J}/\tilde{J}_T)^{(z-1)/2}$). The data points were selectively removed from the data set until the fit agreed well with the value for z obtained earlier (via $d \ln E / d \ln J$ vs J and the subsequent

scaling of the $E-J$ isotherms) and the regression of the fit was the best possible. \tilde{J}_T was calculated separately for each remaining scaled pair. $\xi_0(H)$ was then calculated for each \tilde{J}_T , making use of the above stated relation. An *rms* value of $\xi_0(H)$ was arrived at from the above calculations. Two different methods were used to obtain the error $\Delta\xi_0$ for each of the $\xi_0(H)$ values. The first treatment follows standard statistical analysis of error. The values of $\Delta\xi_0$ obtained by this method were found to vary by amounts ranging from 0.6 Å to 150 Å for the set of fields examined. The dominating terms of the error ΔJ_T are those of ΔE_i and ΔJ_i , the size of which is primarily dependent on how close the isotherm temperature data are to the determined value of T_g . As $T \rightarrow T_g$, these values become very large. It was found that the size of the error can be manipulated by nearly two orders of magnitude by simply adjusting T_g by a few hundredths of a degree kelvin away from the scaled isotherm temperature. This change of T_g is within the margin of error ΔT_g and is therefore allowable. This method provides an unsatisfactory determination of $\Delta\xi_0$. The values of $\Delta\xi_0$ reported here have been obtained by a series of variations of the parameters T_g , z and ν . The critical current density \tilde{J}_T was again calculated as above with each parameter independently evaluated at $T_g \pm \Delta T_g$, etc. The correlation length was calculated from each series of J_T values, and then the set of ξ_0 values was used to obtain an *rms* value of $\xi_0(H)$ and the standard deviation $\Delta\xi_0(H)$. These values are considered more reliable as an estimate of the error.

The calculated values of ξ_0 for each of the fields examined are shown in Fig. V.3. The values of ξ_0 are fairly constant at ~ 340 Å for fields below 8 kOe. At this field the size of ξ_0 suddenly decreases to a much smaller value. For $8 \text{ kOe} \leq H \leq 90 \text{ kOe}$, ξ_0 increases exponentially with H from ~ 100 Å to ~ 800 Å. This apparent discontinuity in ξ_0 at $H \approx 8 \text{ kOe}$ is accompanied by the discontinuous jump of the value of the static scaling exponent ν from 0.6 to 0.9. These results imply that translational order of the vortex-lattice is significantly reduced upon crossing over from low to high field regimes. Such behavior

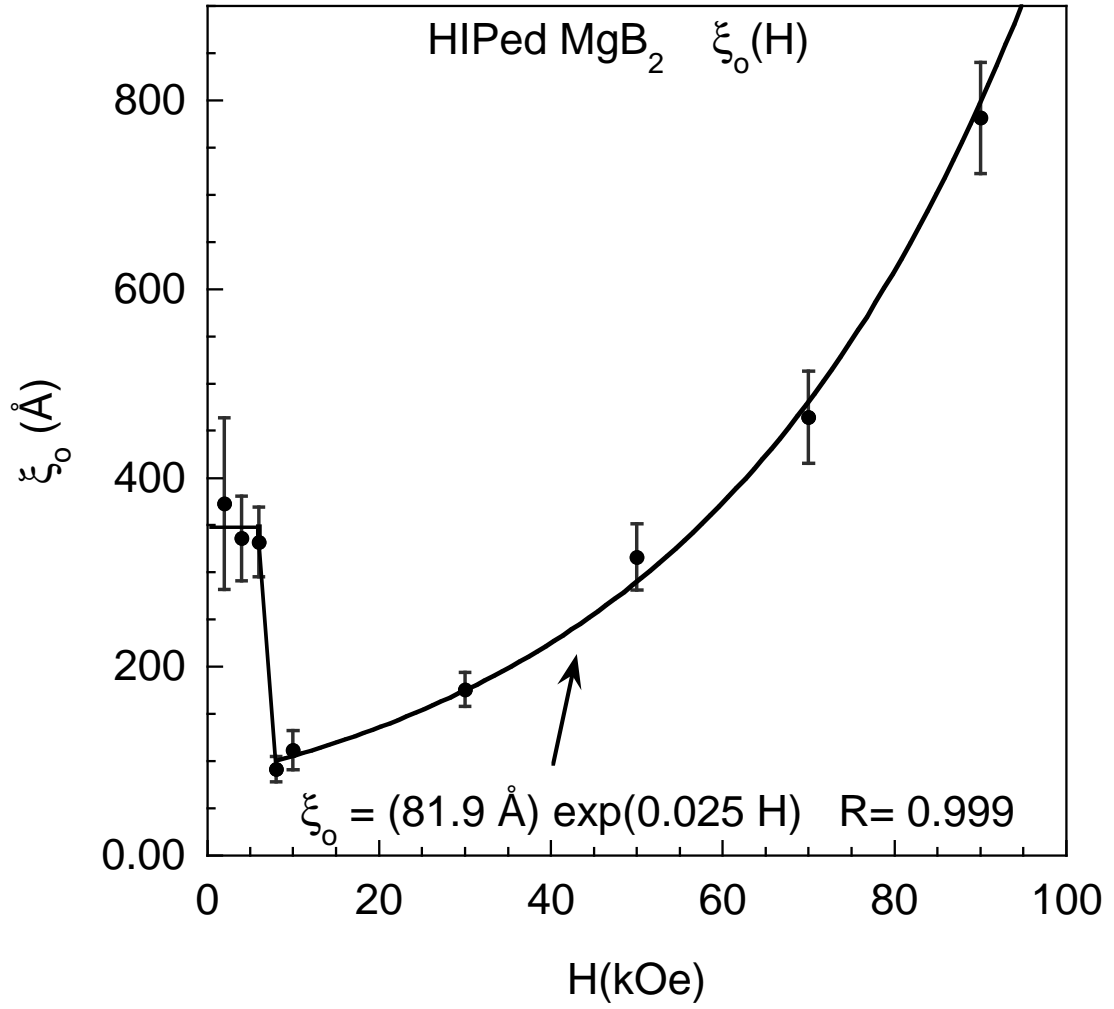


Figure V.3: Zero-field vortex-glass coherence length in HIPed MgB_2 , with estimated error. $\xi_0 \sim 340$ Å for $0.2 \text{ T} \leq H < 0.8 \text{ T}$. ξ_0 increases exponentially from ~ 100 Å to ~ 800 Å for $0.8 \text{ T} \leq H \leq 9.0 \text{ T}$.

is consistent with a order-disorder transition from a Bragg-glass state for $H < 8$ kOe to a vortex-glass at higher fields $H \gtrsim 8$ kOe. Bragg-glass theory predicts a rapid increase of topological defects when disorder or the applied field reaches a threshold, resulting in the aforementioned transition [24]. Long range order is rapidly destroyed upon crossing this threshold, resulting in the sudden decrease in the value of ξ_0 at $H \approx 8$ kOe.

Further evidence supporting a Bragg-glass scenario in MgB_2 is found in observation of the size of the critical region ΔT_{vg} , shown in Fig. V.4. The extent of the critical region is determined from the critical scaling relation of the resistivity, $\rho(T) \sim (T-T_g)^{\nu(z-1)}$ (ref. [8]) by plotting $1/[d(\ln\rho)/dT]$ vs T . The region ΔT_{vg} is the temperature interval over which the plot is linear, intercepting the T axis at T_g with slope $[\nu(z-1)]^{-1}$. On the basis of its relatively small value, the full width of the critical scaling region $2\Delta T_{vg}$ appears to be weakly first order with $2\Delta T_{vg} \approx 0.4$ K for $H \leq 8$ kOe. The full width remains constant at $2\Delta T_{vg} \approx 0.4$ K for $2 \text{ kOe} \leq H \leq 8 \text{ kOe}$, then increases to $2\Delta T_{vg} \approx 0.7$ K at $H = 10$ kOe from which it increases logarithmically for higher fields to a value of 4.4 K for $H = 90$ kOe.

It is of interest to compare the above results to work by Kim *et al.*, [25] which preceded this study, in which a bulk polycrystalline sample of MgB_2 prepared at high pressure and temperature was analyzed via $E - J$ scaling. Two main differences in sample preparation between their work and that presented herein are the pressures used and the order of application of heat and pressure. Their sample was prepared via sintering at 950°C after application of 3 GPa pressure. SEM pictures revealed resolvable grains of $\sim 5\text{-}10 \mu\text{m}$ in length. Our sample was formed by first heating to 850°C , applying 200 MPa pressure, then raising the temperature to 1000°C , followed by cooling below 200°C before removal of the pressure. SEM pictures were unable to resolve grain boundaries at the μm scale in the sample used in this study. Kim *et al.* determined the critical exponents to be universal with $z = 2.33$ and $\nu = 0.5$, which disagrees with the results found here.

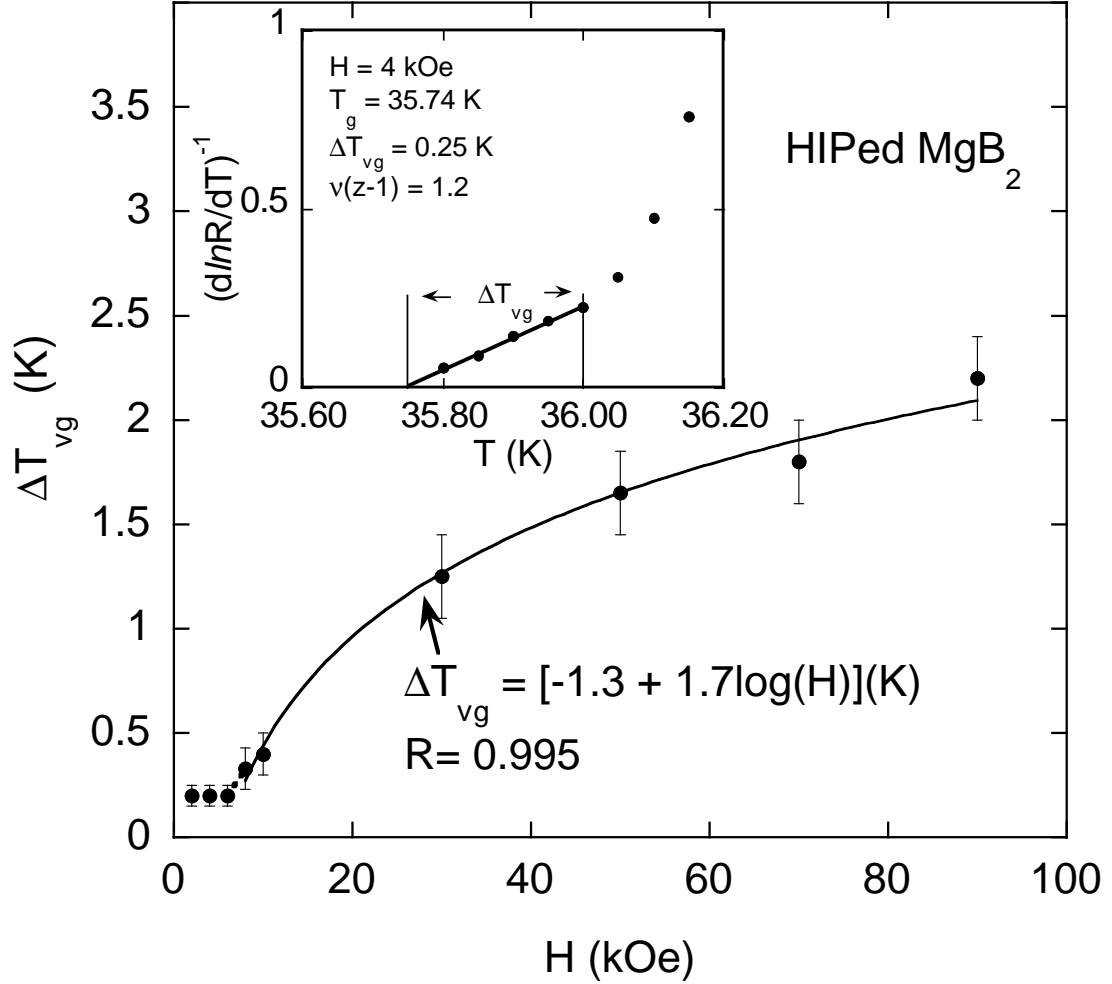


Figure V.4: Temperature width of the critical region of vortex glass scaling in HIPed MgB_2 . T_g and ΔT_g are determined for each field by the region over which $1/[d(\ln(R))/dT]$ is linear in T . For $H = 4$ kOe (inset) $1/[d(\ln(R))/dT] = -31.1 + 0.87(T)$. Note the jump in the value of ΔT_g at $H \approx 0.8$ T. The transition width is nearly constant for $H \leq 0.8$ T, then increases logarithmically with field.

Their phase diagram, then, includes only a vortex glass phase. A possible explanation for this discrepancy may be related to the much higher grain connectivity of our samples, causing them to behave more like single crystal specimens. However, it is notable that they reported that $E - J$ scaling was poor below $H = 1$ T, the same region we have interpreted as being in the Bragg-glass state.

The Bean critical state model was applied to magnetization $M(H, T)$ data determining the critical current density $J_c(H, T)$ of the MgB_2 sample. The results are shown in Fig. V.5. Constant current lines are shown projected onto the low field - high temperature region of the $H - T$ phase diagram in Fig. V.6. The irreversibility line $H_{irr}(T)$ is defined by the locus of points in the $H - T$ plane where $\Delta M = 0$ since J_c is proportional to ΔM in the Bean model. $H_{irr}(T)$ is also expected to coincide with the vortex glass line $T_g(H)$ which demarcates the onset of vortex pinning and a finite critical current. It should be stressed at this point that magnetization measurements have a resolution limit which often results in a disagreement of $H_{irr}(T)$ with $T_g(H)$ with the former lying at lower temperature. This leads to the treatment here of $H_{irr}(T)$ as a boundary where the critical current drops below a measurable noise window upon crossing to higher temperature. However, J_c remains finite (but small) up to the vortex glass line $T_g(H)$. With this in mind the $H - T$ phase diagram is shown in Fig. V.7 with $H_{irr}(T)$ denoted as $J_c \sim 0$. The line of finite measurable J_c approaches $T_g(H)$ and the associated critical region gradually from higher field (lower temperature) but then abruptly crosses *into* the critical scaling region at $H \approx 7$ kOe, $T \approx 34.6$ K, after which it coincides with $T_g(H)$. This region where *measurable* J_c extends to $T_g(H)$ displays a short tail in J_c (Fig. V.8). The larger current end of this tail coincides with the lower boundary of the $T_g(H)$ critical scaling region. J_c in the critical region is observed to follow a power law behavior $J_c \sim |H - H_g|^n$ with $n \approx 1.0 - 1.3$. Making use of the scaling form of $J_c \sim |H - H_g|^{2\nu}$ gives $\nu \approx 0.5 - 0.65$. These values of ν are consistent with those determined from $E(J)$ scaling for $H \lesssim 8$ kOe. The sections of the critical scaling region separated by where measurable J_c

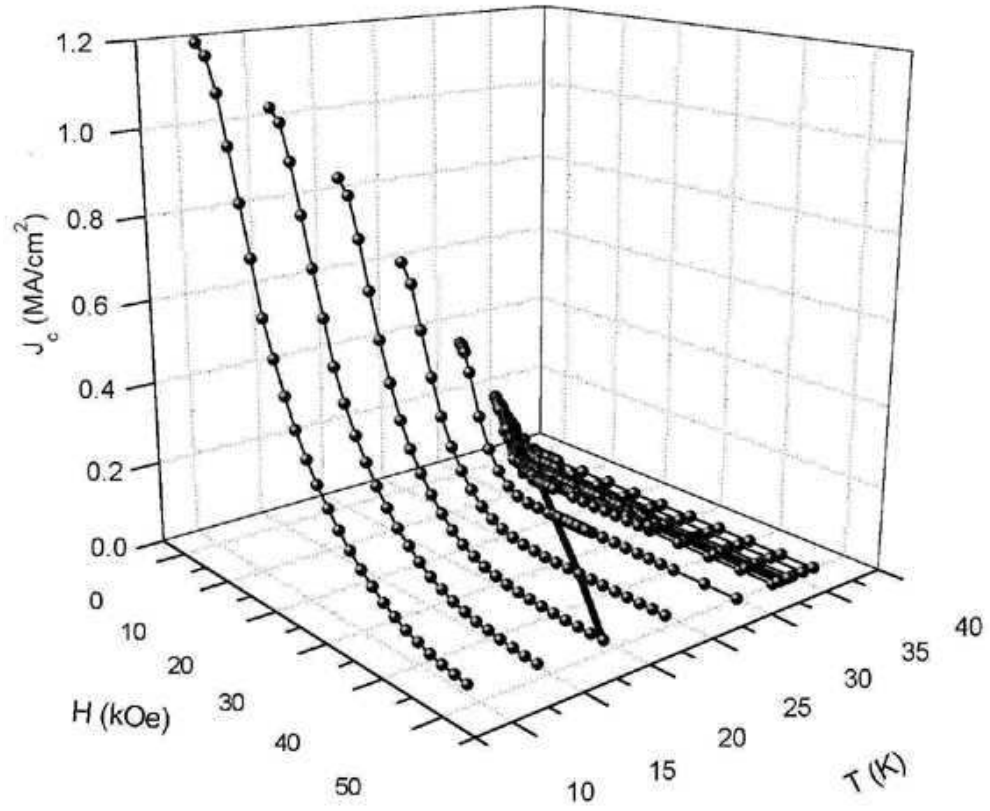


Figure V.5: Three dimensional plots of the critical current density vs magnetic field H and temperature T . (a) $J_c(H, T)$ over the full range of H and T values studied. The solid line indicates where $J_c \sim 0$.

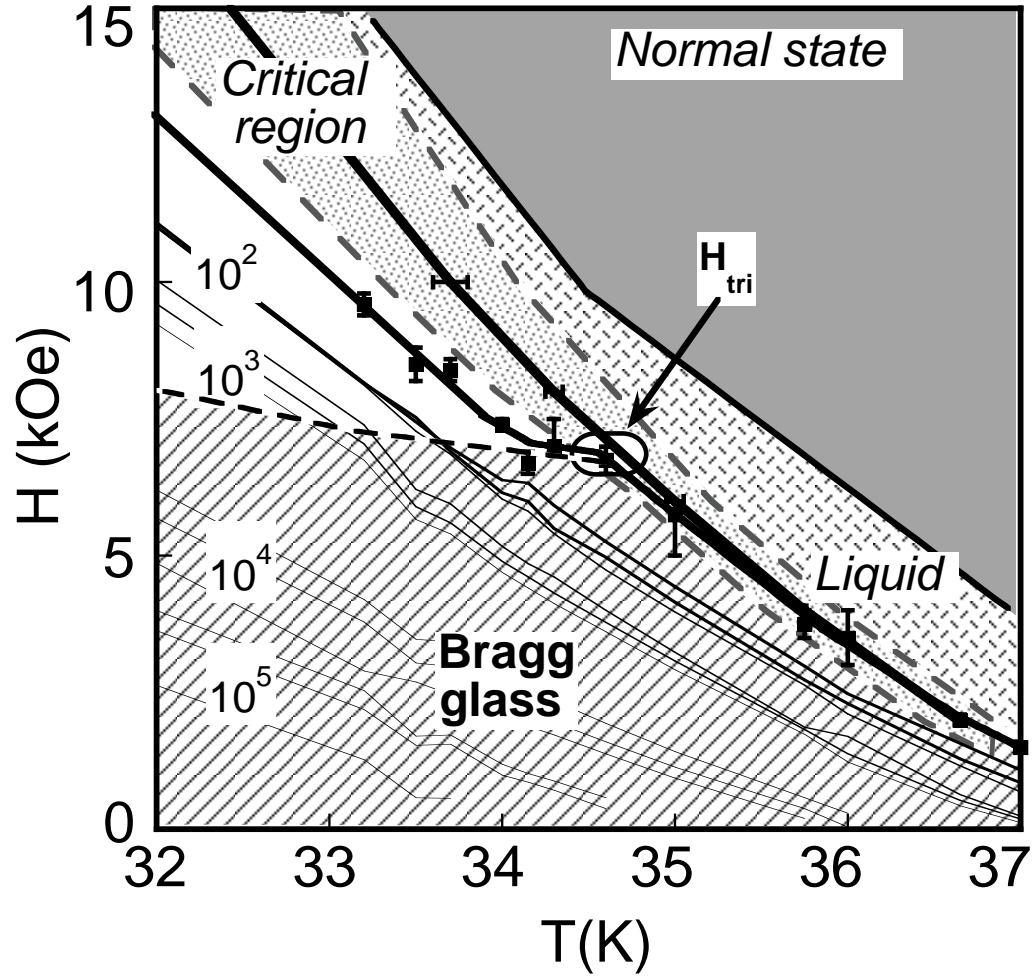


Figure V.6: Lines of constant J_c projected onto the low field, high temperature portion of the $H - T$ plane, demonstrating the steep gradient of the critical current density. Also indicated is the possible location of the tri-critical point, H_{tri} , corresponding to the $H - T$ coordinate on the $T_g(H)$ line separating the low field and high field regions where J_c is finite and immeasurable, respectively.

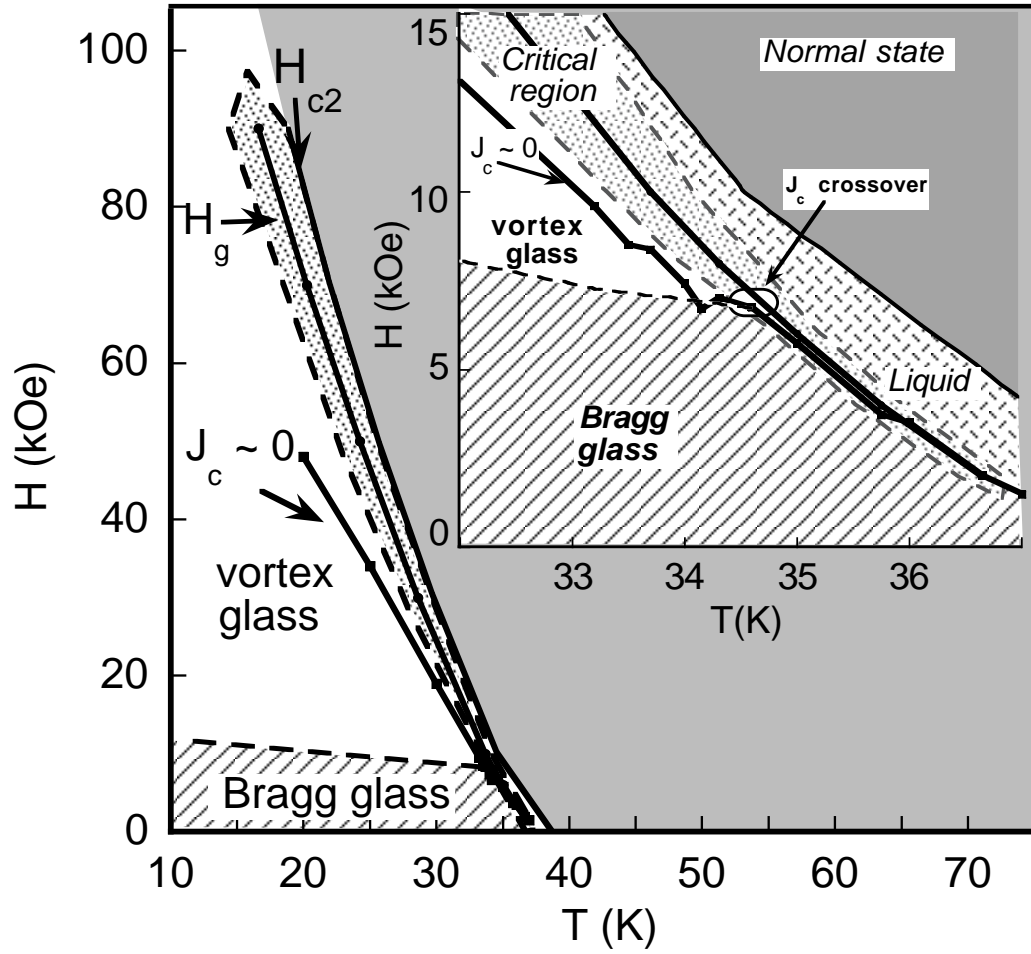


Figure V.7: Magnetic field vs temperature phase diagram of HIPed MgB_2 , with the vortex-glass transition line $H_g(T)$ lying below the upper critical field $H_{c2}(T)$ with the critical scaling region indicated. The line $J_c \sim 0$ denotes the boundary at which J_c is no longer detectable by magnetization methods. $J_c \sim 0$ is equivalent to $H_{irr}(T)$. Inset: Enlargement of low field - high temperature region indicating possible location of the tri-critical point (H_{tri}, T_{tri}) corresponding to the $H - T$ coordinate on the $T_g(H)$ line separating the low field and high field regions where J_c is finite and immeasurable, respectively.

crosses are also distinguished by a change from a weakly first order width (~ 0.4 K) to one which grows logarithmically to ~ 4.4 K (Fig. V.4), extending the critical region boundary ($T_g \leq T \leq T_c$) out towards the normal state boundary H_{c2} . The mean field $H_{c2}(T)$ curve was extracted from $\rho(T, H)$ data, and the magnetic irreversibility line $H_{irr}(T)$ was determined from magnetization vs field $M(H)$ hysteresis loops. The vortex-glass transition line $H_g(T)$ was obtained from scaling of the $E(J)$ isotherms as described above.

By considering all of the above results together, the analysis is consistent with the existence of a well ordered Bragg glass state at low fields along the melting line transition which gives way to a disordered vortex glass state at higher fields. It follows then that a tri-critical point exists along the melting line transition with a field value of $H_{tri} \lesssim 8$ kOe. At least two other groups reached the same conclusion in later studies with more direct methods on single crystal samples of MgB_2 . Both groups reported a peak effect which they interpreted as the boundary between the Bragg-glass and vortex-glass phases. The peak effect was observed via magnetic induction measurements by Pissas et al., [12] and torque magnetometry by Puzniak et al. [13, 14]. The existence of a tri-critical point on the vortex-glass to vortex-liquid line at $H \approx 7$ kOe, has been verified by neutron scattering experiments which reveal a change of the vortex lattice alignment with the underlying crystalline lattice as the smaller superconducting gap, Δ_π , is suppressed at a field between 5 kOe to 9 kOe [15]. Even though the study presented in this chapter is not conclusive on its own, the independent confirmation of the conclusions reached here demonstrates well that useful information about the host material can be extracted from a careful analysis of vortex critical dynamic behavior.

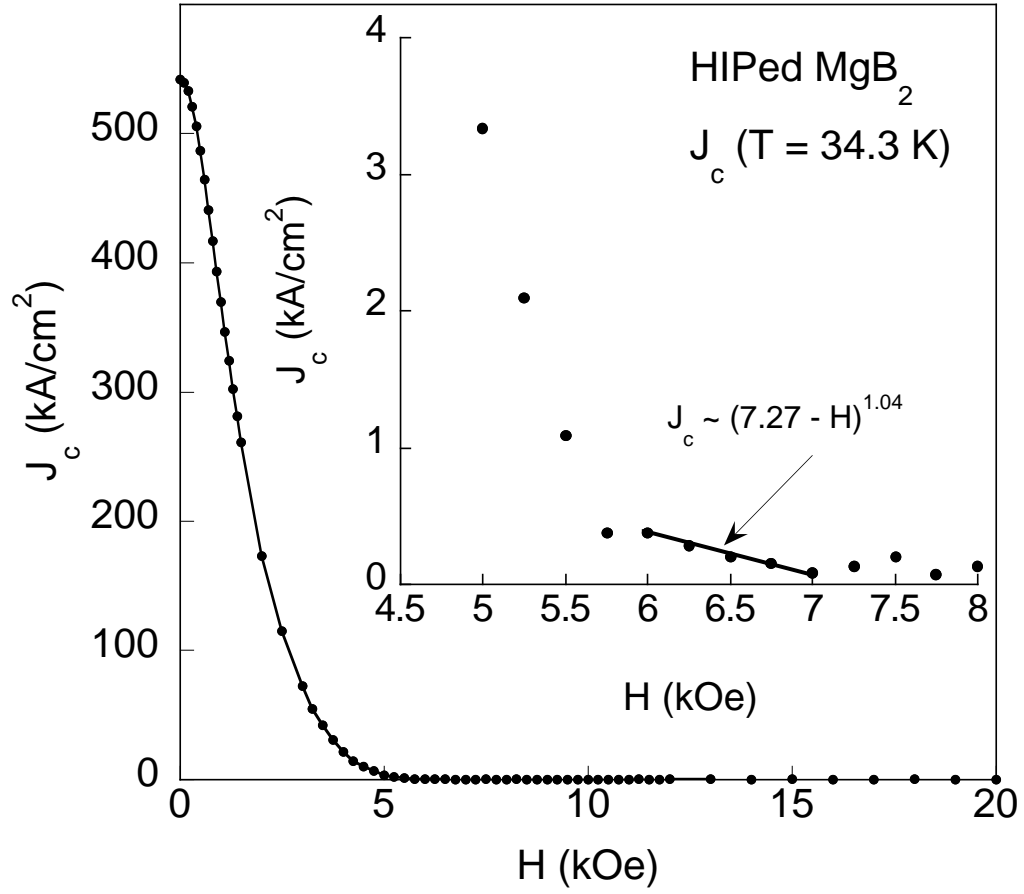


Figure V.8: Critical current density J_c vs magnetic field H at $T = 34.3 \text{ K}$. $J_c(H)$, which is measurable into the critical region via magnetization, displays a small tail in this region. $J_c(H)$ follows a power law, $J_c \sim |H - H_g|^{2\nu}$, with $\nu \sim 0.5 - 0.65$.

V.D Summary

In summary, the vortex-glass transition and critical current density characteristics of HIPed MgB₂ bulk specimens have been studied via electrical transport and magnetization measurements. The critical region is found to be qualitatively separated into low and high field regimes by J_c characteristics and by the size of the critical scaling regions. At low fields, $H \leq 7$ kOe, J_c is measurable via magnetization into the weakly first order critical region. For $H \geq 7$ kOe, J_c is not detectable (although certainly finite) in the critical region which is definitely second order. $E(J)$ scaling results in critical exponents ν and z which are different in low and high fields, changing from $\sim (0.6, 3.1)$ to $\sim (0.9, 3.4)$ between 6 kOe and 8 kOe, indicating a change of vortex dynamics along the melting transition line. The values of the scaling exponents are supported by additional scaling of $\rho(T)$ and J_c . The experimental data and subsequent analysis of the vortex critical dynamic behavior presented here provided the first evidence for the possibility of a Bragg glass phase in a bulk MgB₂ sample. This conclusion has since been verified by magnetization measurements and neutron scattering experiments.

Table V.1: Parameters determined from scaling analysis of $E(J)$ and $\rho(T)$ for HIPed MgB₂ including the vortex-glass melting temperature T_g , the static and dynamic critical scaling exponents ν and z , and the resistivity critical exponent, $s \equiv \nu(z - 1)$.

$H(\text{kOe})$	$T_g _{E(J)}(\text{K})$	$\nu _{E(J)}$	$z _{E(J)}$	$T_g _{\rho}(\text{K})$	$s _{\rho}$	$s _{E(J)}$	$\xi_0(\text{\AA})$	$\Delta\xi_0(\text{\AA})$
2.0	36.64	0.6	3.1	36.6	1.3	1.26	373	91.0
4.0	35.75	0.6	3.1	35.7	1.2	1.26	336	45
6.0	35.00	0.65	3.1	34.9	1.4	1.36	332	37
8.0	34.30	0.9	3.1	34.2	2.0	1.89	91.4	13.6
10.0	33.70	0.9	3.1	33.5	2.0	1.89	111	20.7
30.0	28.60	0.9	3.4	28.5	2.1	2.16	176	17.9
50.0	24.25	0.9	3.4	24.1	2.1	2.16	316	35.0
70.0	20.25	0.9	3.4	19.6	2.1	2.16	464	48.7
90.0	16.60	0.9	3.4	16.0	2.2	2.16	782	59.0

A portion of the text and data of this chapter is a reprint of the material as it appears in “Vortex- and Bragg-glass phases in bulk MgB_2 ,” *Physica C* **387**, 131 (2003), M. B. Maple, B. J. Taylor, S. Li, N. A. Frederick, V. F. Nesterenko, and S. S. Indrakanti; and “Mixed-state flux dynamics in bulk MgB_2 ,” *Physica C* **382**, 177 (2002), S. Li, B. J. Taylor, N. A. Frederick, M. B. Maple, V. F. Nesterenko, and S. S. Indrakanti. The dissertation author was the secondary investigator and author of these articles.

Bibliography

- [1] A. Y. Liu, I. I. Mazin, and J. Kortus, Phys. Rev. Lett. **87**, 087005 (2002).
- [2] H. J. Choi, D. Roundy, H. Sun, M. L. Cohen, and S. G. Louie, Nature (London) **418**, 758 (2002).
- [3] M. Iavarone, G. Karapetrov, A. E. Koshelev, W. K. Kwok, G. W. Crabtree, D. G. Hinks, W. N. Kang, E. -M. Choi, Hyun Jung Kim, H. -J. Kim, and S. I. Lee, Phys. Rev. Lett. **89**, 187002 (2002).
- [4] R. S. Gonnelli, D. Daghero, G. A. Ummarino, V. A. Stepanov, J. Jun, S. M. Kazakov, and J. Karpinski, Phys. Rev. Lett. **89**, 247004 (2002).
- [5] A. Gurevich, S. Patnaik, V. Braccini, K. H. Kim, C. Mielke, X. Song, L. D. Cooley, S. D. Bu, D. M. Kim, J. H. Choi, L. J. Belenky, J. Giencke, M. K. Lee, W. Tian, X. Q. Pan, A. Siri, E. E. Hellstrom, C. B. Eom, and D. C. Larbalestier, Supercond. Sci. Technol. **17**, 278 (2004).
- [6] D. K. Finnemore, J. E. Ostenson, S. L. Bud'ko, G. Lapertot, and P. C. Canfield, Phys. Rev. Lett. **86**, 2420 (2001).
- [7] J. Nagamatsu, N. Nakagawa, T. Muranaka, Y. Zenitani, and J. Akimitsu, Nature **410**, 63 (2001).
- [8] D. S. Fisher, M. P. A. Fisher, and D. A. Huse, Phys. Rev. B **43**, 130 (1991).
- [9] R. H. Koch, V. Foglietti, W. J. Gallagher, G. Koren, A. Gupta, and M. P. A. Fisher, Phys. Rev. Lett. **63**, 1511 (1989).
- [10] T. K. Worthington, E. Olsson, C. S. Nichols, T. M. Shaw, and D. R. Clarke, Phys. Rev. B **43**, 10538 (1991).
- [11] N. -C. Yeh, W. Jiang, D. S. Reed., U. Kriplani, and F. Holtzburg, Phys. Rev. B **47**, 6146 (1993).
- [12] M. Pissas, S. Lee, A. Yamamoto, and S. Tajima, Phys. Rev. Lett. **89**, 097002 (2002).
- [13] R. Puzniak, A. Wisniewski, M. Angst, J. Jun, S. M. Kazakov, J. Karpinski, J. Roos, and H. Keller, Third International Workshop on Magnetism and Superconductivity of Advanced Materials.
- [14] M. Angst, R. Punziak, A. Wisniewski, J. Jun, S. M. Kazakov, J. Karpinski, J. Roos, and H. Keller, Phys. Rev. Lett. **88**, 167004 (2002).
- [15] R. Cubitt, M. R. Eskildsen, C. D. Dewhurst, J. Jun, S. M. Kazakov, and J. Karpinski, Phys. Rev. Lett. **91**, 047002 (2003).

- [16] S. S. Indrakanti, V. F. Nesterenko, M. B. Maple, N. A. Frederick, W. M. Yuhasz, and Shi Li, *Phil. Mag. Lett.* **81**, 849 (2001).
- [17] N. A. Frederick, S. Li, M. B. Maple, V. F. Nesterenko, and S. S. Indrakanti, *Physica C* **363**, 1 (2001).
- [18] S. Jin, H. Mavoori, C. Bower, and R. B. van Dover, *Nature* **411**, 563 (2001).
- [19] J. Deak, M. McElfresh, J. R. Clem, Zhidong Hao, M. Konczykowski, R. Muenchausen, S. Foltyn, and R. Dye, *Phys. Rev. B* **47**, 8377 (1993).
- [20] H. -J. Kim, W. N. Kang, E. -M. Choi, M. -S. Kim, K. H. P. Kim, and S. -I. Lee, *Phys. Rev. Lett.* **87**, 087002 (2001).
- [21] T. Nishizaki, T. Naito, and N. Kobayshi, *Phys. Rev. B* **58**, 11169 (1998).
- [22] T. Nishizaki, T. Naito, and N. Kobayshi, *Physica C* **317**, 645 (1999).
- [23] T. Nishizaki, T. Naito, and N. Kobayshi, *Phys. Rev. B* **61**, 3649 (2000).
- [24] P. Le Doussal and T. Giamarchi, *Phys. Rev. B* **57**, 11356 (1998).
- [25] K. H. P. Kim, W. N. Kang, M. -S. Kim, C. U. Jung, H. -J. Kim, E. -M. Choi, M. -S. Park, and S. -I. Lee, *Physica C* **370**, 13 (2002).

VI

Anomalous dynamic behavior of vortices amidst an emergent peak effect in CeRu₂ films

VI.A Introduction

The exotic superconducting compound CeRu₂, discovered in 1958 by Matthias *et al.*, [1] is a well known and heavily studied material. The past decade has seen intense renewed interest in this material due to it having some basic similarities to both high-T_c cuprate and heavy-fermion superconductors, and also due to the observation of the so called “peak effect,” an anomalous mixed state behavior wherein the vortex ensemble undergoes a transition to a considerably stronger pinning configuration resulting in a large increase of the critical current density within in a region near to the upper critical field, H_{c2}(T). Various mechanisms have been proposed for the origin of the peak effect in CeRu₂. One possibility that has been revisited is the inhomogeneous generalized Fulde-Ferrel-Larkin-Ovchinnikov (GFFLO) superconducting state [2, 3] which has a spatially modulated order parameter along the magnetic field direction [4]. Despite the extensive number of studies devoted to understanding the nature of the peak, and the large volume of

evidence against the FFLO state, debate still persists as to whether or not it exists in CeRu_2 , and is thus responsible for the peak effect in this compound. A more conventional explanation of the peak effect involves the collective bundle pinning scenario with a high density of weak pinning sites leading to a dynamical two-step depinning process [5]. The focus of other studies has been on the role of the few strong point defects and the possibility of unconventional pinning forces arising as a result of the renormalized electronic state due to valence fluctuations [6].

A number of studies strongly suggest that the structural properties of the crystal play a significant, perhaps essential, role in the mechanism of the peak effect.

(i) Ultrasound measurements have shown a substantial softening ($\sim 50\%$) of the shear modulus of CeRu_2 from room temperature down to ~ 20 K with a small upturn down to ~ 6 K without a structural phase transition taking place, pointing to the persistence of strong structural fluctuations [7]. At $T = T_c \sim 6$ K in zero field, further softening is observed by an anomalous downward kink in the shear moduli, which is suppressed to lower temperatures by application of a magnetic field. Upon closer examination of the region of the kink, further anomalous hysteretic field/temperature behavior of the shear modulus was seen [8]. It is observed here that this latter behavior is correlated with various hysteretic properties of the peak effect, including hysteresis in magnetization, $M(H)$, for minor magnetic field loops [9], and distinct regions of the magnetization $M(H)$ loop exhibiting differing relaxation rates [10].

(ii) It has been observed that the peak effect can be destroyed in single crystal samples by a rapid cooling of the sample from room temperature down to ~ 6 K [10]. This is consistent with the peak effect being tied to the softening of the atomic lattice moduli. By rapidly cooling the sample, it is work hardened, removing the necessary softness of the crystal for the peak effect.

(iii) Magnetostriction measurements, $\Delta\ell(H)$, in the peak effect region revealed an anomalous *increase* in the length of the crystal along the direction of

the applied magnetic field [4]. This behavior was also seen to be hysteretic as a function of field, and is readily seen to be associated with the peak effect. Even if the conclusion that the unusual field dependent behavior of the magnetostriction is evidence for the FFLO state is not correct, the correlation between $\Delta\ell(H)$ and the peak effect remains.

A common characteristic of the peak effect observed in various systems is that it only occurs in pure materials that contain extremely weak pinning forces, and as such is only observed in high quality single crystals. Films of CeRu_2 have been successfully grown in this study, with pinning force densities *weaker* than that seen in some single crystals. In a effort to further understand the peak effect mechanism in CeRu_2 we have grown thick film samples and have investigated their peak effect properties via electrical transport, $\rho(H, T)$, critical current density, $J_c(H, T)$, and magnetization, $M(H, T)$, measurements. Previous efforts by Groten *et al.* [11], to make CeRu_2 films resulted in samples with pinning force densities so strong that the region of peak effect, where enhanced pinning takes place, was effectively buried beneath the strong defect pinning. The films in the study presented here fall into a small grain ($d_{max} \sim 2\mu\text{m}$) or large grain (island) ($d_{max} \sim 10\mu\text{m}$) category, and exhibit significantly different transport properties which are thought to give insight as to the nature of the peak effect mechanism. The films exhibit residual resistivities comparable to moderate quality single crystals, and yet exhibit pinning force densities, $F_p(H, T)$, *less than* that found in high quality single crystals, and as such are expected to exhibit peak effect behavior. Remarkably though, the peak effect is missing in these samples from both transport, $\rho(H, T)$, and magnetization, $M(H)$, measurements. This is *not* due to strong disorder pinning overriding the peak effect region, as seen in the previous study of CeRu_2 films [11]. In this chapter, experimental evidence indicating a suppression of the superfluid density, ρ_s , in the region of the peak effect is presented. The maximum of the suppression of ρ_s is seen to be centered at the maximum of the magnetization hysteresis loop. The observation of a suppression of the superfluid

density is consistent with results from μ SR measurements of the magnetic penetration depth, λ [12, 13], wherein an anomalous increase of λ was found in the peak effect region, and as such indicates a corresponding increase of normal state electrons, quasiparticles, outside the vortex cores. These results are consistent with the existence of a nodal vortex state, *i.e.*, the FFLO state. However, an alternate possibility, which has a more conventional explanation for the increase of quasiparticles related to the well known structural fluctuations is considered. Furthermore, it is observed that the critical behavior of the vortices may also play an important role in the peak effect mechanism through an enhancement of the coupling of the vortices to the underlying fluctuating atomic/electronic host.

VI.B Experimental Details

Thick films of CeRu₂ were synthesized by pulsed laser deposition (PLD) using a Lambda Physik KrF laser with a wavelength of 248 nm. A polycrystalline CeRu₂ boule was prepared for use as an ablation target by arc-melting a stoichiometric mixture of Ce and Ru under an inert Ar atmosphere near 1 atm based on the procedure described by Dilley *et al.*, [5]. During the process, extra Ce was added to compensate for the Ce loss that occurs during arc-melting. The boule was then cut using a diamond wheel saw and was subsequently polished to yield a smooth surface. The resulting target had a 1.5 cm diameter surface and a thickness of 0.5 cm. Ablation took place in a clean background of $\sim 1 \times 10^{-5}$ torr UHP Ar after initially pumping down to a base pressure of $\sim 5 \times 10^{-10}$ torr. Films ranging in thickness from 1000 Å – 4.5 μ m were grown on r-plane cuts of sapphire (Al₂O₃) (films "A" and "B,") and on c-plane cuts of Lanthanum Aluminate (LaAlO₃) (film "C"). The thickness of samples presented in this study are 4 μ m (film "A") and 4.5 μ m (films "B" and "C"), with planar dimensions of $\sim 1 \times 2$ cm². The target to substrate distance was 3.2 cm, and the estimated energy density of the beam on the target was ~ 5 J/cm² for film "A" and ~ 20 J/cm² for "B" and "C". Films

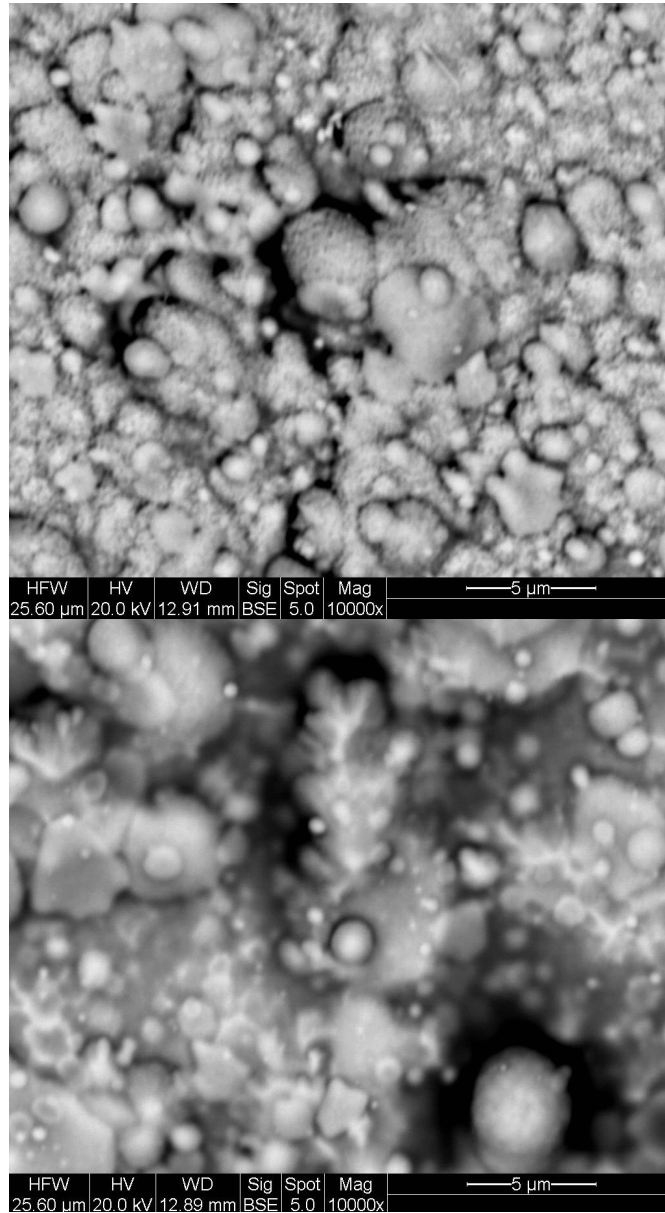


Figure VI.1: SEM image of CeRu_2 films “A” (SG) (top) and “B” (LG) (bottom) grown on Al_2O_3 substrates (r-plane cut). The films were grown under identical conditions (see text) with the exception of the laser ablation energy density. The energy densities were $\sim 5 \text{ J/cm}^2$ and $\sim 20 \text{ J/cm}^2$ for the small and large grain films respectively. Both films are well into the clean limit with mean paths within the grains $\ell \sim 1000 - 2000 \text{ \AA}$.

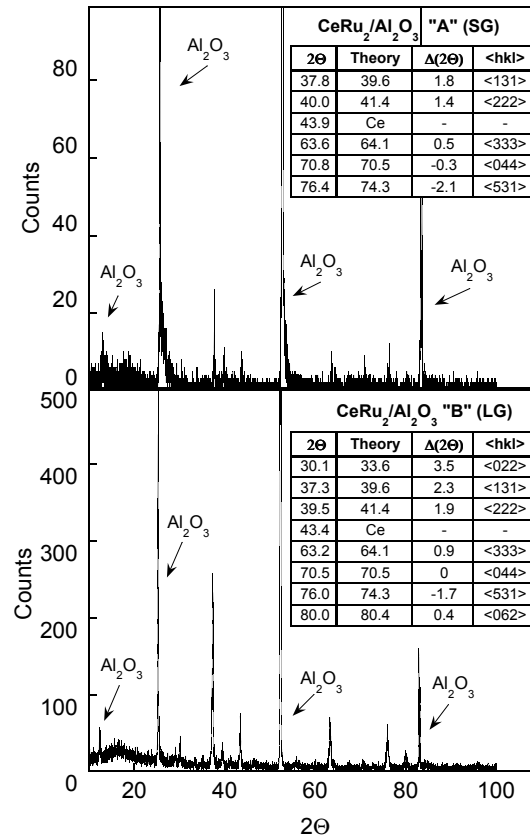


Figure VI.2: X-ray data for the small grain film, “A” (top panel), and the large grain film “B” (bottom panel). The difference in average grain size is evident by the increase of count number. The primary crystalline alignment is along the $\langle 111 \rangle$ direction. Other orientations are also present along with minor Ce-Ru impurity phases.

were found to grow best at 400 °C. Growth was followed by an in situ anneal at 760 °C for 30 minutes.

Magnetization $M(T)$ and $M(H)$ data were taken using a Quantum Design Magnetic Property Measurement System (MPMS) in fields up to 5.0 T and for temperatures from 1.8 K up to 10 K. For magnetotransport measurements, gold leads were attached with silver epoxy to gold pads sputtered on the films, with the resulting contact resistance $< 1 \Omega$. Standard four-wire DC resistance measurements were performed using a Keithley 220 current source, a Keithley 2182 nanovoltmeter, and a Quantum Design Physical Property Measurement System (PPMS) from temperatures 1.8 K to 300 K and in fields up to 9.0 T. Electrical resistivity, $\rho(H, T)$ measurements were made in a static manner, that is, at incremental values of the magnetic field (temperature) for a given fixed temperature (field). Unless otherwise stated, all resistivity data were taken by preparing the sample in a zero field cooled (ZFC) initial state. Then, for $\rho(T)$ data, a field was applied, followed by incremental increases of temperature to a maximum a few degrees above T_c , then lowered by the same increments. Following the ZFC to a fixed temperature, $\rho(H)$ data were taken in incremental increasing field steps to a maximum of 7 – 9 tesla, then lowered by the same increments. A sample was also cut from the target material for comparison of magnetization and electrical transport properties. It was polished to have sample dimensions $\ell \times w \times t = 0.245 \text{ cm} \times 0.111 \text{ cm} \times 33 \text{ }\mu\text{m}$. The thickness is ~ 8 times that of the films. The magnetic field for all of the above measurements was applied perpendicular to the film surface and to the largest target sample surface.

VI.C Experimental Results

Films grown on LaAlO_3 substrates were found to have very high pinning force densities which overwhelmed the peak effect region. These films were grown at the same time as those on Al_2O_3 substrates. The main results examined in this

study are the low pinning force density films grown on Al_2O_3 substrates. Results from a film grown on LaAlO_3 are also shown to demonstrate that the unusually low pinning force density is intrinsic to the Al_2O_3 grown films. The SEM data (Fig. VI.1) show that the surface of the films and the regions between the islands are granular with grain diameters (along the a – b plane of the substrate) ranging in size from $d \sim 0.5 - 2 \mu\text{m}$ for film “A” and $d \sim 1 - 5 \mu\text{m}$ for film “B”. The morphology of the the small grain (SG) film “A” is primarily granular with some island type growth. In the large grain (LG) film “B,” the predominant structures are islands of diameter $d \approx 10\mu\text{m}$ which appear to be partially in direct contact with each other, with smaller grains in the open regions between and on the surface. X-ray diffraction data shown in (Fig. VI.2), demonstrate that the films are polycrystalline and the island growth is primarily aligned along the $\langle 111 \rangle$ direction. Some minor impurity phases of Ce-Ru intermetallics are also seen. The higher intensities of the X-ray diffraction data for film “B” over that of “A” is readily attributable to the larger average grain size of the film.

The superconducting magnetic transitions, $\chi \equiv 4\pi M(T)/H$, of the target sample and the two films are shown in Fig. VI.3. The value of the onset critical temperature, T_c^{onset} , is 6.2 K and 5.7 K, with 10% – 90% transition widths, $\Delta T_c \approx 0.64$ K and 0.45 K for the target and films, respectively. The target sample exhibits a full Meissner effect, within experimental error, demonstrating the quality of the target material. The insets to Fig. VI.3 show $\chi \equiv 4\pi M/H$ data of the films. The magnetization data in inset (a) was adjusted by accounting for an effective enhancement of the superconducting volume due to the coating of the edges of the substrate with CeRu_2 . The effect of the substrate edges being coated with CeRu_2 is to shield the magnetic field over a greater volume than just that of the film dimensions. The edge coating is not uniform and does not extend over the entire thickness of the substrate. While it is difficult to estimate to what extent the edge coating affects the magnetization measurement, the thickness of the effective

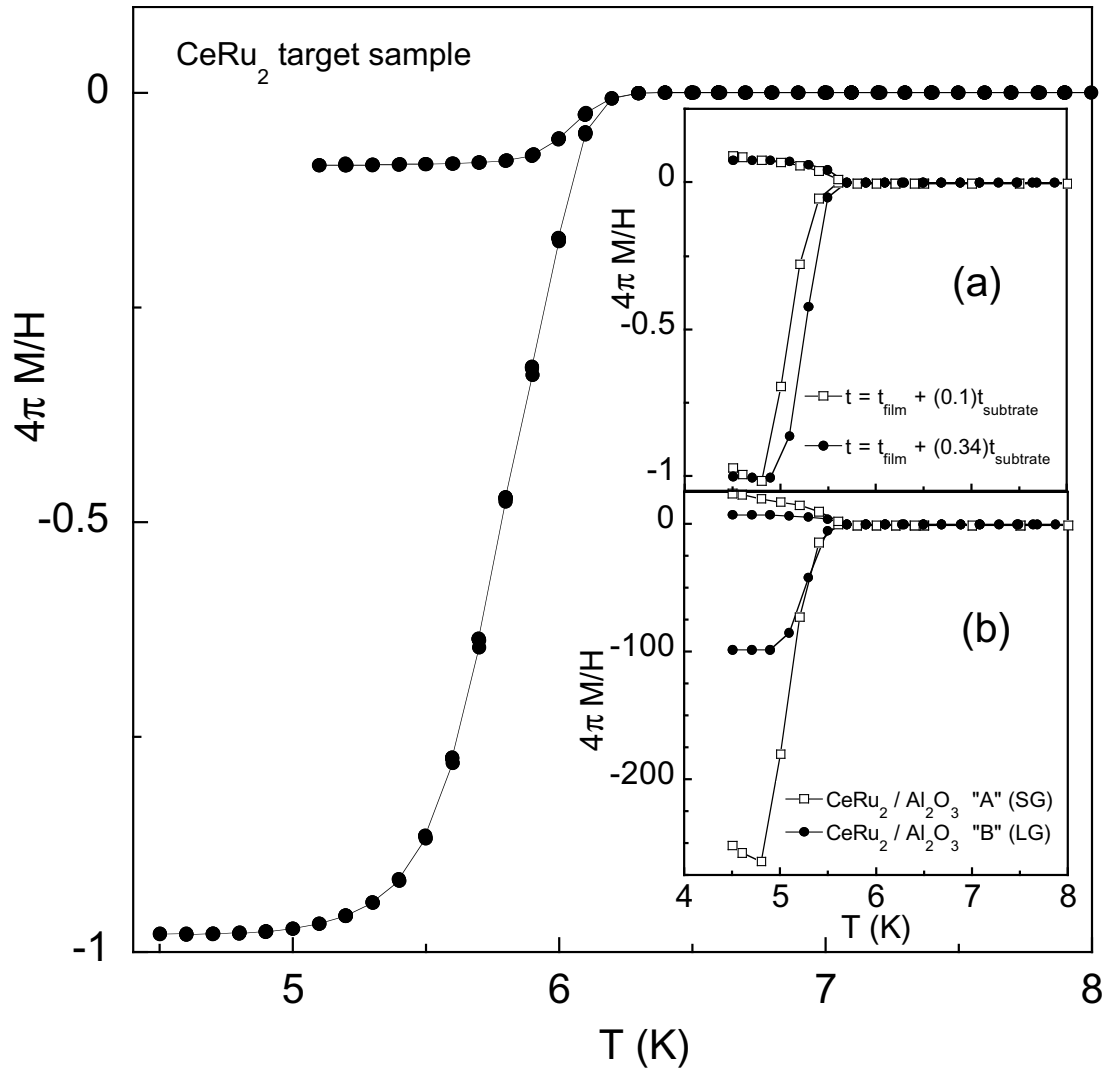


Figure VI.3: Magnetic susceptibility, $\chi \equiv 4\pi M/H$, data for the target sample and films (inset). Inset (a) shows adjusted values of χ for the films after taking into account an effective volume due to the coating of the substrate edges with superconducting material. Inset (b) shows the unphysically large values of χ for the films found by using the film dimensions. See text for details.

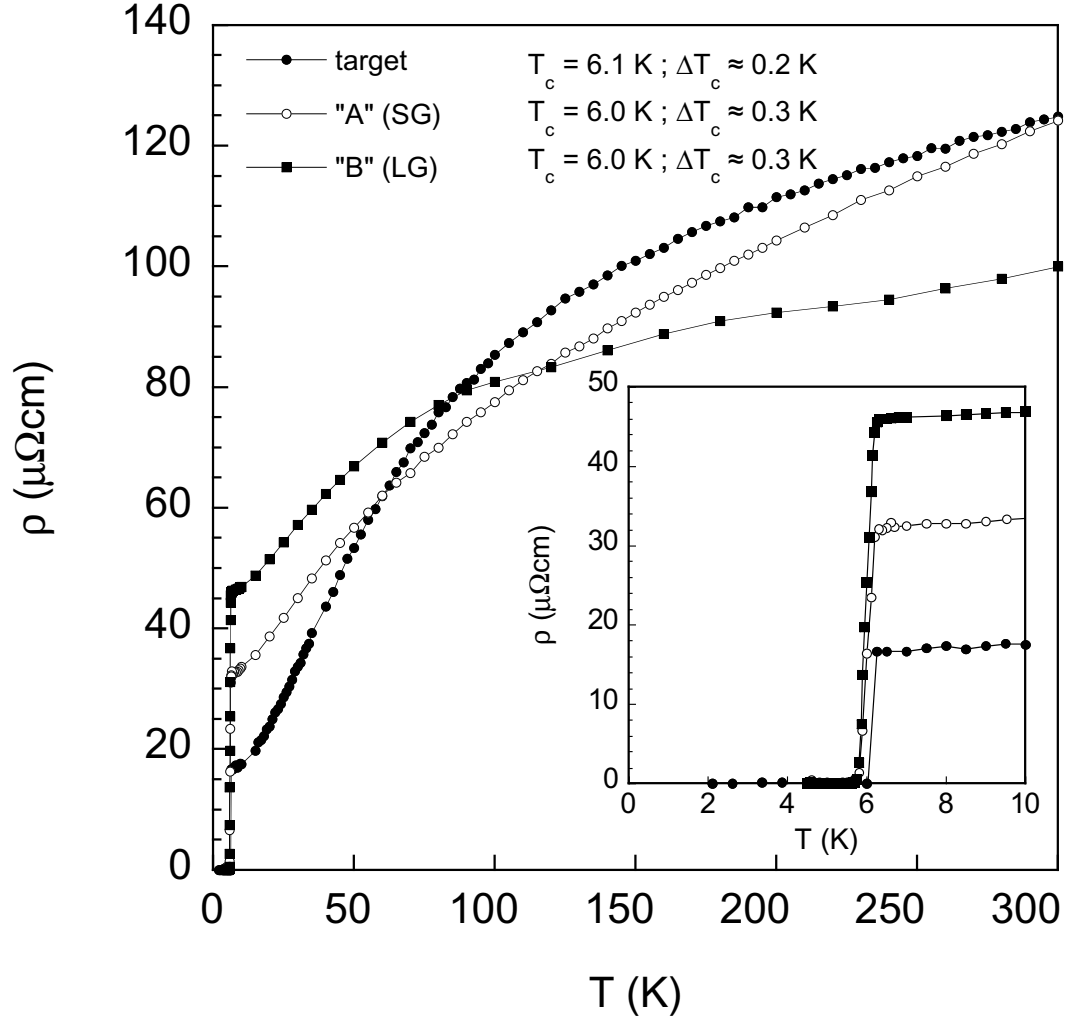


Figure VI.4: Resistivity, $\rho(T)$, data for target sample and films "A" and "B". Note that the larger grain size (more crystalline) film, "B", shows signs of substrate-film interface strain upon cooling: the intrinsic residual resistivity of "B" is estimated to be a factor of 2 smaller than shown.

volume, $t = t_{film} + (x\%)t_{substrate}$ is found by assuming a full Meissner effect and solving for the additional thickness needed after accounting for a demagnetization factor [14].

Resistivity data from the two films and from a sample taken from the PLD target material are shown in Fig. VI.4. The resistivities, $\rho(T)$, of all three samples are qualitatively similar. However, film “B” shows signs of substrate-film interface strain as a result of mismatched thermal expansion rates. This is naturally of more importance in the large grain (LG) crystalline film, since the sizes of the grains of the LG film are equal to or greater than the film thickness resulting in the majority of the grains being connected to the substrate surface. The largest grains of the small grain (SG) film are approximately equal to or less than the film thickness. The critical temperature, defined as the midpoint of the resistive transition, is $T_c = 6.1$ K for the target sample, and $T_c = 6.0$ K for both of the films, with ΔT_c defined as the 10% – 90% resistivity values, $\Delta T_c \approx 0.2$ K and 0.3 K for the target and films respectively. The residual resistivities are $\rho_0 \approx 15 \mu\Omega\text{cm}$ and $\rho_0 \approx 30 \mu\Omega\text{cm}$, for the target sample and the films (inset Fig. VI.4). The residual resistivity of film “B” is estimated to be approximately a factor of two less than that shown without the effect of the substrate strain.

The electronic mean free path, ℓ , in the films was estimated by comparison of the residual resistivities of the films to that of a single crystal whose mean free path was determined by de Haas-van Alphen measurements [15] where $\rho_0 = 0.6 \mu\Omega\text{cm}$, $\xi_0 = 79 \text{ \AA}$, the residual resistivity ratio is 270, and the mean free path is $\ell \approx 2000 \text{ \AA}$ - 2400 \AA , depending upon the field–crystal orientation.

From the relation $\rho_n \ell = \left[\frac{2}{3} N(0) v_F e^2 \right]^{-1}$ we have $\ell_{film} = \ell_{bulk} \frac{\rho_n(bulk)}{\rho_n(film)}$. This gives $\ell_{film} \approx 58 \text{ \AA}$. From the relation $\ell_{film}/\ell_{bulk} = RRR_{film}/RRR_{bulk}$ [5], where RRR is the residual resistivity ratio $\rho(300K)/\rho_0$, we find $\ell_{film} \approx 35 \text{ \AA}$. Either estimate gives $\ell < \xi_0$ implying that the films are in the dirty regime, which is in conflict with the conclusion reached from the pinning force density measurements described below, where the pinning of vortices in the films is found to be similar

to that found in high quality single crystals. This contradiction can be resolved by recognizing that it is likely that the connections between the grains and/or islands are considerably more resistive than the crystal material due to the high resistivity of the junctions between grains. If instead, we make use of a property of very clean superconductors wherein the introduction of a small amount of point disorder, the upper critical field, $H_{c2}(0)$, will be enhanced as a result of the decrease of the superconducting coherence length ξ with minimal effect upon the critical temperature, T_c [16], we arrive at the relation

$$\ell_{film} = \ell_{bulk} \left(\frac{\xi_{film}(0)}{\xi_{bulk}(0)} \right)^2.$$

This gives $\ell_{film} \approx 1800 \text{ \AA}$ for the small grain film and $\ell_{film} \approx 1600 \text{ \AA}$ for the large grain film. It seems most likely that the crystalline grains of the films have a defect density and corresponding mean free path comparable to single crystals. If this is true, then the grains of the SG film, with diameters of $d \sim 0.1 - 2 \mu\text{m}$ have few if any defects. The grains of the LG film, with diameters of $d \sim 0.5 - 10 \mu\text{m}$ have only a small number of defects.

The primary source of impedance to vortex motion in the SG films is the surface barrier of the grains and defects within any amorphous material between the grains. Further evidence for a very low density of defects within the SG sample is found from low current resistivity, $\rho(T)$, and $V - I$ data. The natural log of the resistivity versus inverse temperature, $\ln(\rho(T))$ vs. $1/T$, at various magnetic fields, is plotted in Fig. VI.5. The data conform to a thermally assisted flux flow (TAFF) type behavior over the linear portions as plotted, corresponding to a resistivity that is described by $\rho(T) = \rho_0 \exp[-U/k_B T]$ [8].

In contrast, the large grain film exhibits resistivity, $\rho(T)$, behavior suggestive of first order melting of a vortex-lattice. In Fig. VI.6 and the inset, the sharpness of the resistive superconducting transition in various magnetic fields is seen in both $\rho(T)$ and $d(\rho(T))/dT$, with transition widths of $\Delta T \sim 0.2 \text{ K}$ for all fields. However, no measurable hysteresis in temperature could be observed, so

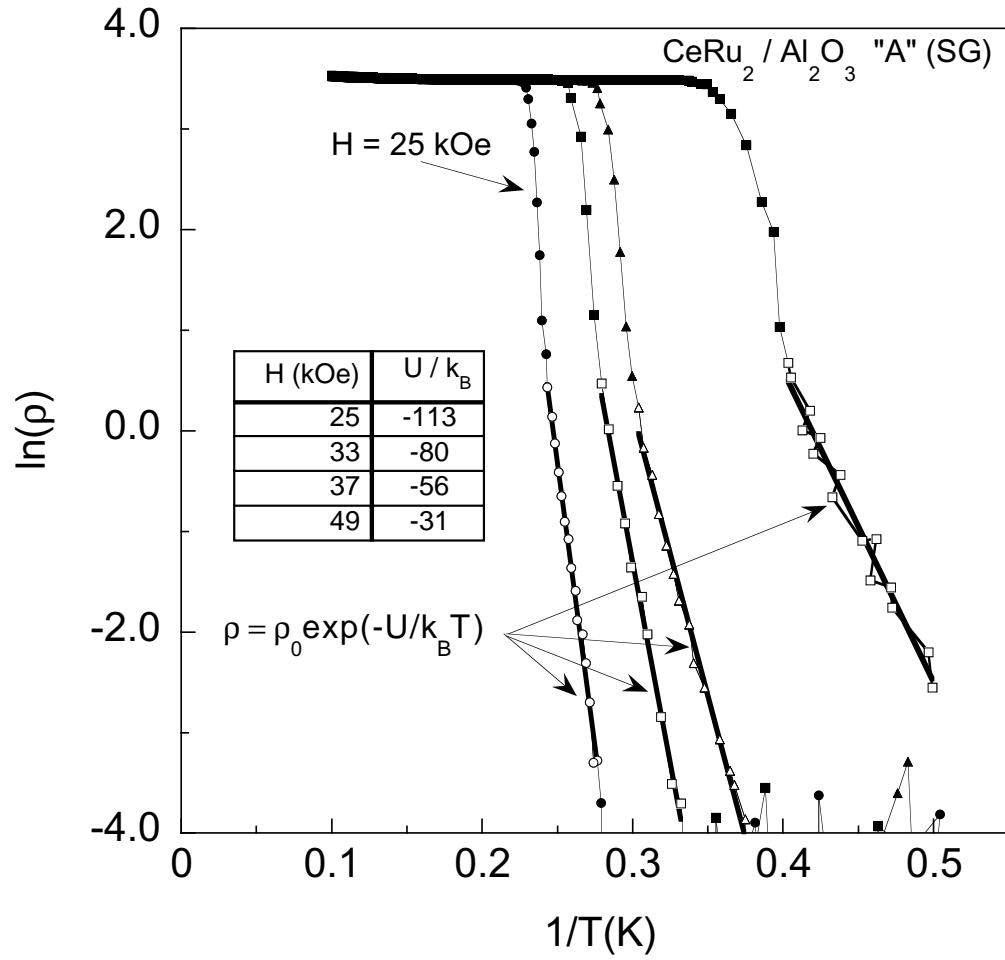


Figure VI.5: Natural log of the resistivity vs. inverse temperature, $\ln \rho(T)$ vs $1/T$, data from film "A". The data demonstrate that the vortex ensemble is in a TAFF regime in this film.

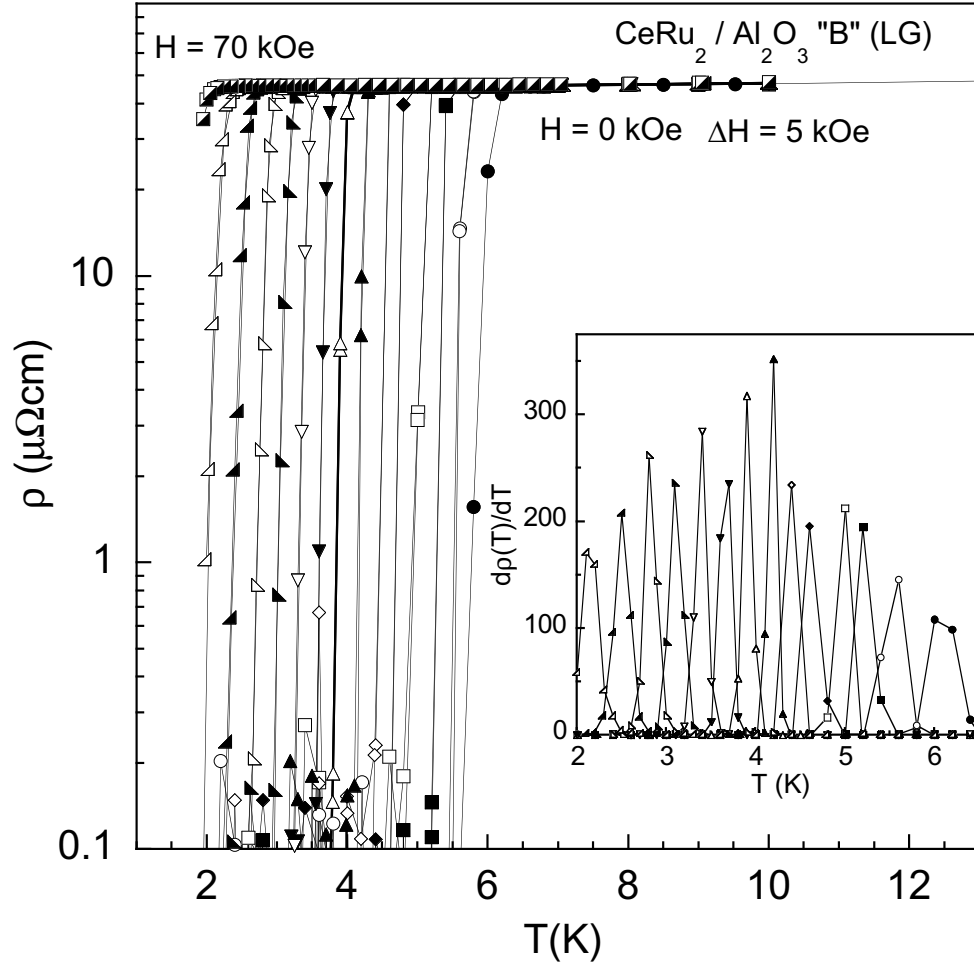


Figure VI.6: Resistivity, $\rho(T)$, data for film "B". Note that the peak effect like behavior seen in the $\rho(H)$ data is not observable here. The sharpness of the $d\rho(T)/dT$ data for film "B" indicates that the melting transition is, or is very nearly, a first order vortex lattice melting transition. Transition widths do not broaden measurably with field, with $\Delta T \approx 0.2$ K for all fields.

the transition may just be a very clean vortex glass [17, 18, 19], or Bragg glass [20] transition.

While the peak effect is completely absent in $\rho(T)$ data for both films, the behavior of $\rho(H)$ data is significantly different, and seemingly contradictory. In Fig. VI.7, $\rho(H)$ data for both films are shown in a semi-log plot to reveal the low resistivity features. The difference between the behavior of the two samples is highlighted in the inset which shows $\rho(H)$ data from both at $T = 4.5$ K normalized to the residual resistivity values of ρ_0 and to the onset field, H_{onset} , of the transition. A finite resistivity value is observed down to the lower field value of the peak effect region in both samples. The behavior of the resistivity at field values below H_{onset} , where the peak effect in $\rho(H)$ ought to be seen, can be understood as the result of the extremely weak pinning in these samples, with the higher resistivity contribution from vortex dissipation arising in the cleaner small grain sample. In the inset, note the kink in the data at $H/H_{onset} \approx 0.7$ for the small grain sample, and the sharp drop in the data at $H/H_{onset} \approx 0.8$ for the large grain sample. These features are very close to where the resistance would vanish or reach a minimum, if the peak effect were observed [21].

It appears then, from the above results, and also from pinning force calculations presented below, that while the weak pinning condition is definitely satisfied in both samples, this is not a sufficient condition for the peak effect, and thus the peak effect mechanism is frustrated or absent. Furthermore, keeping in mind that all measurements start from the ZFC condition, the complete absence of a resistive signal below the transition in temperature, $\rho(T)$, and the contrasting finite value below the transition in field, $\rho(H)$, points to an obvious difference of the evolution of the dynamical state of the vortices upon approaching the transition by increasing either temperature or magnetic field. This difference is further highlighted by the result that the upper critical field lines, determined by using the field/temperature value at a resistivity value of $\rho = 0.1 \mu\Omega\text{cm}$, $H_{c2}(T)[\rho(H)]$ and $H_{c2}(T)[\rho(T)]$ do not agree, and, are separated by a distance larger than can

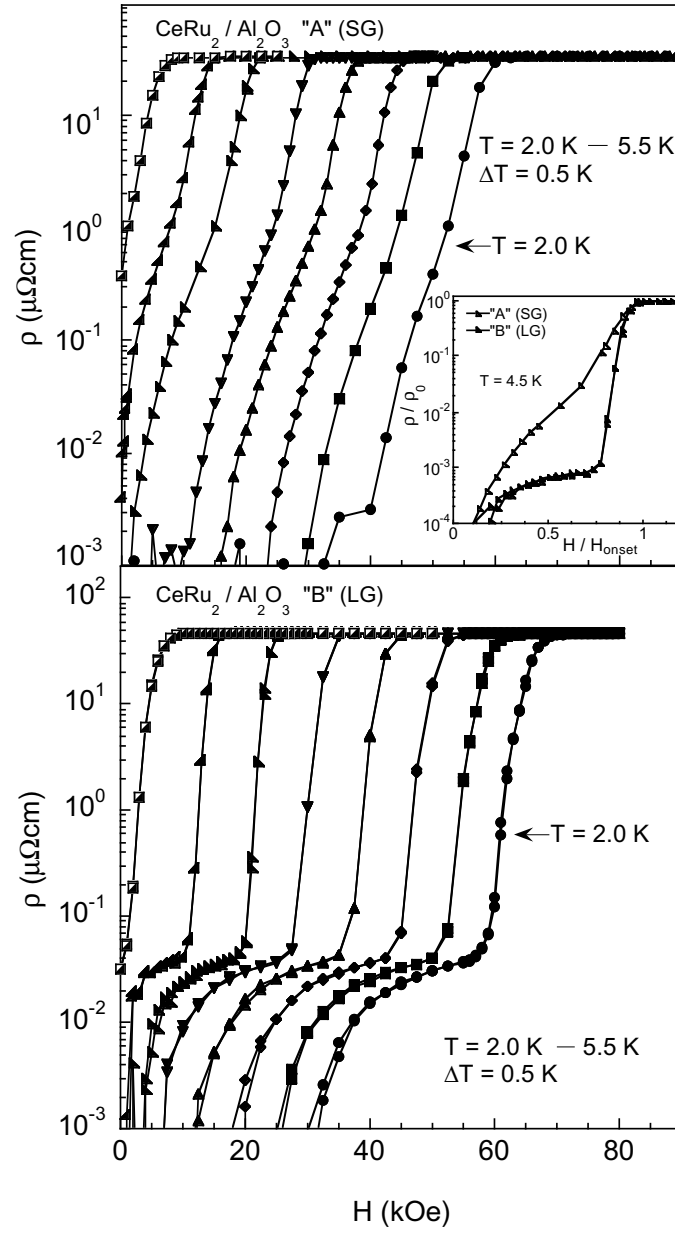


Figure VI.7: Resistivity, $\rho(H)$, data for films "A" and "B". The inset shows data from both samples at $T = 4.5$ K, normalized to ρ_0 and to the field value of the onset of the transition, for comparison of behavior in the region where the peak effect is usually observed. See the text for further discussion.

be attributed to any experimental error. It is suggested here that the difference in vortex dynamics for the resistive transition in temperature, $\rho(T)$, and in field, $\rho(H)$, as well as the discrepancy between $H_{c2}(T)[\rho(H)]$ and $H_{c2}(T)[\rho(T)]$ can be attributed to differences in the structural response of the atomic lattice with respect to field and temperature. That is, the dynamic behavior of the vortices are responding to changes within their environment, *i. e.*, changes of the electronic band configuration due to thermal or field driven structural deformation and/or fluctuations. Further explanation of this suggestion is given in the Discussion section below.

Finally, a comparison is made between the behavior of $\rho(H)$ in the large grain film, “B”, and of a similar large grain film grown at the same time, “C”, on a LaAlO_3 substrate in Fig. VI.8. The samples have a similar morphology, (see Fig. VI.1 right panel,) with slightly larger island diameters on the LaAlO_3 grown film, and presumably have the same in-grain point defect density. Remarkably though, in contrast to film “B”, there is no detectable resistive signal in film “C” in the peak effect region. As seen below, the pinning force density of the LaAlO_3 grown sample far exceeds either of the Al_2O_3 grown films throughout all regions of the phase diagram. With the only difference between the samples being the substrate upon which they were grown, there are two possible explanations for the dramatic difference of pinning characteristics. (*i*) La ions could conceivably have diffused from the substrate into the the interface region of the CeRu_2 film. However, it is unlikely that this would have any impact on the pinning properties since the regions of the film away from the interface would not be contaminated, and it has been shown that La doping produces no increase in the pinning potential [22]. (*ii*) substrate-film strain is seen to affect the resistivity $\rho(T)$ of the sample as it is cooled down, (as mentioned above for Al_2O_3 grown sample “B”,) and at low temperatures the strain is the greatest. While the strain distribution throughout the film it is not quantifiable at this time, what is known is that the thermal expansion coefficient values of the substrates are considerably different;

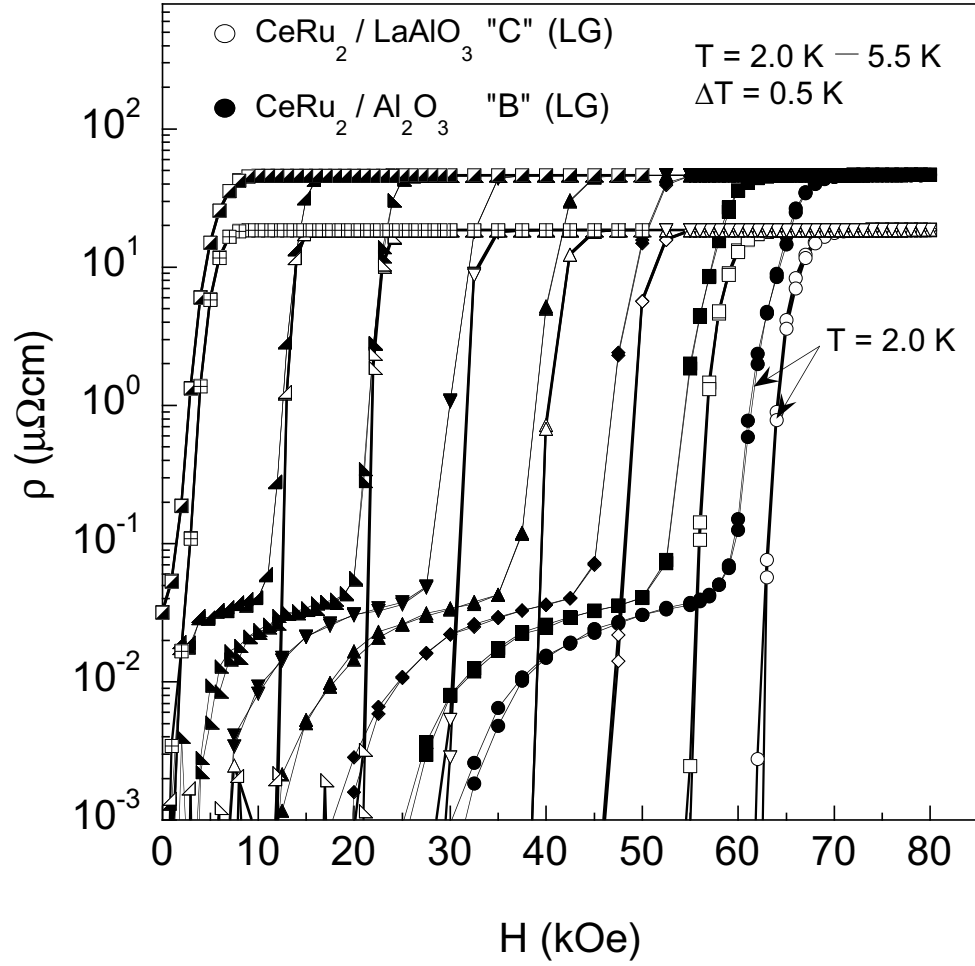


Figure VI.8: Resistivity, $\rho(H)$, data for film "C" (LaAlO_3 substrate) and film "B" (Al_2O_3 substrate), grown at the same time. The different behavior at low fields is attributed to strain in the films. See the text for details.

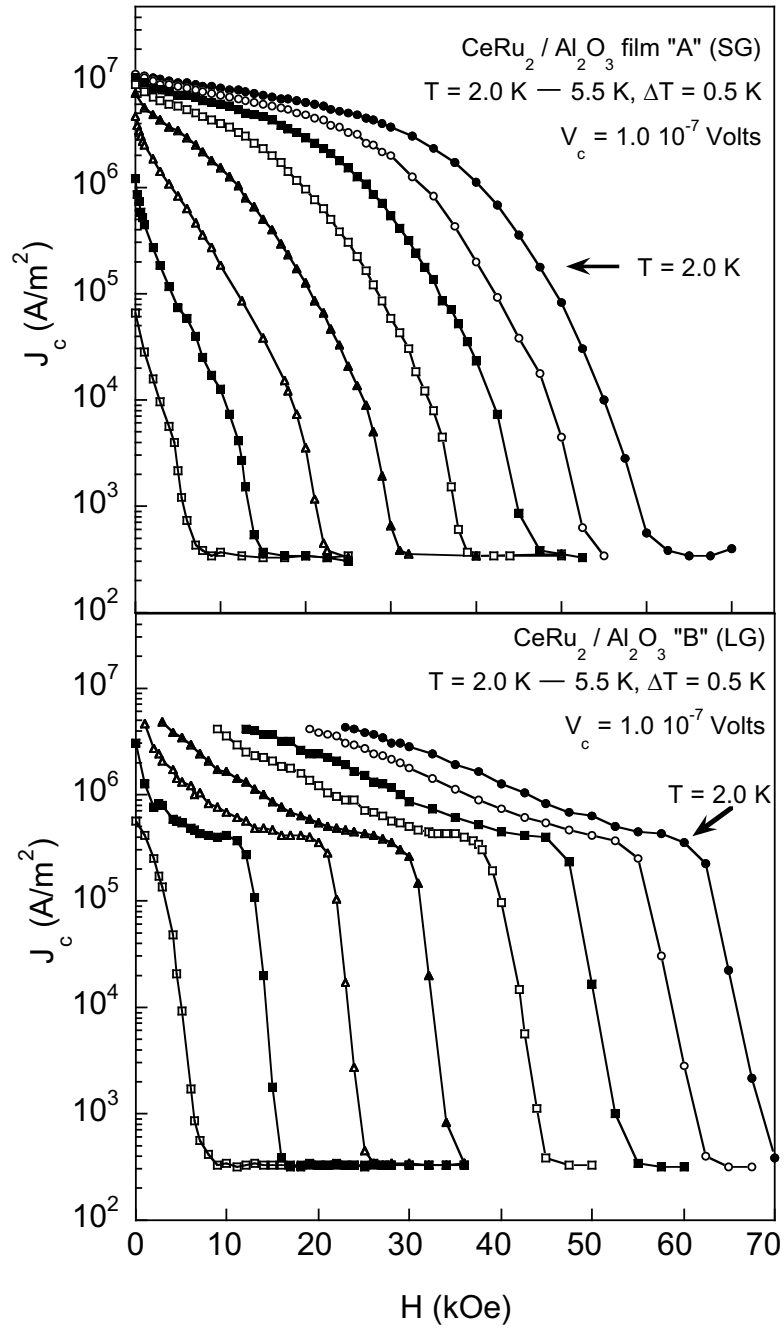


Figure VI.9: Critical current density, $J_c(H)$, data of the small grain film "A" and the large grain film "B". The low field J_c values of the two samples are comparable, however, an increase of J_c in the large grain film over that of the small grain film at fields corresponding to the peak effect region is seen.

$7.50 \times 10^{-6} \text{ K}^{-1}$ for Al_2O_3 and $9.2 \times 10^{-6} \text{ K}^{-1}$ for LaAlO_3 , corresponding approximately to a 20% higher in plane strain on the single crystal islands. How this strain changes the $\rho(H)$ peak effect behavior is given further attention to in the discussion section below.

The behavior of the critical current density, $J_c(H, T)$, and pinning force density, $F_p(H, T)$, obtained from V–I measurements, of the small and large grain Al_2O_3 grown films, is examined next. The critical current densities, $J_c(H)$, at fixed temperatures, of both samples is shown in Fig. VI.9. The value of $J_c(H)$ was determined by the value of the current at a fixed voltage value of $1 \times 10^{-7} \text{ V}$, for each V–I curve. The value of the critical current density in both samples at low fields are nearly equal. In the field regions where the peak effect is expected to occur, a definite increase of the critical current density of the large grain sample over that of the small grain sample is seen.

The low field values of J_c , and subsequently F_p , in both films are of the same order of, or less than, that found in high quality single crystals [9, 23]. The pinning force density, defined as $\mathbf{F}_p(H) = \mathbf{J}_c(H) \times \mathbf{H}$, of both samples, at temperatures ranging from 2 – 5 K plotted vs field scaled to the upper critical field, H/H_{c2} , is shown in the top panel of Fig. VI.10. The emergence of the peak effect in the large grain sample, already evident from the behavior of the critical current density, is readily seen here. In the lower panel of Fig. VI.10, the scaled pinning force, $\kappa_1 F_p/H_{c2}$, as derived by Tenya *et al.* [9], is plotted, where $\kappa_1 = H_{c2}/\sqrt{2}H_c$ is the Ginzburg-Landau parameter. The values of $\kappa_1(T)$ used here to scale F_p are those found by Tenya *et al.* [9]. If the pinning mechanism at each temperature value is the same over the entire field range, then $F_p(H)$ will scale onto a single universal curve. The low field–low temperature region of the data of the small grain sample does in fact scale onto a single curve, as does the high field–low temperature region of the data of the large grain sample. It also appears that the low field–low temperature data of the large grain sample might also scale to the same line as the small grain sample, though the data in this region

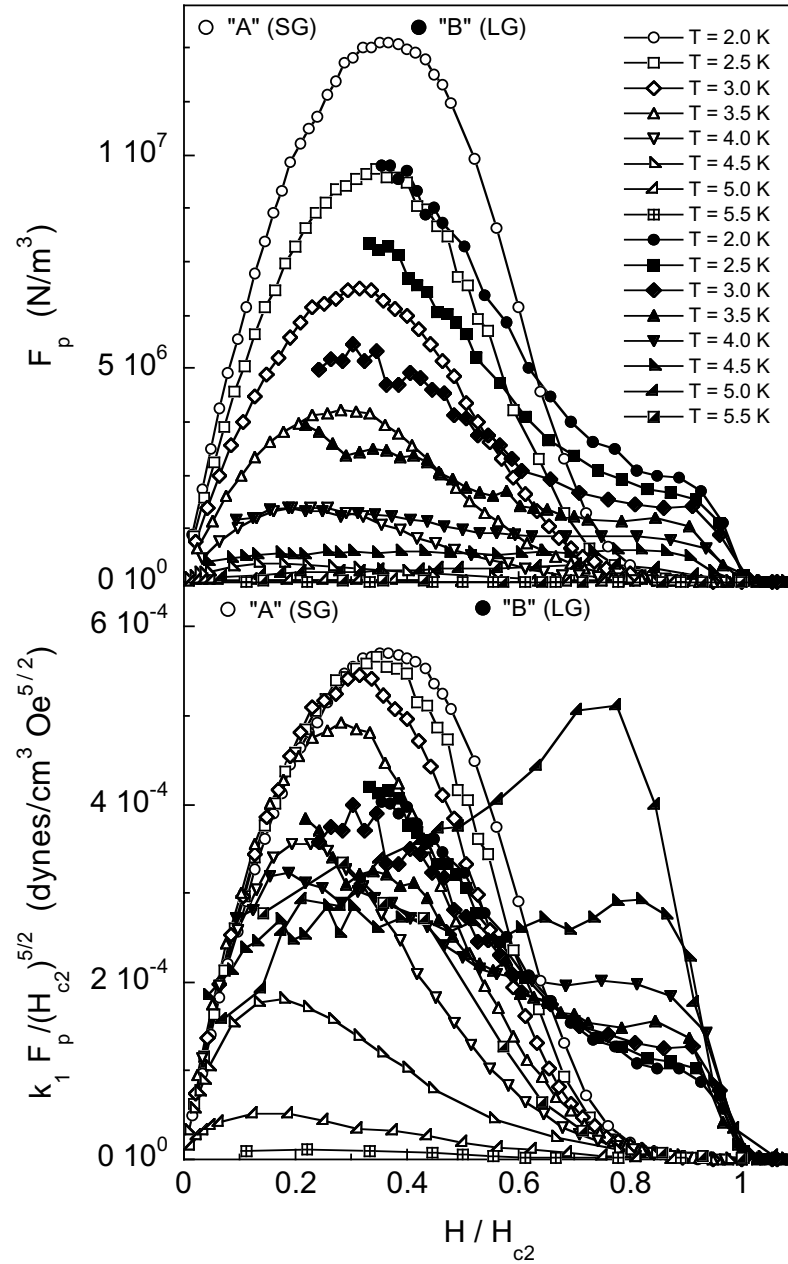


Figure VI.10: $F_p(H)$ and scaled $F_p(H)$ data for films “A” and “B” demonstrating the different behavior in and outside of the peak effect region. Note the emergence of the PE in the *dirtier* film, “B,” similar to that seen in single crystals.[23] A direct comparison of pinning force values of the films to single crystals is complicated by the additional pinning due to grain boundaries in the films.

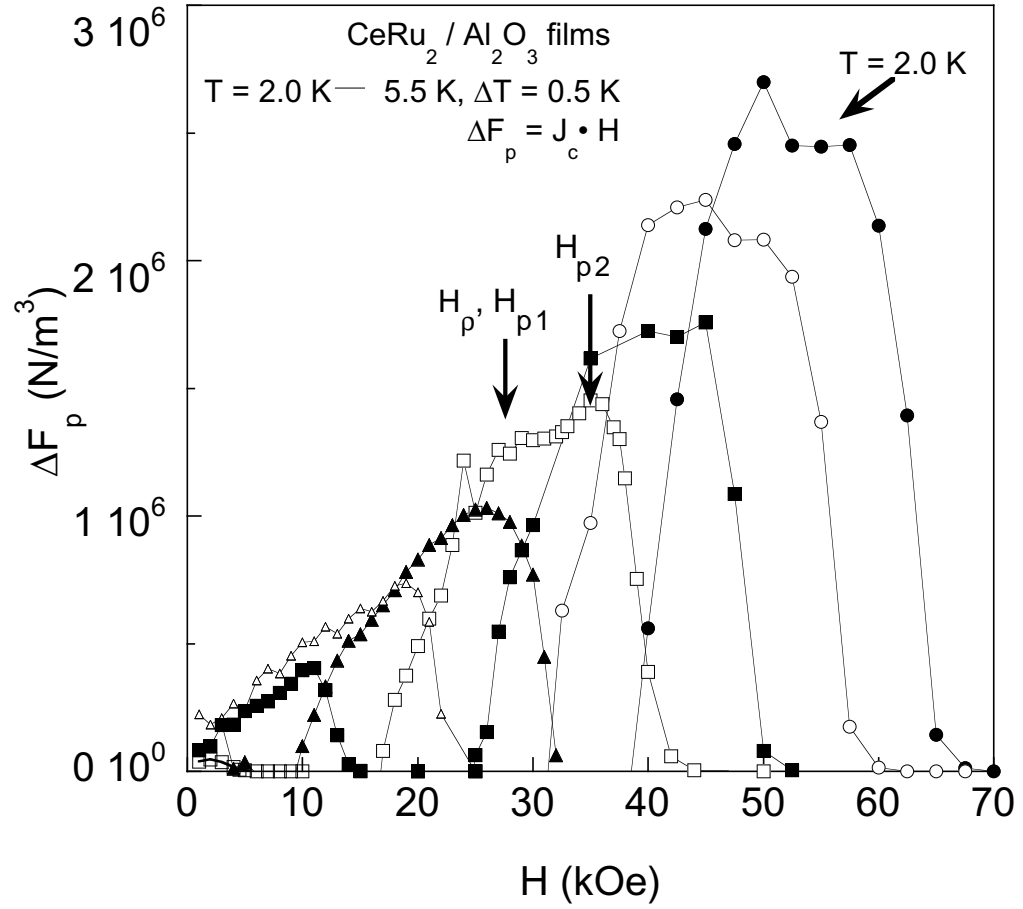


Figure VI.11: The enhanced pinning force region of large grain film “B”, corresponding to the peak effect region. Note the double peak structure, as indicated for the $T = 3.5 \text{ K}$ data.

is too limited for a definite observation. These results highlight the different nature of the pinning mechanisms in the conventional and peak effect regions, a result noted for single crystals [23], and a point that will be returned to in the discussion section below. The difference between the pinning force density, ΔF_p , of the small and large grain samples is shown in Fig. VI.11 to further emphasize that the peak effect mechanism is absent in the small grain sample, and that the increase seen in the large grain sample is in fact attributable to the emergence of the peak effect mechanism.

In Fig. VI.12 magnetization data from the target sample is compared to that of the large grain film. The peak effect is seen in the target sample and compares to typical results for polycrystalline samples [21]. The magnetization data for the film show that the pinning force density remains finite up to a field value near to the edge of the peak effect region, then collapses to zero. This behavior is observed for all $M(H)$ data at temperatures $5.5 \text{ K} \leq T \leq 6.1 \text{ K}$. The value of the critical current density, $J_c(H)$, determined via transport measurements, on both films and the difference, $\Delta J_c(H)$, are plotted for comparison. The increase of J_c in the large grain film is seen to be correlated with the peak effect region. Also, indicated by the shaded area, is the region over which the superfluid density is suppressed. This is inferred from scaling of the $E - J$ data discussed below. The important features to be noticed are (i) that the low field boundary of this critical region coincides with the sudden drop in the pinning force density indicated by $M(H)$ data, (ii) the critical field, H_ρ , coincides with the maximum of the peak effect, and (iii) the upper field boundary coincides with the maximum of the pinning force density peak, H_{p2} , inferred from $\Delta F_p(H)$ data, just prior to the collapse of the peak effect region.

Electric field vs. current density, $E - J$, data is shown in the inset of Fig. VI.13 from film “B”, and in the main panel the highlighted portions of the same data after they have been scaled. A modified scaling form based on the model of Fisher, Fisher, and Huse [19], has been used, where now the vortex glass

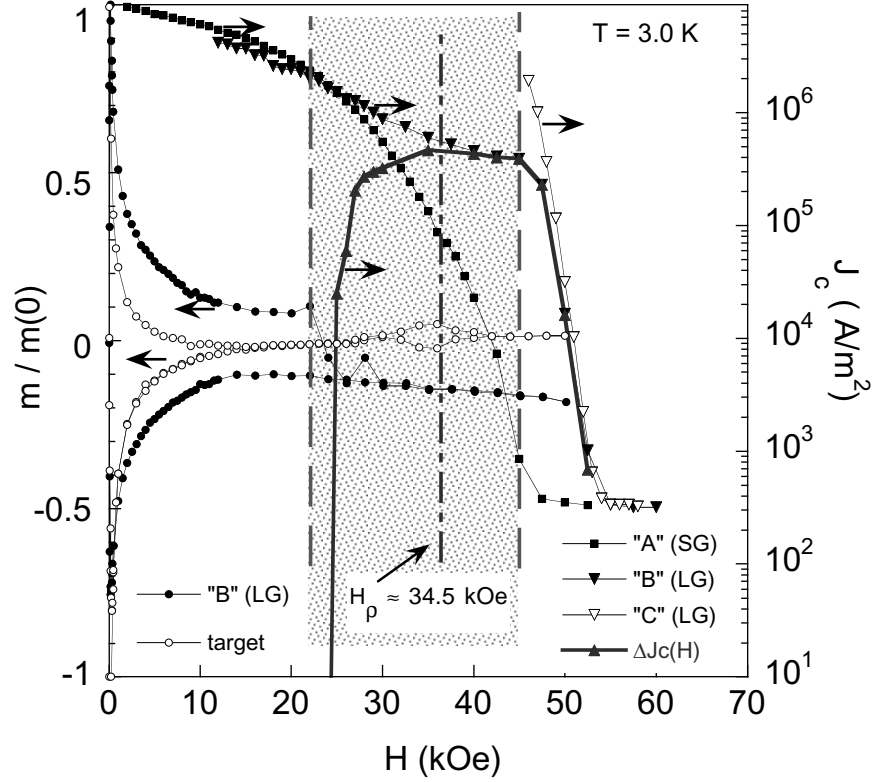


Figure VI.12: Normalized magnetization data, $M(H)$, at $T = 3.0$ K, for the target sample and the large grain film “B”. Notice that the peak effect is observable in the polycrystalline target sample, with a region of low to zero critical current density, $J_c = 0$, between the conventional and peak effect regions. The pinning force density of the film remains finite well into the region where it disappears for the target sample, and then rapidly collapses over a small field range at a value just below the peak effect region. Also shown are the critical current densities of the small grain (“A”) and large grain films (“B” and “C”) as determined from V–I measurements. Note that the critical current density in film “C,” grown on an LaAlO_3 substrate, is much greater than films “A” and “B,” grown on Al_2O_3 substrates. The difference of the critical current density values of “A” and “B,” $\Delta J_c(H)$, is plotted as well, emphasizing that the increase of the critical current density, $J_c(H)$, in the large grain sample is attributable to the peak effect. The shaded area corresponds to a region of suppressed superfluid density as evidenced by critical dynamic-like vortex behavior with the critical field value, H_g , corresponding to the maximum of the peak effect loop. See the text for further explanation.

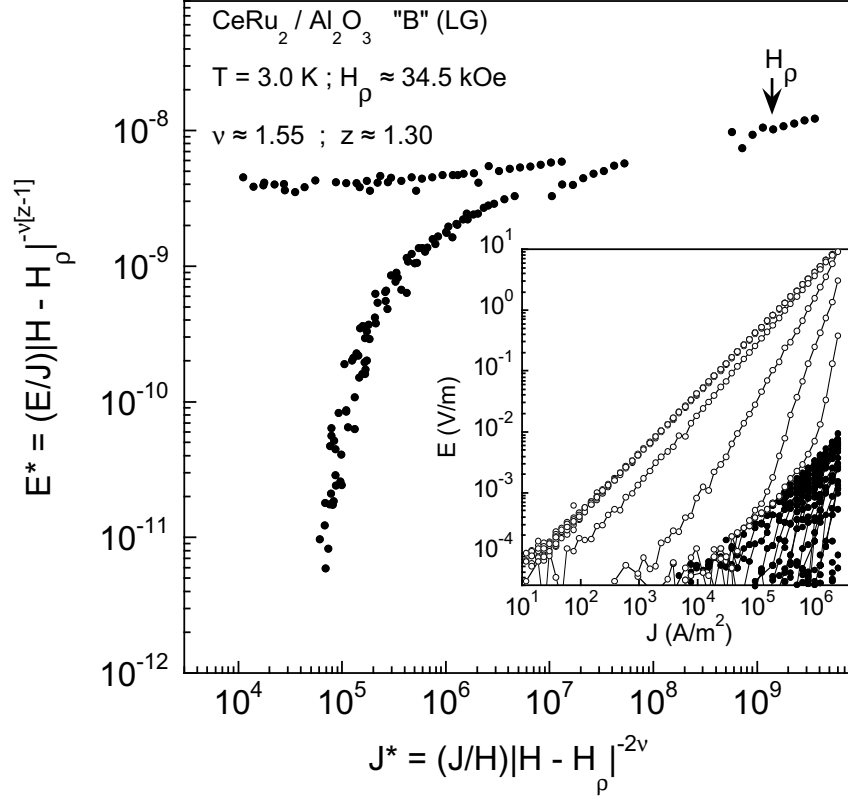


Figure VI.13: Electric field—current density, $E - J$, data for the large grain film “B” scaled by the modified FFH scaling relation given in the text. The inset shows the original $V-I$ data. The data which collapse onto the universal scaling curves shown in the main figure, in the high current density region, are indicated by solid circles. The field H_ρ corresponds to field at which the maximum of the peak effect in $M(H)$ is observed, as shown in Fig. VI.12. The range of magnetic field over which the $E-J$ data scale are indicated by the outer edges of the shaded region in Fig. VI.12.

correlation length diverges with field as $\xi_g \propto |H - H_g|^{-\nu}$, and E and J scale as $E^* \equiv (E/J)\xi_g^{z+2-d}$ and $J^* \equiv (J/H)\xi_g^{d-1}$. In Appendix C an argument for this form is developed, and shown generally that this field dependent scaling of $E - J$ data provides an equivalent description of vortex glass critical dynamic behavior as that of the established temperature dependent scaling form.

It should be emphasized, however, that the results from using the modified scaling analysis do not correspond to a vortex-glass melting transition, *i. e.*, a vanishing linear resistivity of the form $\rho(T) \sim |T - T_g|^{-\nu}$ or $\rho(H) \sim |H - H_g|^{-\nu}$. Thus, the notation H_ρ is used instead of H_g to indicate the critical field about which the data conform to the modified scaling relation of FFH. Recall the above results for $\rho(T)$ where there is no measurable resistivity below the initial, nearly first order, transition. Also, as seen in Fig. VI.14, the field value H_ρ lies in the middle of the $\rho(H)$ tail and corresponds to the lower field peak, H_{p1} , of the double peak structure seen in ΔF_p in Fig. VI.11, and, the field value of the second peak in ΔF_p corresponds to the usually observed maximum of the anomalous increase of the pinning force density just prior to H_{c2} . Based upon the theoretical arguments developed in Appendices C and D, we suggest that the scaling behavior of the $E - J$ data in CeRu₂ is evidence of a region of a fluctuating suppression of the superfluid density, ρ_s centered at H_ρ , which coincides with the field value of the maximum of the peak effect magnetization curve, that the fluctuation region as defined by the field values over which $E - J$ scales is the peak effect region, and most importantly that this $H_\rho(T)$ line coincides with at least three other important phenomena known for some time to be associated with the peak effect (Fig. VI.15).

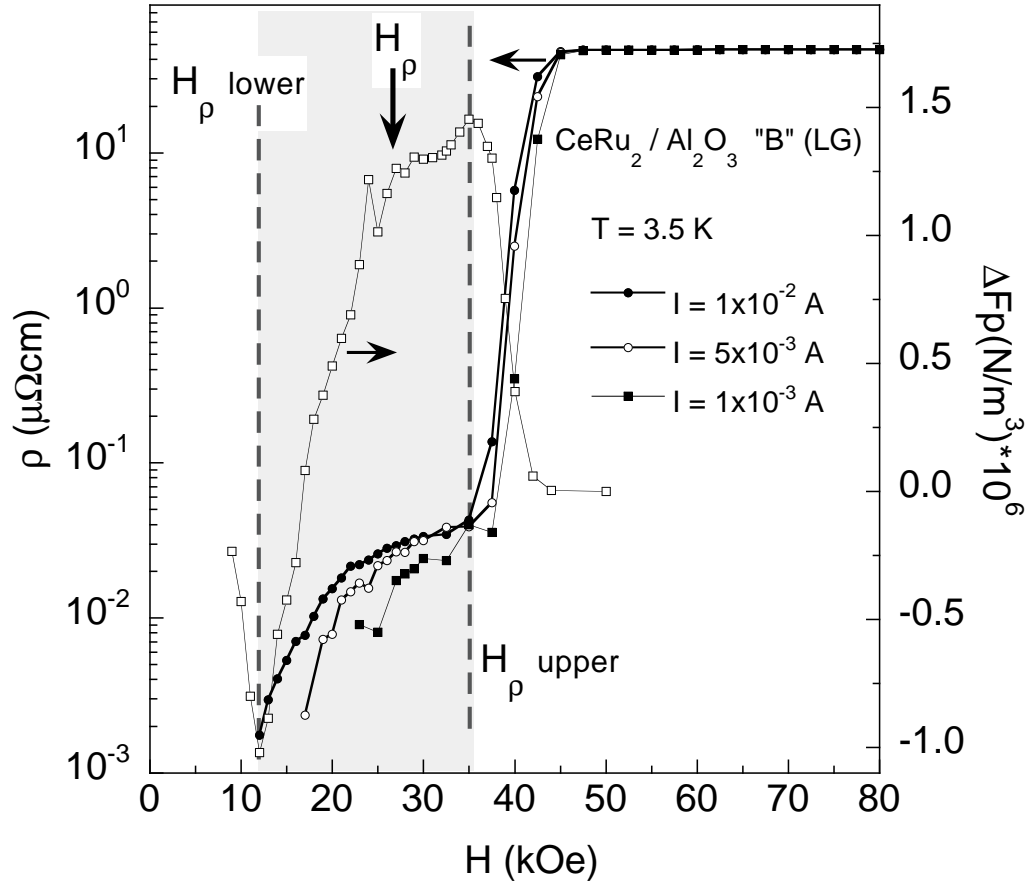


Figure VI.14: Resistivity, $\rho(H)$, data from the large grain film at various current values. The enhanced pinning force region indicated by $\Delta F_p(H)$, of the film is shown, corresponding to the peak effect region. The field region over which the E–J data scale is indicated by the shaded area, with the critical field H_{ρ} seen to lie in the middle of the resistive tail.

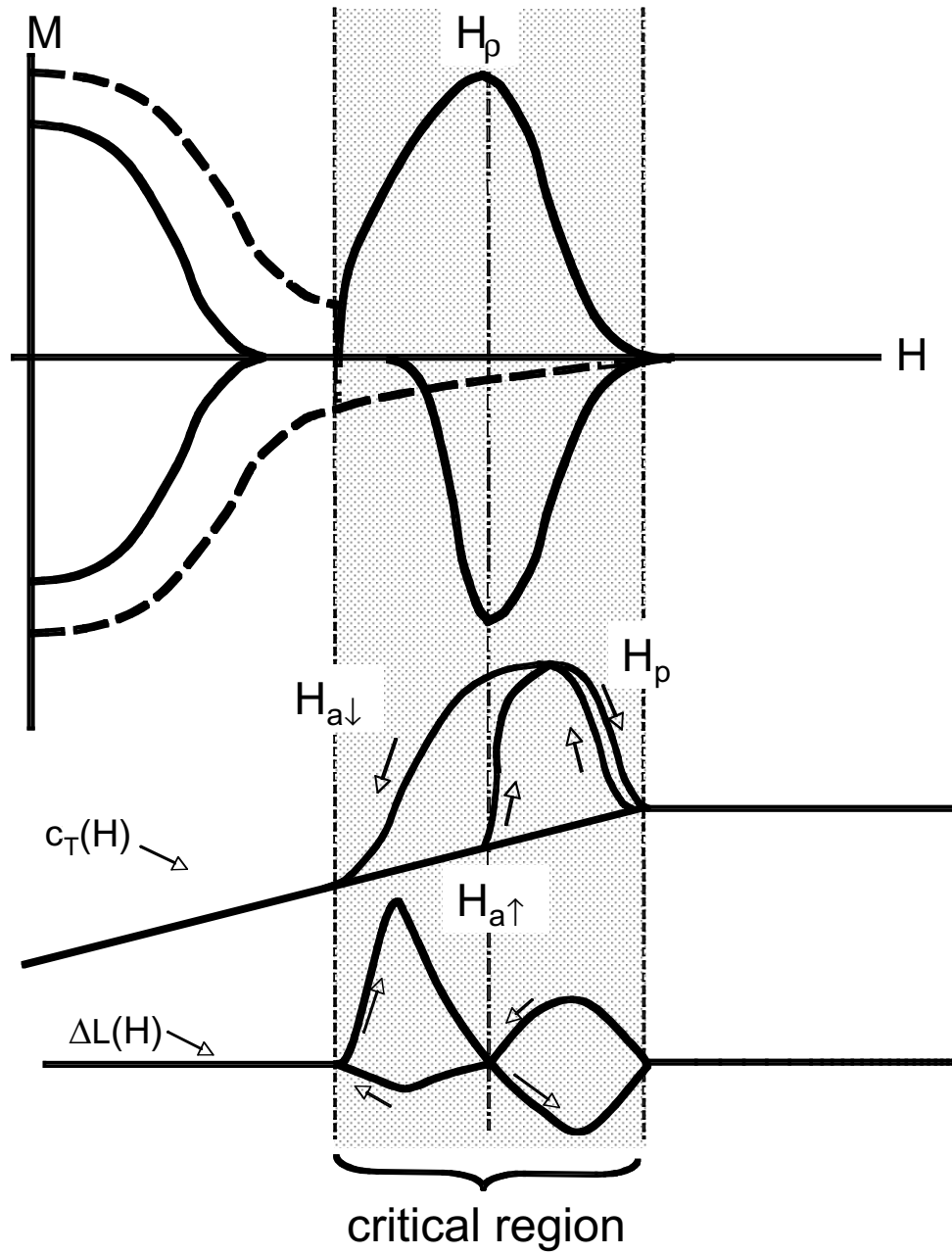


Figure VI.15: Generic behavior of the magnetization, $M(H)$, of a single crystal (solid line, not to scale), and a large grain size film (dashed line). Below is the hysteretic field dependent behavior of the atomic lattice shear moduli, $c_T(H) = \frac{1}{2}(c_{11} - c_{12})(H)$, and the anomalous positive and hysteretic magnetostriction, $\Delta L(H)$.

VI.D Discussion

Before discussing further the results from the data presented above, important results from other studies are reviewed briefly below.

VI.D.1 Review

The softness of CeRu₂ and the band structure model.

Elastic moduli of high quality CeRu₂ single crystals were measured by an ultrasonic method from $T = 300$ K - 2 K by Suzuki *et al.* [7], and Yoshizawa *et al.* [8]. The results of Suzuki *et al.*, revealed a huge lattice softening in both transverse (c_T) elastic moduli, $(c_{11} - c_{12})/2$ and c_{44} , of 55% and 12%, respectively, over this temperature range, without a structural phase transition. An additional anomaly consisting of a kink at $T = T_c$ in both transverse moduli was also found. The bulk modulus, c_B , however, behaves conventionally, increasing with a decrease of temperature and saturating at low temperature. The shear modulus anomalies and the normal behavior of the bulk modulus are suggestive of structural fluctuations coupling to the symmetry breaking strain. Based on band structure calculations [24] which reproduce the experimentally determined Fermi surface [25], Suzuki *et al.*, showed that the unusual elastic behavior can be accounted for by a narrow degenerate band with a high density of states just above E_F which splits in response to the shear strain.

The measurements of $c_T = \frac{1}{2}(c_{11} - c_{12})(H)$ in field by Yoshizawa *et al.*, revealed even more remarkable anomalous behavior that could be directly correlated with the peak effect. As shown in Fig. VI.15, the kink in c_T at $T = T_c$, is suppressed to lower temperatures by a magnetic field, and the field at which this kink occurs corresponds to the upper field of the peak effect region. Additionally, there is an anomalous increase of the value of $c_T(H)$ in the peak effect region *which is hysteretic in a manner that correlates with the hysteresis of the peak effect*, and lies along the same line as the H_p line determined from the scaling of $E - J$ data, as

shown in Fig (VI.16).

Relaxation of peak effect region

Time dependent magnetization measurements of CeRu_2 in the mixed state by Ho *et al.* [10], clearly show a relaxation of the magnetization in the peak effect region. It was observed that the relaxation rate of the magnetization is not uniform over the field loop. Relaxation of the magnetization was seen to occur at a much faster rate in the last quadrant of the loop. This behavior can readily be correlated with the hysteretic features of the magnetization loop and of the transverse elastic moduli c_T . Furthermore, it was found that after a rapid cooling of the sample from room temperature to the superconducting state in zero field, the peak effect was no longer observable. Subsequently, warming the sample back up and cooling at a slow rate resulted in the restoration of the peak effect. The rapid cooling scenario freezes the crystal into a stable, hardened state. This strongly supports the idea that the structural properties of CeRu_2 are a key driving mechanism of the peak effect.

Anomalous magnetostriction behavior

Tachiki *et al.* [4], reported magnetostriction measurements of CeRu_2 in the peak effect region. They found an anomalous expansion of the atomic lattice in this region that is hysteretic in field. As shown in Fig. VI.15 distinct features of the magnetostriction behavior also correlate with the features of the peak effect. These results have also been considered as evidence for the FFLO state.

While one usually thinks of the pinning force as acting on the vortices, as pointed out by Schlessner *et al.*, an equally large distortion force is transferred to the body of the material.[26] Under normal circumstances the structural integrity of the atomic lattice is such that distortions are a negligible effect. However, as discussed above, due to the weak shear modes at low temperatures, CeRu_2 is particularly susceptible to strain forces. There are two stress forces due to the magnetic field

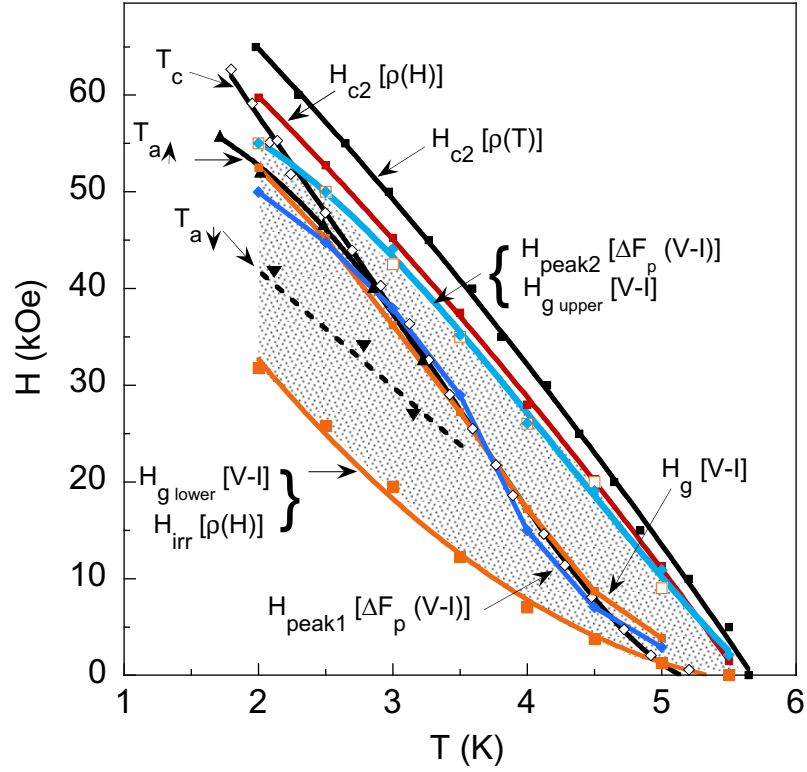


Figure VI.16: $H - T$ phase diagram for the large grain CeRu_2 film (“B”). The H_{c2} lines determined by $\rho(H)$ and $\rho(T)$ measurements are seen to be significantly separated. The discrepancy between the two lines is larger than experimental error and is attributed to the different effects that increasing temperature or magnetic field have on the vortex dynamics. The $H_\rho(T)$ line, inferred from scaling of $E - J$ data coincides with the $T_{a\uparrow}$ line determined from the shear modulus structural anomaly shown in Fig. VI.15. The lines T_c , $T_{a\uparrow}$, and $T_{a\downarrow}$ from Yoshizawa *et al.*, [8] are scaled in temperature and field to adjust for the different $T_c(0)$ and $H_{c2}(0)$ values of their crystal and of the film. The shaded region indicates the region of scaling of the $E - J$ data corresponding to a suppression of the superfluid density with the minimum density along the H_ρ line.

to be taken into consideration. (i) that caused by the flux density gradient profile: inward for ascending and outward for descending fields, as described by the critical state model, resulting in dilation or contraction of the crystal along the applied field direction. (ii) the line tension of a vortex flux tube which attempts to restore the flux tube to a straight, (unkinked,) structure. Within the standard London and Ginzburg-Landau theories, there is no coupling between the vortex lattice and the crystal. A full microscopic theory of the mixed state, using a nonlocal London model [27], contains this coupling via the nonlocal relation between the current density and the vector potential, $J_\alpha(\mathbf{r}) = \int \mathbf{Q}_{\alpha\beta}(\mathbf{r} - \mathbf{r}') \mathbf{A}_\beta(\mathbf{r}') d^3\mathbf{r}'$, where the kernel Q is dependent upon the Fermi surface, pairing symmetry, and field orientation [28, 29]. Then, if the flux line induced stress is dominant, this would lead to a scenario where, upon entering the peak effect region from the lower field region where the vortex ensemble is a vortex liquid (or in a low pinning state in some cases), a pinning mechanism of a different origin than that in the conventional irreversible region results in an enhanced coupling of the vortices to lattice defects. The restoring force of the vortex line tension results in a contraction (dilation) in the direction perpendicular (parallel) to the field.

Anomalous increase of the penetration depth

Magnetic penetration depths, λ , in the mixed state of CeRu₂, measured by muon spin rotation [12, 13], have been seen to undergo an anomalous increase in the peak effect region. An increase was observed from $\lambda \simeq 2000$ Å at $T = 2$ K in the field region below the peak effect region, to $\bar{\lambda} \simeq 3000$ Å within the peak effect region, indicating a significant fractional increase of the normal state electrons, *i.e.*, quasiparticles, outside of the vortex cores. The maximum of the increase of λ corresponds to the maximum of the peak effect loop. With the penetration depth $\lambda \propto \rho_s^{-1/2}$, and the superfluid density given by [13],

$$\rho_s \propto 1 - N_{env}(H)/N_{env}(H_{c2}), \quad (\text{VI.1})$$

where $N_{env}(H)$ is the quasiparticle density of states outside of the vortex cores, the above increase of λ corresponds to a reduction of the superfluid density by approximately 50%. This enhancement of the normal state carrier has been shown to be consistent with the generalized FFLO state, where the nodal vortex state results in an increase of the normal state volume of the sample. Below a different explanation is proposed as to the origin of the increase of the normal state electrons that is consistent with the experimental results concerning the atomic lattice moduli, c_T and the anomalous magnetostriction behavior discussed above.

The martensitic transformation

CeRu₂ belongs to the C15 cubic Laves phase class of compounds, a structural cousin of the A15 compounds. A structural phase transition known as a martensitic transformation, where the lattice undergoes a spontaneous distortion from a cubic to a tetragonal symmetry, is known to occur in superconducting A15 and C15 (Laves phase) compounds [30]. An important characteristic of this class of materials is that a lattice instability will occur at low temperatures if the Fermi energy is close to the bottom of narrow degenerate sub-bands with a high density of states. Near the bottom of these sub-bands the density of states are expected to diverge as $\sim (\epsilon - \epsilon_m^{(0)})^{-1/2}$, where $\epsilon_m^{(0)}$ is the m^{th} sub-band [31]. At temperatures below the transition, T_M , the electrical conductivity increases significantly due to the splitting of the degenerate sub-bands resulting in an excessively high density of states $N(\epsilon_F)$ [31, 32]. Another well known property is that this transition is easily frustrated by disorder [33].

As mentioned above, CeRu₂ at low temperatures, is close to, but does not undergo, a structural phase transition. The issue of the martensitic transition is raised here for three reasons; (i) this transition is known to occur in the C15 class of compounds to which CeRu₂ belongs, (ii) because of the similarity of the electronic band structure arrived at by Suzuki *et al.* [7], and that described above, and (iii) an increase of normal state conduction electrons, such as that caused by

a martensitic transformation, in the superconducting mixed state would suppress the superfluid density, leading to a softening of the vortex lattice shear modes; providing the mechanism of the peak effect.

An argument against CeRu₂ being near a martensitic transformation is that the martensitic transition temperature, T_M , is suppressed to lower temperatures by the application of a magnetic field at a much slower rate than the critical temperature T_c [31, 33], where the shift in temperature is given by

$$\Delta T_M(H) = -0.18 T_M(0) [\mu_B H / \epsilon_F(0, 0)]^2 \quad (\text{VI.2})$$

and $\epsilon_F(0, 0)$ is the Fermi energy at $T = 0$ in the cubic phase. Since, in the case of CeRu₂, at zero field we would have $T_c \gtrsim T_M$, then with the application of a magnetic field T_c would lie below T_M , removing the presumed source of suppression of ρ_s .

While it may be possible that CeRu₂ is very close to a martensitic transition that is being frustrated in an unusual manner, this does not need to be the case. What matters is that the degenerate, high density of states band structure of CeRu₂ described by Suzuki *et al.* [7], will be split in the same manner by the structural fluctuations of the lattice and by the application of a magnetic field.

The missing peak effect in ultraclean CeRu₂ single crystals

Shown in Fig. VI.17 are the pinning force densities of single crystals of CeRu₂ with varying levels of disorder, determined by electrical resistivity measurements, as originally published by Hedo *et al.* [23]. These include a superclean sample with a residual resistance ratio (RRR) of 270, a very clean (RRR = 240), and dirty (RRR = 13) crystal. Remarkably, the pinning force density disappears in the peak effect region in the superclean crystal. A similar result was seen by Tenya *et al.* [34], where they observe that the peak effect from $M(H)$ becomes weaker with increasing RRR. It appears then that disorder is actually a necessary ingredient for the peak effect mechanism, a point that will be returned to below.

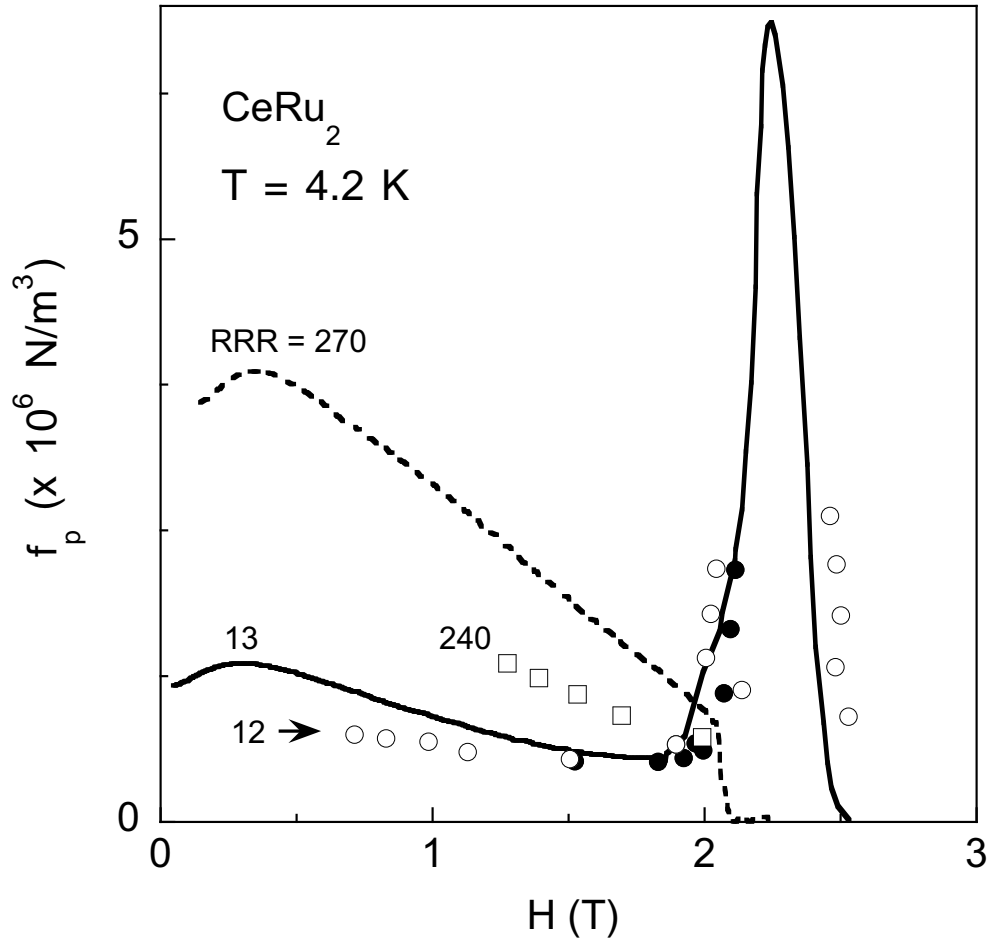


Figure VI.17: Figure from Hedo *et al.*, [23]. Pinning forces in single crystals of CeRu_2 . The pinning force was determined by current dependent resistivity measurements for the samples with $\text{RRR} = 12$ and $\text{RRR} = 240$, shown by open circles and squares, respectively. Solid circles are obtained from I-V data in fields. Data obtained from magnetization measurements for the $\text{RRR} = 270$ and $\text{RRR} = 13$ samples are shown as dotted and solid lines. Note that for fields below the peak effect region, the pinning force density increases with decreasing disorder, but, in the region of the peak effect the pinning force density disappears for the superclean $\text{RRR} = 270$ sample.

VI.D.2 Current results: relation to known peak effect anomalies

The question naturally arises as to why the peak effect is completely absent in the small grain film, and only emergent in the large grain film, if they are of such high quality with respect to lattice defects within the grains. An argument is developed below for what this result, along with the evidence for suppression of the superfluid density from the scaling analysis of the E–J data, contributes to the picture of the peak effect mechanism in CeRu₂.

The evidence from the studies reviewed above strongly point to a coupled structural-electronic origin of the peak effect. The simple explanation for the results of this study is that the grains of the films are under differing average levels of strain. The small grains of film “A” have a higher level of surface tension, and smaller available internal volume able to undergo the intrinsic atomic lattice deformation process. The large grains of film “C”, grown on the LaAlO₃ substrate, are well attached to the substrate and experiences a larger interface strain than film “B”, grown on an Al₂O₃ substrate. Film “B”, under the least external and surface strain, exhibits a nascent peak effect because it is able to deform just enough to begin the structure driven splitting of the degenerate electronic sub-band and shifting of energy levels.

While this explanation of the “missing” peak effect in our films is consistent, there remains the matter of the “missing” peak effect observed in ultraclean CeRu₂ single crystals [9, 23], mentioned above. Since the crystals in the above studies are relatively large and of the same size, then the size/strain effect postulated for the grains can not be relevant here. Thus, disorder to a certain extent plays a role in enhancing or aiding the peak effect process. We consider two possible reasons for this. (i) As happens with the martensitic transformation discussed above, the structural deformation process is likely readily frustrated by defects. The deformation of the atomic lattice is tied to the electronic properties, *i.e.*, the band splitting effects. If the deformation is unimpeded and the splitting of the bands continues beyond a critical level, then $N(\epsilon_F)$ will be excessively large and

the superfluid density will never recover enough stiffness to allow the vortex lattice to acquire a sufficiently strong shear modulus, thus the enhancement of the ability of the vortices to acquire a higher pinning configuration will be lost to the over weakening of the rigidity of the vortex lattice. (ii) The coupling of the vortices to the lattice plays an important role in driving or sustaining the peak effect mechanism. (a) The absence of defects removes the defect-vortex line coupling strain from the deformation dynamics. A nearly perfect vortex lattice, with its motion unimpeded will be easily displaced by the Lorentz force of an applied current, resulting in transport behavior of the TAFF kind, as observed in the small grain film whose grain dimensions are of the same length scale as the mean free path. (b) The collective critical nature of the vortices indicated by the scaling of the E – J data may provide an enhancement of the vortex line tension via the correlated dynamical manner in which vortex motion takes place, beyond that of the single line picture.

While the point in (i) above sufficiently explains the single crystal picture, and it is not invalidated by the results from the films, it can not be the case here if, as presumed, the strained state of the films prevents the initiation of the peak effect mechanism. Thus, the latter idea is further explored here, particularly the collective nature of the vortices in the peak effect region.

If, as suggested by the scaling properties of the $E - J$ data in the large grain sample, the vortex ensemble is in a critical dynamical state akin to a vortex glass critical region, then a correlation length scale, ξ^{vg} , associated with the dynamical behavior plays a relevant physical role. Using the scaled $E - J$ data from the large grain sample, the coherence length of the vortex glass at the boundary of the peak effect region is calculated [19, 35]. The values are given in Table VI.1. It is seen that the coherence length, ξ^{vg} is effectively cutoff by the grain size dimensions in the small grain film prior to, or just inside the peak effect region, and will be cutoff at some point in the peak effect region prior to the critical field line H_ρ . While these results are certainly not conclusive, they suggest that the granular

regions must reach a critical size to support the critical dynamic vortex behavior, which in turn, plays a supporting role in the structural deformation process of the atomic lattice. The enhancement of vortex line-atomic lattice coupling in the peak effect region may not require the somewhat exotic scenario suggested above, but it is apparent that a sufficient amount of disorder must be present for the vortices to be able to couple to, and exert strain upon, the atomic lattice. What should be understood from the scaling of the $E - J$ data, is that the dynamic properties of the vortices are changing in response to a change in their environment, and as such, the $H_p(T)$ line does not necessarily constitute a vortex phase transition boundary.

Finally, we are left then with the following scenario summary: The peak effect occurs because of enhanced pinning of the vortices. The enhanced pinning is a result of the vortices being able to rearrange into a stronger (more tangled) pinning configuration. This is made possible by a weakening of the shear moduli of the vortex lattice. The weakening of the vortex lattice shear moduli is a result of a reduction of the superfluid density, $c_{66} \propto \rho_s$, etc. The suppression of the superfluid density comes from an increase of the normal state electrons, quasiparticles, outside of the vortex core. The increase of quasiparticles has two possible (and not mutually exclusive) sources. (i) The GFFLO state described above. (ii) A frustrated martensitic like scenario which is consistent with both the observed lattice softening in CeRu₂ and the doubly degenerate band model of Suzuki *et al.* [7].

The latter scenario is the interpretation we favor. Many previous arguments against the GFFLO state persist. Additionally, the difference in the upper critical field lines, $H_{c2}(T)$, determined by resistivity data as a function of field or temperature, $H_{c2}(T)[\rho(H)]$ or $H_{c2}(T)[\rho(T)]$, reveals an asymmetry of the vortex dynamical state with respect to approaching the upper critical field in temperature or magnetic field. This asymmetry is not accounted for by the (G)FFLO model, but can be attributed to a field–temperature asymmetry of the strain moduli. The

anomalous increase of the normal state electron density in the peak effect region can be explained naturally by a band structure that is known to exist. The lattice deformation-electronic band splitting phenomenon may be frustrated or aided by magnetostriction effects. If this is the case, this could possibly be investigated by measurements of the superfluid density in single crystals with a variation of the angular dependence of the applied field, or by measurements under uniaxial and/or hydrostatic pressure.

VI.E Summary

The first study of the peak effect in CeRu_2 films grown by the pulsed laser ablation method is reported here. The films exhibit residual resistivities and low field pinning force densities comparable to single crystals, yet the peak effect is not readily observable in electrical resistivity, $\rho(H, T)$, or magnetization, $M(H)$, measurements. The pinning force density, determined by transport measurements, in the peak effect region *is nearly zero* in the small grain film, and is seen to be emerging with a much lower than usual strength in the large grain size film. Magnetization, $M(H)$, measurements indicate a zero pinning force density in both samples in the peak effect region. In the region of the emerging peak effect, the large grain film exhibits electrical transport behavior reminiscent of the dynamical behavior of a vortex glass. In this same region, transport measurements of the small grain size film are found to be consistent with a thermally assisted flux flow (TAFF) scenario. The vortex-glass like behavior associated with the peak effect in the large grain film is considered to be evidence of fluctuations of the superfluid density, ρ_s . Evidence is seen for an important role of the softening of the atomic lattice moduli, from previous ultrasound, magnetostriction, and magnetic relaxation studies [4, 7, 8, 10], and for the coupling of the vortex lattice to the atomic lattice. The critical behavior of vortices in the large grain film, inferred from scaled $E-J$ data, can be correlated with both the anomalous field dependence

of the shear moduli and the magnetostriction. This study strongly suggests the origin of the peak effect in CeRu_2 has a conventional explanation, originating with the unusual structural properties and the degenerate band structure near the Fermi level.

Table VI.1: Values of the critical temperature, T_g , and field, H_g for the large grain film. Also listed are values for the zero temperature vortex glass correlation length ξ_0^{vg} , the values of ξ^{vg} and the lattice constant a_Δ at the lower field of the peak effect region, ξ_-^{vg} and a_Δ^- , respectively, and the ratio of the temperature at which the correlation length will exceed the grain size to the temperature at the critical line, $H_g(T)$, for the small and large grain films.

T(K)	H_g (T)	ξ_0^{vg} (Å)	$\Delta\xi_0^{vg}$ (Å)	ξ_-^{vg} (Å)	a_Δ^- (Å)	t_{sg}	t_{lg}
2.0	5.25	180	65	1160	271	0.75	0.94
2.5	4.52	320	105	2300	309	0.61	0.91
3.0	3.62	1100	240	9240	346	0.05	0.78
3.5	2.72	1580	370	27800	489	—	0.56
4.0	1.72	1670	460	41900	631	—	0.43
4.5	0.87	1900	690	87610	892	—	0.08

A portion of the text and data of this chapter appears as it will be published in the article, “Anomalous critical dynamic behavior of vortices amidst a nascent peak effect in granular CeRu_2 films,” B. J. Taylor, R. E. Baumbach, T. A. Sayles, and M. B. Maple. The dissertation author was the primary investigator and author of this article.

Bibliography

- [1] B. T. Matthias, H. Suhl, and E. Corenzwit, Phys. Rev. Lett. **1**, 449 (1958).
- [2] P. Fulde and R. A. Ferrell, Phys. Rev. **135**, A550 (1964).
- [3] A. I. Larkin and Yu. N. Ovchinnikov, Sov. Phys.-JTEP **20** 762 (1965).
- [4] M. Tachiki, S. Takahashi, P. Gegenwart, M. Weiden, M. Lang, C. Geibel, F. Steglich, R. Modler, C. Paulsen, and Y. Ônuki, Z. Phys. B **100**, 369 (1996).
- [5] N. R. Dilley and M. B. Maple, Physica C, **278**, 207 (1997).
- [6] K. Kadowaki, H. Takeya, and K. Hirata, Phys. Rev. B, **54**, 462 (1996).
- [7] T. Suzuki, H. Goshima, S. Sakita, T. Fujita, M. Hedo, Y. Inada, E. Yamamoto, Y. Haga, and Y. Ônuki, J. Phys. Soc. Jpn. **65**, 2753 (1996).
- [8] M. Yoshizawa, M. Tamura, M. Ozawa, D.-H. Yoon, H. Sugawara, H. Sato, and Y. Ônuki, J. Phys. Soc. Jpn. **66**, 2355 (1997).
- [9] K. Tenya, S. Yasunami, T. Tayama, H. Amitsuka, T. Sakakibara, M. Hedo, Y. Inada, E. Yamamoto, Y. Haga, and Y. Ônuki, J. Phys. Soc. Jpn, **68**, 224 (1999).
- [10] P.-C. Ho, S. Moehlecke, and M. B. Maple, cond-mat/0301281 (2005).
- [11] D. Groten, S. Ramakrishnan, B. Becker, G. J. Nieuwenhuys, J. A. Mydosh, and J. Aarts, Physica B **230**, 377 (1997).
- [12] A. Yamashita, K. Ishii, T. Yokoo, J. Akimitsu, M. Hedo, Y. Inada, Y. Ônuki, E. Yamamoto, Y. Haga, and R. Kadono, Phys. Rev. Lett. **79**, 3771 (1997).
- [13] R. Kadono, W. Higemoto, A. Koda, K. Ohishi, T. Yokoo, J. Akimitsu, M. Hedo, Y. Inada, Y. Ônuki, E. Yamamoto, and Y. Haga, Phys. Rev. B **63**, 224520 (2001).
- [14] D. C. Cronmeyer, J. Appl. Phys. **70**, 2911 (1991).
- [15] Y. Inada and Y. Ônuki, Low Temp. Phys. **25**, 573 (1999).
- [16] T. P. Orlando and M. R. Beasley, Phys. Rev. Lett. **46**, 1598 (1981).
- [17] M. P. A. Fisher, Phys. Rev. Lett. **62**, 1415 (1989).
- [18] M. P. A. Fisher, Phys. Rev. Lett. **65**, 923 (1990).
- [19] D. S. Fisher, M. P. A. Fisher, and D. A. Huse, Phys. Rev. B **43**, 130 (1991).
- [20] T. Giamarchi and P. Le Doussal, Phys. Rev. B **52**, 1242 (1995); **55**, 6577 (1997).

- [21] N. R. Dilley, J. Herrmann, S. H. Han, M. B. Maple, S. Spagna, J. Diederichs, and R. E. Sager, *Physica C* **265**, 150 (1996).
- [22] D. Groten, E. Ardonne, S. Ramakrishnan, G. J. Nieuwenhuys, and J. A. Mydosh, *Physica C* **306**, 271 (1998).
- [23] M. Hedo, Y. Kobayashi, Y. Inada, E. Yamamoto, Y. Haga, J. Suzuki, N. Metoki, Y. Ônuki, H. Sugawara, H. Sato, K. Tenya, T. Tayama, H. Amitsuka, and T. Sakakibara, *Physica B*, **259**, 688 (1999).
- [24] M. Higuchi and A. Hasegawa, *J. Phys. Soc. Jpn.* **65**, 1302 (1996).
- [25] M. Hedo, Y. Inada, T. Ishida, E. Yamamoto, Y. Haga, Y. Ônuki, M. Higuchi, and A. Hasegawa, *J. Phys. Soc. Jpn.* **64**, 4535 (1995).
- [26] R. Schleser, P. J. E. M. van der Linden, P. Wyder, and A. Gerber, *Phys. Rev. B* **67**, 134516 (2003).
- [27] V. G. Kogan, A. Gurevich, J. H. Cho, D. C. Johnston, Ming Xu, J. R. Thompson, and A. Martynovich, *Phys. Rev. B* **54**, 12386 (1996); V. G. Kogan, M. Bullock, B. Harmon, P. Miranovic, Lj. Dobrosavljevic-Grujic, P. L. Gammel, and D. J. Bishop, *Phys. Rev. B* **55**, R8693 (1997).
- [28] A. Gurevich and V. G. Kogan, *Phys. Rev. Lett.* **87**, 177009 (2001).
- [29] P. Miranović and V. G. Kogan, *Phys. Rev. Lett.* **87**, 137002 (2001).
- [30] V. G. Pushin and V. V. Kondrat'ev, *Fiz. Met. Metalloved.* **78**, 40 (1994).
- [31] J. P. Maita and E. Bucher, *Phys. Rev. Lett.* **29**, 931 (1972).
- [32] K. Ikeda, K. A. Gschneidner, Jr., B. J. Beaudry, and T. Ito, *Phys. Rev. B* **25** 4618 (1982); K. Ikeda, K. A. Gschneidner, Jr., B. J. Beaudry, and U. Atzmony, *Phys. Rev. B* **25** 4604 (1982).
- [33] J. Šebek, M. Mihalik, O. Syshchenko, J. Vejpravová, *Czech. J. Phys.* **52**, 291 (2002).
- [34] K. Tenya, S. Yasunami, T. Tayama, H. Amitsuka, T. Sakakibara, M. Hedo, Y. Inada, Y. Haga, E. Yamamoto, and Y. Ônuki, *Physica B* **259**, 692 (1999).
- [35] Shi Li, B. J. Taylor, N. A. Frederick, M. B. Maple, V. F. Nesterenko, and S. S. Indrakanti, *Physica C* **382**, 177 (2002).
- [36] E. H. Brandt, *Rep. Prog. Phys.* **58**, 1465 (1995).
- [37] M. J. P. Gingras and D. A. Huse, *Phys. Rev. B* **53**, 15193 (1996).
- [38] M. E. Fisher, M. N. Barber, and D. Jasnow, *Phys. Rev. A* **8**, 1111 (1973).

Appendix A

The modified vortex glass scaling model of Rydh, Rapp, and Andersson

Recently Rydh, Rapp, and Andersson (RRA)[1, 2] developed a modified Vortex-glass (MVG) model based on the original model of Fisher, Fisher, and Huse (FFH) [3], and the empirically observed equation for the vortex glass melting line by Lundqvist *et al.* [4], where,

$$B_m \approx \frac{1.85\Phi_0}{(\gamma d)^2} [(1-t)/t]^\alpha, \quad (\text{A.1})$$

with d the interlayer spacing, and $\alpha \approx 1$. RRA arrive at a scaling law for the vanishing of the resistivity as the critical temperature T_g is approached, such that resistivity data taken in various constant magnetic fields will collapse onto a single curve when it is plotted as

$$\left[\frac{\rho(T)}{\rho_N} \right] \text{ vs. } \frac{T(T_c - T_g)}{T_g(T_c - T)} - 1. \quad (\text{A.2})$$

Additionally, Lundqvist *et al.*, used the expression of the vortex lattice melting line arrived at by Blatter and Ivlev to lend support for the melting line equation. It is easily seen that Eq. (A.1) can be recovered as a high Q or q limiting case of Eqs. (III.15) and (III.16) where $\alpha = \tilde{s}$.

Appendix B

The Columb-gas model

The scaling laws from the Coulomb-gas (CG) scaling model [5] are nearly equivalent to those found from the modified vortex-glass thermal depinning model of Rydh, Rapp, and Andersson [1, 2]. This can be seen simply by examining the scaling functions of the resistivity in the two cases. In the CG model the resistivity data, $\rho(T)$, is predicted to scale such that for all applied magnetic fields in the relevant regime, the data will collapse onto a single curve when plotted as,

$$\ln \left[\frac{\rho(T)}{\rho_N} \right] \text{ vs. } \frac{T (T_c - T_g)}{T_g (T_c - T)}. \quad (\text{B.1})$$

RRA note that their scaling law is very similar to the CG scaling relation, and surmise that there is a likely connection between the generalized Coulomb-gas model and their modified Vortex-glass model. The situation is thus: If resistivity data will scale according to the CG model it will also scale according to the MVG model, and vice versa. This equivalence is shown in Fig. (B.1) where generic resistivity data for two different magnetic fields that follows the MVG relation,

$$\rho(T, B) = \rho_N \left| \frac{T (T_c - T_g)}{T_g (T_c - T)} - 1 \right|^s \quad (\text{B.2})$$

is plotted according to both scaling relations.

However, it is possible to distinguish between the two cases. If, as is shown in Fig. (B.2), we plot generic resistivity data which follow the CG relation for resistivity instead,

$$\ln \left[\frac{\rho(T, B)}{\rho_N} \right] = -A / \left(\frac{T(T_c - T_g)}{T_g(T_c - T)} - 1 \right)^{0.5}, \quad (\text{B.3})$$

the data can again be seen to collapse in either case, *however* the data fail to exhibit the predicted power law behavior in the MVG scaling plot. Thus, it is quite obvious, from a formalistic and phenomenological examination, that the CG model is a special case or subset of the MVG model, which is itself a special case (the large q limit) of Eq. (III.16).

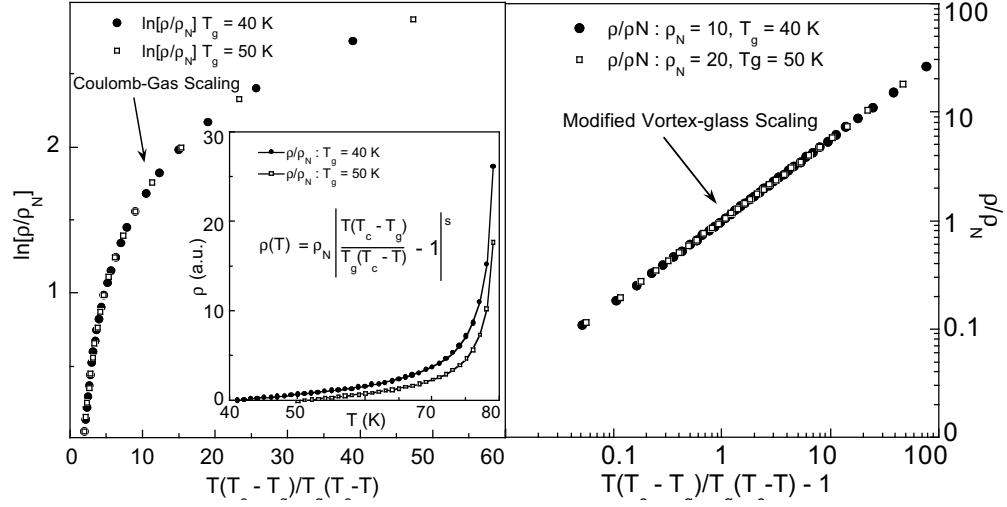


Figure B.1: Generic resistivity data that follow the modified Vortex-glass relation $\rho(T, B) = \rho_N \left| \frac{T(T_c - T_g)}{T_g(T_c - T)} - 1 \right|^s$, plotted according to the CG (left panel) and MVG (right panel) scaling laws. Notice the linear (on a log-log plot) behavior of the data in the MVG plot, a key indicator of vortex-glass behavior.

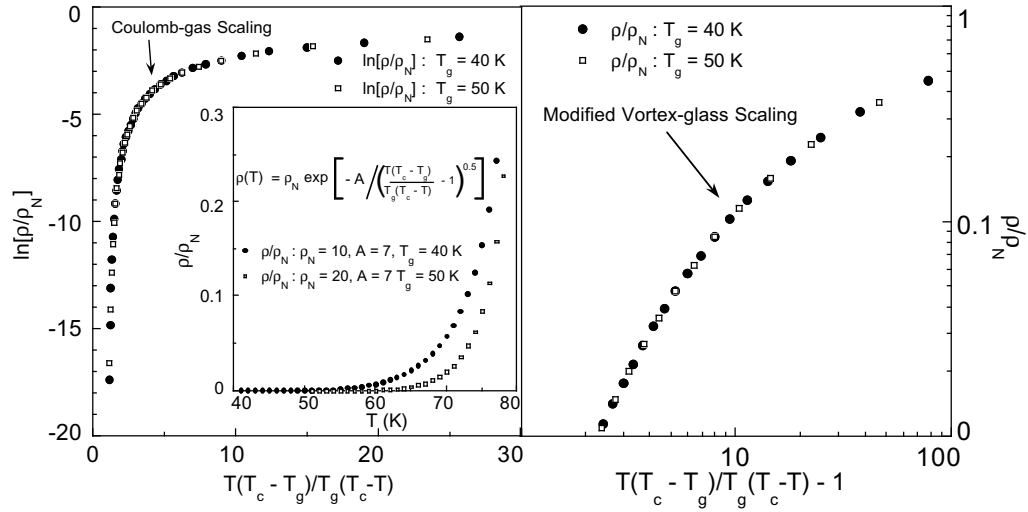


Figure B.2: Generic resistivity data that follow the Coulomb-gas relation $\ln \left[\frac{\rho(T, B)}{\rho_N} \right] = -A / \left(\frac{T(T_c - T_g)}{T_g(T_c - T)} - 1 \right)^{0.5}$, plotted according to the CG (left panel) and MVG (right panel) scaling laws. Notice the lack of linear (on a log-log plot) behavior of the data in the MVG plot, indicating that vortex-glass behavior is not the case here.

Appendix C

Modified vortex glass scaling model: Magnetic field dependencies

The current–voltage characteristics of a vortex ensemble that undergoes a vortex-glass melting transition in a fixed magnetic field, H , is such that, as the temperature approaches the transition temperature T_g , E–J data will scale according to the form arrived at from the ansatz of (FFH) [3, 6]. The dissipative electric field with a dc current density J will scale as

$$E \approx J \xi_g^{d-2-z} \mathcal{E}_{\pm}(J \phi_0 \xi_g^{d-1}/cT) \quad (\text{C.1})$$

from which the scaled electric field and current densities are then given by

$$E^* \equiv (E/J) \xi_g^{z+2-d},$$

and

$$J^* \equiv (J/T) \xi_g^{d-1}.$$

ξ_g is the vortex glass coherence length which, in the critical region, vanishes linearly with temperature such that $\xi_g \propto |T - T_g|^{-\nu}$. The exponents ν and z are referred to as the static and dynamical critical exponents, and d is the dimensionality of the vortex system.

Starting from the form of the coherence length given by Brandt [7], $\xi_g(H, T) = \xi_g(H) |1 - T/T_g|^{-\nu}$, we naturally expect a divergence of the correlation length scale $\xi_g(H, T)$ regardless of whether the melting line is approached

in field or in temperature. The assumption that $\xi_g(H)$ should take the form $\xi_g(H) \propto |1 - H/H_g|^{-\nu}$ is supported by both experimental observation and related theoretical models. Electrical transport data exhibit a linear dependence with respect to field, H , over a range beginning at a critical field H_g when plotted as $[d[\ln \rho]/dH]^{-1}$ vs H . This field dependence is analogous to the linear temperature dependence of $\rho(T)$ data plotted as $[d[\ln \rho]/dT]^{-1}$ vs T over a temperature range beginning at the critical temperature T_g and extending up to a temperature T_g^u corresponding to the upper limit of the critical region. Theoretical support for this form can be found both in the work of Gingras and Huse [8], and Fisher [9]. In the former, it is observed, within the context of the random field X-Y model with topological defects, that the correlation length ξ diverges as $\xi \sim (H - H_c)^{-\nu}$ as a transition from a topologically ordered phase to a disordered phase is approached. Fisher considered the scenario when the field-tuned superconductor-insulator transition from the vortex- to electron-glass phase is approached as the magnetic field increases in the $T \rightarrow 0$ limit. The assumption was also made that as one nears the critical field of the transition, B_c , a diverging correlation length is expected such that $\xi_B \sim (B - B_c)^{-\nu}$.

Next, we return to the derivation for the original expression for the scaling form of the current density arrived at by F-F-H [3], $J^* \equiv (J/T)\xi_g^{d-1}$. This expression is found by the argument that the characteristic current density within the scaling regime will be that which is large enough to change the statistics of the phase of the order parameter and that of the vortex-line fluctuations. In an isotropic system, the variation in the phase will be $\sim 2\pi$ within a correlation volume so then $|\nabla\phi| \sim 1/\xi$. With the coupling of an external current to a phase gradient via

$$\delta F_J = - \int \frac{\phi_0}{c} \mathbf{J} \cdot \nabla \phi, \quad (\text{C.2})$$

then, within a correlation volume ξ^D , δF_J will be of the order of $k_B T$, and thus of similar magnitude to the spontaneous fluctuations when $J \sim (cT)/\phi_0 \xi^{d-1}$ (where

c is a constant). However, from the perspective of approaching the critical region by an increase in field at a fixed temperature, the increase of the free energy of the superfluid density is proportional to the number of flux lines within the superfluid, which is proportional to the applied magnetic field H . Then, within the same correlation volume ξ^D , we will have $\delta F_J \sim H$ and comparable in magnitude to the spontaneous fluctuations when $J \sim (cH)/\phi_0 \xi^{d-1}$ (where c is a different constant than above). Hence, it follows, that as the critical region is approached in the $H-T$ phase diagram along the field axis we expect similar scaling properties as those established by F-F-H, with now E and J scaling as $E^* \equiv (E/J)|H - H_g|^{-\nu(z+2-d)}$ and $J^* \equiv (J/H)|H - H_g|^{-\nu(d-1)}$.

Appendix D

Critical behavior: suppression of the superfluid density

Here we show that the scaling forms of $E^* - J^*$ as given by FFH [3] or those derived in Appendix C, give information about the the superfluid density ρ_s in the critical region.

For simplicity, we work with the scaling forms given by FFH [3]. From the form of the complex conductivity at low frequency and $T < T_c$,

$$\sigma(\omega) \approx \rho_s / (-i\omega + \epsilon) \quad (\text{D.1})$$

and, using the scaling properties in the critical region where the relaxation time scales as $\tau \sim \xi^z$ [3], the superfluid density scales as $\rho_s \sim \xi^{2-d}$ [3, 10], with $\xi \sim |T - T_c|$, the scaling relation of the frequency dependent conductivity is then

$$\sigma(\omega) \approx \xi^{z+2-d} \mathcal{S}_{\pm}(\omega \xi^z). \quad (\text{D.2})$$

When $T \rightarrow T_c^+$, the dc conductivity, $\sigma(0)$, diverges as $\tau \rho_s \sim \xi^{z+2-d}$.

The FFH ansatz generalizes the zero field scaling properties of the superconducting transition to the vortex glass melting transition, where the melting line is considered to be a line of critical points so that $T_c \Rightarrow T_g$, and $\xi^{VG} \sim |T - T_g|$.

Then, from the E–J scaling forms where

$$E^* \equiv \frac{E}{J} |T - T_g|^{-\nu(z+2-d)} \quad (\text{D.3})$$

and

$$J^* \equiv \frac{J}{T} |T - T_g|^{-2\nu} \quad (\text{D.4})$$

with $J = \sigma E$ and $\sigma/\tau \sim \rho_s$,

$$\frac{1}{E^* |T - T_g|^{\nu(2-d)}} = \frac{\sigma}{|T - T_g|^{-\nu z}} \sim \rho_s. \quad (\text{D.5})$$

So then the divergent $E^* \rightarrow \infty$ behavior at $T = T_g$ corresponds to $\sigma \sim \rho_s \rightarrow 0$, *i.e.* a suppression of the superfluid density at a critical temperature/field.

Bibliography

- [1] A. Rydh, Ö. Rapp, and M. Andersson, Phys. Rev. Lett. **83**, 1850 (1999).
- [2] M. Andersson, A. Rydh, and Ö. Rapp, Phys. Rev. B **63**, 184511 (2001).
- [3] D. S. Fisher, M. P. A. Fisher, and D. A. Huse, Phys. Rev. B **43**, 130 (1991).
- [4] B. Lundqvist, A. Rydh, Yu. Eltsev, Ö. Rapp, and M. Andersson , Phys. Rev. B **57**, R14064 (1998).
- [5] P. Minnhagen, Rev. Mod. Phys. **59**, 1001 (1987).
- [6] M. P. A. Fisher, Phys. Rev. Lett. **62**, 1415 (1989).
- [7] E. H. Brandt, Rep. Prog. Phys. **58**, 1465 (1995).
- [8] M. J. P. Gingras and D. A. Huse, Phys. Rev. B **53**, 15193 (1996).
- [9] M. P. A. Fisher, Phys. Rev. Lett. **65**, 923 (1990).
- [10] M. E. Fisher, M. N. Barber, and D. Jasnow, Phys. Rev. A **8**, 1111 (1973).